Investigation on shielding effectiveness of reverberant enclosures with contents

Jiexiong Yan

Doctor of Philosophy

University of York
Electronic Engineering
March 2019

Abstract

Shielding is a method to protect electronic devices from electromagnetic interference and the protection is usually provided by using an enclosure. This ability of protection is quantified by shielding effectiveness (SE). Most of methods to predict SE are about empty enclosures. It has been shown that the presence of contents affects the SE and hence they should be considered.

The power balance (PWB) method is widely used for analysing shielding problems of populated enclosures. By using this method, the contents are represented by their absorption cross sections (ACS). Previous ACS measurements were performed when the contents were unpowered. This might be a problem if the contents contain active devices. In order to investigate the influence of power states on ACS, we measured the ACS of some computer components when they were powered on and off. Comparison suggests that their ACS barely change in different power states. Therefore, it can be concluded that power state has little effect on ACS measurements.

The PWB method assumes that in the steady state, the internal field of an enclosure is uniform, which is not true when the internal loss is high. In order to overcome this limitation, a 2D diffusion model has been proposed. It stems from acoustics and is a generalization of the PWB method. In this work, the 2D model has been expanded to a 3D one. The 3D diffusion model was verified by using it to predict the power density in a populated enclosure and compare the predictions with those obtained by full wave simulation and measurement. The result indicates that when the loss in an enclosure is high, the internal field is not uniform and the 3D diffusion model is able to describe the variation of field.

Contents

List of Tables

List of Figures

Acknowledgements

I still remember my first day at the University of York. I hauled my luggage in the campus, feeling excited, wondering what my life would be. Days go by, now four years have passed and my PhD study is approaching to an end. When I look back on my journey, all I can think of is a cliché: time flies fast!

During my time at the EMC research group, I received help from many people. Without them, I could not have accomplished my work. I would like to express my appreciation to the following people. First, my supervisors John Dawson and Andy Marvin. They are both experienced, professional and easy-going. I learned not only knowledge from them, but also critical thinking and an excelsior's attitude. I will always remember their guidance. Then, Martin Robinson, a friendly member of the EMC group, who has an amazing insight. He always notices details that slipped through other people's eyes. Last but not least, Ian Flintoft, a researcher who knows all. Although he is not my supervisor, when I have problems with my measurements, he is always the first one I turn to for help.

At last, I would like to dedicate this thesis to my parents, who support me unconditionally. Because of them, I can concentrate on my study. Their love, I can never repay.

Declaration

I declare that this thesis is a presentation of original work and I am the sole author. This work has not been previously presented for an award at this or any other university. All sources are acknowledged as references.

This thesis contains research presented in the following publications.

- J. Yan, J. Dawson and A. Marvin, “Effect of power states on absorption cross sections of personal computers: applications to enclosure shielding,” Proceedings of the 2017 International Symposium on Electromagnetic Compatibility (EMC Europe 2017), Angers, France, pp. 1-5, September 2017.
- J. Yan, J. Dawson and A. Marvin, “Estimating reverberant electromagnetic fields in populated enclosures by using the diffusion model ,” Proceedings of the 2018 IEEE Symposium on Electromagnetic Compatibility, Signal Integrity and Power Integrity (EMC+SIPI 2018), Long Beach, USA, pp. 363-367, July 2018.
- J. Yan, J. F. Dawson, A. C. Marvin, I. D. Flintoft and M. P. Robinson, “3D diffusion models for predicting electromagnetic power density in loaded enclosures,” IEEE Transactions on Electromagnetic Compatibility (Early Access), 2019.

Chapter 1

Introduction

1.1. Backgrounds

Any electrical or electronic system generates electromagnetic waves when operating. Sometimes the waves are intentional such as in radio and radar transmitters, but often they are unintentional and can interfere with other components. Those unintentional waves may be a source of electromagnetic interference (EMI). EMI causes degradation of the system's performance and therefore needs to be mitigated. Electromagnetic compatibility (EMC) is the ability of systems to co-exist without causing electromagnetic interference to each other. It provides a fertile area of research in which the improvement of the co-existence of different components in a system is studied. By co-existence, we mean the components do not cause interference with other components and they are not susceptible to emissions from other components. This co-existence is achieved by reducing the EMI coming from either outside or other components. EMI can be reduced by: 1. Suppress the EMI at its source; 2. Make the propagation paths of EMI as inefficient as possible; 3. Make the potential receiver less susceptible to EMI. The transfer of electromagnetic energy can be further divided into two groups: radiated emissions and radiated susceptibility. A number of methods have been applied to deal with these four basic EMC sub problems, such as shielding, grounding, bonding and filtering [1].

This thesis focuses on shielding technique. The main purposes of shielding technique are: 1. To reduce emitted EMI; 2. Prevent external EMI to enter a shielded space. To achieve these purposes, a shell is constructed as an enclosure surrounding some or all of a system. The ability of an enclosure to protect its contents from EMI is quantified by its shielding effectiveness (SE), which is influenced by several factors, such as the material of the enclosure, aperture penetrations, the frequency of EMI and the distance between the EMI source and the enclosure.

Two issues are important to shielding problems. One is the effect of apertures. A perfectly shielded enclosure should block EMI completely. However, in reality, an equipment enclosure

always has holes and/or slots for purposes like ventilation and inspection. Their presence allow EMI to penetrate into the enclosure and reduce the shielding effectiveness. In order to accurately predict the shielding effectiveness of enclosures, apertures should be considered. At low frequencies where there are only a limited number of modes excited in an enclosure, circuit approximation can be applied to obtain shielding effectiveness. The work presented in this thesis is mostly about the reverberant regime where many modes are excited. Therefore, circuit models are not suitable for our study.

The other issue with the shielding problems of enclosures is that in reality, they always have contents. It has been proved that the presence of contents change the internal fields and thus affect the shielding effectiveness [2]. In present day, the high packing density of contents in an enclosure makes it impossible to ignore their effects on electromagnetic fields. One method to analyse the shielding problems of populated enclosures is the power balance (PWB) method [3], which is applicable to cases where the loss in an enclosure is low. By using the PWB method, the shielding effectiveness of an enclosure can be calculated from the absorption cross section (ACS) of the content and the transmission cross section (TCS) of the aperture [4]. The advantage of the PWB method is that it does not require the detailed geometry of the content. Therefore, it is able to provide fast approximations as well and has been applied widely.

However, one fundamental limitation of the PWB method is that it assumes the field in an enclosure is uniform in the steady state. This is only true when the loss in the enclosure is small. When the loss in an enclosure is high, the internal field is no longer uniform and the PWB method cannot describe this change. The acoustics community has proposed a diffusion equation based model that is able to account for the variation of field due to the presence of high loss. The diffusion model is the main subject of the thesis. It can be derived from the radiative transport of particles in an enclosure. It is a generalization of the PWB method and we have applied it to shielding problems. Initial evaluations have been made with a 2D diffusion model, obtaining promising results. In this thesis, extensive investigations are made to verify a 3D diffusion model.

1.2. Research Scope

The main objective of this thesis is to explore the estimation of shielding effectiveness of populated enclosures in a reverberant environment. A number of methods are reviewed. Two particular analytical methods, the power balance method and its generalization, a diffusion equation model are investigated in detail. These two methods are of interest because they analyse shielding problems from a macroscopic point of view and they do not require the details (such as position, shape) of the contents. Hence, they have a wide applicability. In the thesis, simulations and physical measurements are given in order to compare with theoretical calculations. The research aim can be divided into the following parts:

- To demonstrate that the contents of an enclosure affect its shielding effectiveness and the shielding effectiveness can be predicted by using the absorption cross section of the contents and the transmission cross section of apertures.
- In order to use the power balance method, it is necessary to obtain the absorption cross section of contents. When measuring the ACS of electronic components such as printed circuit boards, their power states are always ignored in previous research. In this thesis, we investigated the influence of power state of contents on their absorption cross section and proved that the power state can be ignored.
- The 2D diffusion model has been studied previously [5]. In this study, we verified the usefulness of a 3D diffusion model in predicting electromagnetic fields inside enclosures.

1.3. Outline of thesis

Chapter 2 provides a general review of the shielding theory as well as several analytical methods to predict shielding effectiveness of enclosures.

Chapter 3 reviews some facilities (open area test site, anechoic chamber and reverberation chamber) and methods (one, two and three antenna methods) to perform shielding measurements.

Chapter 4 introduces the power balance method. Examples will be presented to show that it is necessary to include the contents when predicting the shielding effectiveness of enclosures.

The theory of absorption cross section and its relation with shielding problems is explained. The effect of the power state of contents on the absorption cross section is investigated.

Chapter 5 is all about the diffusion equation based model. Its principles, assumptions and relationship with the power balance method are explained. A number of test scenarios will be provided to demonstrate its usefulness, including an enclosure with different content, electrically large and small aperture and different dimensional ratios. Full wave simulations and physical measurements will be presented as comparison.

Chapter 6 draws the conclusion of the work presented in the thesis. The advantages and limitations of different methods for shielding problems are summarized. Discussions about possible extensions of the current research are made.

Chapter 2

Overview of shielding effectiveness

2.1. Outline of thesis

Shielding is one of the techniques that have been applied to EMC engineering to suppress electromagnetic interference. Any interference that transmits through space can be reduced by proper shielding. The term shield usually refers to an enclosure that (in an ideal case) completely encloses an electronic component [6]. There are two goals of a shield. The first is to prevent the emission of an electronic component to reach outside the boundary of the shield. This is to prevent the emission to influence other components. The second goal is to prevent external emission from coupling to the electronic component, which may cause interference in the component's performance. An illustration of shield can be seen in Figure 2.1 (a).

From the introduction above, it can be seen that a shield serves as a barrier to the transmission of electromagnetic fields. A shielding enclosure is usually made of conductive or magnetic material and it should shield both electric and magnetic fields. The ability of an enclosure to protect its contents from electromagnetic interference is quantified by its shielding effectiveness (SE). Shielding effectiveness can be defined in terms of field or power. From the field point of view, Shielding effectiveness is defined as the ratio of the magnitude of the electric or magnetic field that is incident on the enclosure to the magnitude of the electric or magnetic field that is penetrated through the enclosure [6]:

$$\mathrm{SE} = 20\log_{10}\left|\frac{E_i}{E_0}\right| \tag{2.1}$$

$$\mathrm{SE} = 20\log_{10}\left|\frac{H_i}{H_0}\right| \tag{2.2}$$

where E_i and H_i are the electric and magnetic field that is incident on the enclosure, E_0 and H_0 are the electric and magnetic field that is transmitted through the enclosure. It can be noticed that shielding effectiveness is usually expressed in decibels. If the media on both sides of the

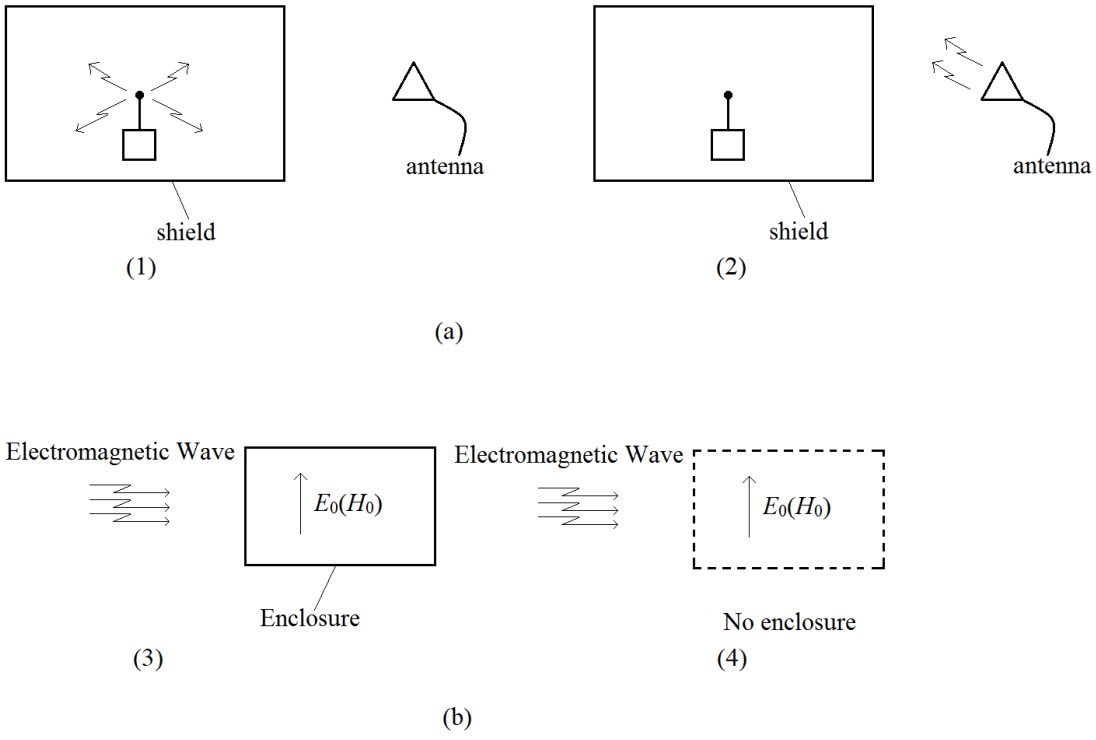

Figure 2. 1. (a). Illustration of the use of a shielding enclosure: (1) to contain radiated emissions; (2) to exclude radiated emissions. (b). Illustration of definition of shielding effectiveness: (3) field with shielding enclosure; (4) field without shielding enclosure.

enclosure is the same, then the two definitions are identical. For near fields and/or different media on two sides of the enclosure, the two are not equivalent. In reality, the definition in terms of electric field in formula (2.1) is usually considered to be the standard [6]. An illustration of the definition of shield effectiveness can be seen in Figure 2.1 (b). From the power point of view, shielding effectiveness is defined as [2]:

$$\mathrm{SE} = 10\log_{10}\frac{S_i}{S_0} \tag{2.3}$$

where S_i is the density of the incident power and S_0 is the density of the internal power, both in W/m^2.

A number of factors affects shielding effectiveness. For an ideal case where an infinite conducting sheet is illuminated by a plane wave, the shielding effectiveness depends on the frequency of the plane wave and the properties of the sheet's material properties (conductivity, relative permittivity and relative permeability). If a shielding enclosure is applied, then the shielding effectiveness is dependent on the position within the enclosure.

Furthermore, if an empty enclosure is made of highly conductive material and contains an aperture, then the shielding effectiveness is determined mainly by the penetration of energy through the aperture. If there are contents, then they have an influence on the shielding effectiveness as well.

2.2. Methods to predict shielding effectiveness

The prediction of shielding effectiveness can be divided into numerical methods and analytical methods. Numerical methods solve Maxwell's equations directly with certain boundary conditions. Theoretically, they can be applied to any enclosure and they are able to model complex structures. There are already a number of commercial software for people to choose. To solve most real world SE problems full wave numerical electromagnetic solvers must be used. However, to reach an exact numerical solution, full wave solvers may take hours or days depending on the complexity of the problem. An EMC designer would usually like to solve a problem in seconds so that the effects of design changes can be observed quickly. This requirement boosts the development of analytical methods, which are usually empirical or semi-empirical and uses approximations. They may not be as accurate as numerical solutions but they need far less computational resources. There are many analytical methods; here we only review a couple of early ones.

One early analytical method is the circuit model proposed by Schelkunoff, which compares the propagation of electromagnetic waves in a shielding enclosure to that of travelling waves along a transmission line [7]. According to Schelkunoff's model, when an electromagnetic wave impinges on a sheet with finite thickness, a portion of the wave is reflected and the rest of it penetrates into the sheet. When the latter reaches the boundary of the sheet, a part of it is reflected again and the rest of it goes to the other side of the sheet. The former part keeps reflecting inside the sheet and every time it reaches either boundary, a part of the wave goes through it. Therefore, the shielding effectiveness of the sheet is the sum of reflection loss, absorption loss and multi-reflection loss.

Another analytical method is the field theory proposed by Kaden [8]. He developed general approaches to calculate eddy currents in certain specific empty enclosures and applied them to nonhomogeneous shielding analysis: spiral shields, shields with apertures and multilayer shields. According to Kaden's theory, when an electromagnetic field incidents on a shielding

enclosure, eddy currents are induced on the surface of the enclosure and they create opposite fields. By using the separation of variables method, we solve Helmholtz's equation in each of the three regions: the space outside the enclosure, the space inside the enclosure and in the wall of the enclosure (usually metal). Combined with boundary conditions, continuity and conservation of the tangent component of the field at each of the enclosure's surfaces to obtain the external and internal field. The shielding effectiveness can be calculated by formula 2.1.

Both Schelkunoff and Kaden's methods lay the foundation of contemporary shielding study. However, their models are only suitable to some idealized geometries. Schelkunoff's method can only be applied to infinite sheet and Kaden's theory is only suitable for some simple structures (plan-parallel, spherical, cylindrical, elliptic, parabolic, toroidal, etc.). Therefore, they do not address many EMC problems in modern electronic systems, nor do they reflect the latest technical advances in shielding study.

More recently, some analytical methods have been developed for applications that are able to be applied to more practical situations. For example, the intermediate level circuit model proposed by Robinson et al. is able to predict the shielding effectiveness of an empty rectangular enclosure with an aperture [9]. For the case where an enclosure is illuminated by a plane wave, the model considers the enclosure as a shorted waveguide and assumes a single mode of propagation. The plane wave is represented by a voltage source and an impedance. The aperture is represented by a length of coplanar strip transmission line, shorted as each end. The shielding effectiveness at a particular point along the central line of the enclosure is simply the ratio of electric field in the absence and presence of the enclosure as described in formula (2.1). Later, attempts have been made to include higher order modes [10], aperture array [11] and apertures on different faces [12] into the circuit model. The intermediate level circuit model is able to provide fast approximations and can be used at early stages of EMC design. However, most of the proposed models ignored the contents of enclosures, and thus, underestimated internal power loss.

As frequency increases, the enclosure becomes electrically large (electrically large means the enclosure supports several modes at the lowest frequency of interest) and over-moded (the criterion of over-mode will be presented in section 3.1.3). The internal electromagnetic environment can be modelled by probabilistic laws. In this case, we can make the

approximation that the enclosure is equivalent to a pseudo-mode stirred reverberation chamber. In other words, when an enclosure is electrically large and over-moded, there is no privileged direction of energy in it. Therefore, high frequency shielding problems can be treated from an average energy point of view.

In order to predict the shielding effectiveness of populated enclosures at high frequencies, the power balance (PWB) method has been introduced [3]. The PWB method assumes that the enclosure is electrically large and the internal field is uniform in the steady state. For steady state conditions, the power transmitted into the enclosure equals the power dissipated inside. Since it only considers average energy, the details of the content's geometry, the shapes of the aperture and the enclosure is no longer important.

As can been introduced, contents affect the shielding effectiveness of an enclosure by absorbing some internal energy. The absorption characteristics of the contents are quantified by their absorption cross sections, which are the effective areas of them that absorb energy. By using the PWB method, the shielding effectiveness is closely related to the absorption cross section of the contents. Besides contents, we also need to consider the influence of apertures. Junqua et al extended the original PWB method and proposed a network formulation for coupled enclosures [13].The details of the power balance method will be provided in chapter 4.

In terms of measurements, absorption cross section is defined as the ratio of absorbed power to the power density of illuminating field. Carlberg et al have shown that absorption cross section can be measured in a reverberation chamber and pointed out that the overall ACSs of densely packed objects are smaller than the sum of individual ACS [14]. In [4], Flintoft et al analysed an enclosure filled with packed printed circuit boards and proposed a segmented power balance model. They proposed an empirical shadowing factor to account for the reduction of ACS due to close proximity of printed circuit boards.

The power balance method assumes that the energy is uniform throughout an enclosure in the steady state. If the loss in the enclosure is high, the energy is no longer uniform and the power balance method cannot predict this change. The acoustics community has proposed a diffusion model that is able to predict the variation of energy due to the presence of high loss. For the first time, Flintoft et al applied the diffusion model to shielding problems and validated

a 2D diffusion model [5]. The diffusion model compares the transport of electromagnetic rays to particles in a cavity. The main subject of this thesis is to further develop this method and verify the usefulness of 3D diffusion model. The details are given in chapter 5.

2.3. Summary

This chapter began with some general principles and concepts of shielding effectiveness. Then some methods for shielding problems were reviewed. Numerical methods produce accurate results but usually require much computing resources. In order to get fast estimations, analytical methods become necessary. Schelkunoff's transmission line model for infinite plane shield and Kaden's analytical methods for symmetrical structures are early attempts to analyse shielding problems and are only suitable to idealized situations.

The intermediate level circuit model stems from the waveguide theory (analogues to EM waves in an enclosure). It is able to estimate resonant frequencies of enclosures with apertures and most of the study centres on empty enclosures only, limiting its applicability.

The power balance method has been used to analyse shielding problems of populated enclosures from an average energy point of view and it does not require the geometry of the contents, but it is accurate only when the loss in the enclosure is low. For moderate or high loss cases, the power balance method is unable to predict the variation of power due to the presence of loss.

The diffusion equation based model is a generalization of the power balance method and it is able to account for such variation. The diffusion model is derived from a radiative of transport theory of particles in an enclosure. A 2D diffusion model has been verified. The main subject of this thesis is to verify the usefulness of a 3D diffusion model.

Chapter 3

Measurement of shielding effectiveness

3.1. Facilities for shielding measurements

Study of shielding effectiveness relies on measurements. A shielding effectiveness measurement usually contains two steps: 1. a reference coupling test; 2. a shielded coupling test [15]. The measurement can be performed in either an open-area test site (OATS), an anechoic chamber or a reverberation chamber. If we hope to investigate the circumstance where there is only a single direction of illumination, then the measurement can be performed in open-area test site or anechoic chamber; if we want to study a multi direction illumination case, then we could use a reverberation chamber to perform the measurement. In this section, we present introductions of all three measurement facilities. It should be noted that in actual cases, an electronic/electrical device is more likely to be exposed to electromagnetic interferences coming from different directions rather than interferences from a single direction. Therefore, all the measurements presented in this thesis were performed in a reverberation chamber and the introduction will mainly focus on reverberation chamber.

3.1.1. Open-area test site

An open-area test site (OATS) is ideally a perfectly flat, infinitely large plane without any obstructions. In reality, such a test site is usually built at places where there are as little ambient electromagnetic interferences as possible. It is suitable for radiated emission test, which measures unintentional release of electromagnetic energy from an electronic/electrical device. The size and shape of an open area test site depends on the measurement distance and whether the equipment under test will be rotated. If rotation is required, the standard ANSI C67.4-2015 recommends an elliptical test site; otherwise a circular site is recommended [16]. Figure 3.1 shows the open area test site at the University of York.

Figure 3. 1. The open area test site at the University of York.

Although shielding effectiveness measurements can be performed in an open area test site, in this work, no measurements were performed in it. Therefore, we will not provide more details about OATS in this thesis.

3.1.2. Anechoic chamber

In actual cases, measurements performed in an open area test site are unavoidably affected by electromagnetic interferences coming from sources like mobile phone or TV stations due to the open nature of the test site. An anechoic chamber can serve as an alternative of an open area test site. Figure 3.2 shows the anechoic chamber at the University of York. It can be seen from the photo that an anechoic chamber is a shielded room with absorbing material covering the internal walls. There are two types of anechoic chambers: semi-anechoic chamber and full anechoic chamber. The difference is that in a semi-anechoic chamber, absorbers do not cover the floor while in a full anechoic chamber the floor is covered. Therefore, a semi-anechoic chamber simulates open area test sites and a full anechoic chamber simulates free space. The cost of building an anechoic chamber is higher than that of an open area test site due to the use of absorbing materials. However, it has the advantages of free from ambient electromagnetic interference.

Figure 3. 2. The anechoic chamber at the University of York.

3.1.3. Reverberation chamber

The concept of reverberation chamber arises from the idea of using resonant cavities to perform radiation measurements, where a small change in boundary condition leads to huge field variation [17]. A reverberation chamber is a screen room with highly conductive inner walls that minimise the absorption of electromagnetic energy. It operates in over-moded region. The most notable difference between a reverberation chamber and an anechoic chamber is that a reverberation chamber is able to provide a uniform electromagnetic environment. Therefore, it is suitable for radiated emission and radiated susceptibility measurements.

Figure 3.3 shows the reverberation chamber at the University of York. It can be seen that a mechanical stirrer is fitted in the chamber. The stirrer can be moved to different orientations to achieve different boundary conditions. The method of mechanical stirring holds a constant frequency while varying the chamber's boundary conditions to obtain an adequate number of modal contributions to the internal field. In this manner, field homogeneity is achieved by averaging the contributions of different modes.

Figure 3. 3. The reverberation chamber at the University of York.

The chamber in figure 3.3 has dimensions of 4.7m×3m×2.37m. The walls are made from zinc plated galvanised mild steel. The relative permeability of the chamber walls is assumed to be unity and a conductivity of 1MS/m was found to give a Q-factor similar to the measured Q-factor (see figure 3.7) at 1GHz. The conductivity of pure zinc (17MS/m) overestimates the Q-factor by a factor of about 10. The real conductivity is presumably highly dependent on the purity and surface finish of the real walls. Steel has a conductivity ranging from 1-7MS/m, depending on the carbon content and production process. In a technical note, Flintoft states that the wall loss dominates the antenna loss (if there is an antenna) above 1GHz and hence the antenna has little influence on the chamber Q-factor at high frequencies (above 1GHz) (see figure 3.7) [18].

For chambers or enclosures that are not convenient to install a mechanical stirrer, frequency stirring is an alternative way to achieve field uniformity [19]. Frequency stirring does not change the boundary condition. Instead, the frequency is allowed to vary over a narrow band of frequency. Then frequency stirring is achieved by averaging the contribution of each mode in that frequency band.

By talking field uniformity, we mean there should be sufficient number of uncorrelated samples in the chamber. The number of uncorrelated samples can be estimated by autocorrelation function (ACF). Later in this chapter, we will show the ACF of S-parameter

measured in the reverberation chamber at the University of York as an example. When using mechanical stirring, more independent samples can be obtained by properly increasing the number of stirrer positions. When using frequency stirring, more independent samples can be obtained by an increase the bandwidth to include more samples. Currently the choice of the bandwidth for frequency stirring is empirical. In [20], Marvin et al compared several bandwidths (5MHz, 10MHz, 20MHz and 50MHz) for frequency stirring in a reverberation chamber and concluded that the wider the bandwidth, the result tend to get closer to an exact value. This is because broader bandwidth means more independent samples are included. However, this does not mean we can choose the bandwidth as wide as we want because it might obscure the original features of the results. For example, in shielding measurements, the shielding effectiveness of an enclosure decreases dramatically at resonant frequencies. If we choose a very wide bandwidth for frequency stirring, then the averaged values get too close to an exact number and the reduction in shielding effectiveness might not be observed.

Other methods to achieve field uniformity in a reverberation chamber include source stirring [21] and load stirring [22].

As has been mentioned, a reverberation chamber operates in over-moded region. In order to illustrate what over-moded means, here we briefly review enclosure resonators. The resonant frequencies of an enclosure or chamber is given by [23]:

$$f(MHz) = 150\sqrt{\left(\frac{k}{l}\right)^2 + \left(\frac{m}{w}\right)^2 + \left(\frac{n}{h}\right)^2} \tag{3.1}$$

where *l* ,*w* and *h* are the length, width and height of the chamber respectively, all in meters. *k*, *m*, and *n* are positive integers 0, 1, 2…… etc. It should be noted that not more than one of them could be zero at the same time. The reverberation chamber at the University of York has dimensions of 4.7m×3m×2.37m. Therefore, the first mode, TE110, is at:

$$f_{TE110} = 150\sqrt{\left(\frac{1}{4.7}\right)^2 + \left(\frac{1}{3}\right)^2} \approx 59.3MHz \tag{3.2}$$

The frequency at which a reverberation chamber can be considered as over-moded is defined as the lowest usable frequency (LUF) and there are different ways to determine the LUF. The IEC standard 61000-4-21:2011 gives an estimate of the lowest useable frequency as the frequency of the 60th mode [24]. The number of modes in a reverberation chamber below (and up to) a certain frequency can be estimated by [24]:

$$N = \frac{8\pi}{3} lwh \left(\frac{f}{c}\right)^3 \tag{3.3}$$

where *c* is light speed and *f* is frequency in Hertz. The frequency of the 60th mode (*N*=60) in the reverberation chamber at the University of York is about 178MHz, which means the lowest useable frequency of the chamber is 178MHz. The American military standard MIL-STD-461F proposed a higher standard in which there should be at least 100 modes in a reverberation chamber before it can be considered usable [25]. In this case, according to formula (3.3), the lowest usable frequency of the chamber is approximately 213MHz.

In [26], Schroeder proposed a more rigorous criterion of the lowest useable frequency that marks the transition from individual resonances to many overlapping modes. The crossover frequency, which is called the Schroeder frequency, is the frequency at which the mode bandwidth to mode spacing is three. The mode bandwidth, *BW*, is given by [27]:

$$BW = \frac{f}{Q} \tag{3.4}$$

where *Q* is the quality factor of the chamber. The mode spacing, Δf, is given by:

$$\Delta f = \frac{c^3}{4\pi V f^2} \tag{3.5}$$

where *c* is the light speed and *V* is the chamber volume. Figure 3.4 shows the mode bandwidth to mode spacing ratio of the empty reverberation chamber at the University of York. It can be seen that the Schroeder frequency of the empty chamber is about 1.7GHz.

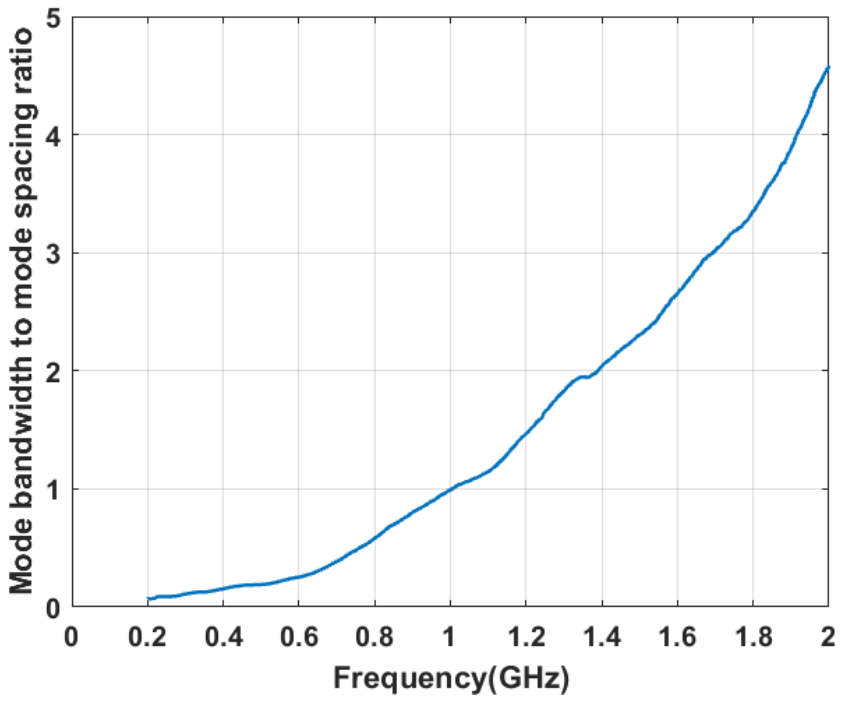

Figure 3. 4. The mode bandwidth to mode spacing ratio of the reverberation chamber at the University of York.

As has been mentioned, one condition to achieve field uniformity in a reverberation chamber, is that there must be enough number of independent samples. When mode tuned method is applied, it is necessary that a change in stirrer position should result in enough change in boundary condition. The number of independent samples, $N_{ms;ind}$, can be calculated from the autocorrelation of the S_{21} parameter between a transmitting antenna and a receiving antenna from a certain frequency and it is given by [28]:

$$N_{ms;ind} = \frac{N_{ms;tot}}{N_{ms;cor}} \tag{3.6}$$

where $N_{ms;tot}$ is the total number of samples and $N_{ms;cor}$ is the number of correlated samples. Figure 3.5 shows the autocorrelation function of S_{21} at different frequencies in the reverberation chamber at the University of York. In the measurement, the stepped stirring technique was used and there were 100 stirrer positions over a full rotation, which means $N_{ms;tot}$=100. Empirically, when the autocorrelation drops below 1/*e*, the change in stirrer positions is sufficient for the samples to be independent. It can be seen that at 500MHz, 1GHz and 2GHz, the number of correlated samples are 20, 5 and 1 respectively. Therefore, according to formula (3.6), the number of independent samples at 500MHz, 1GHz and 2GHz

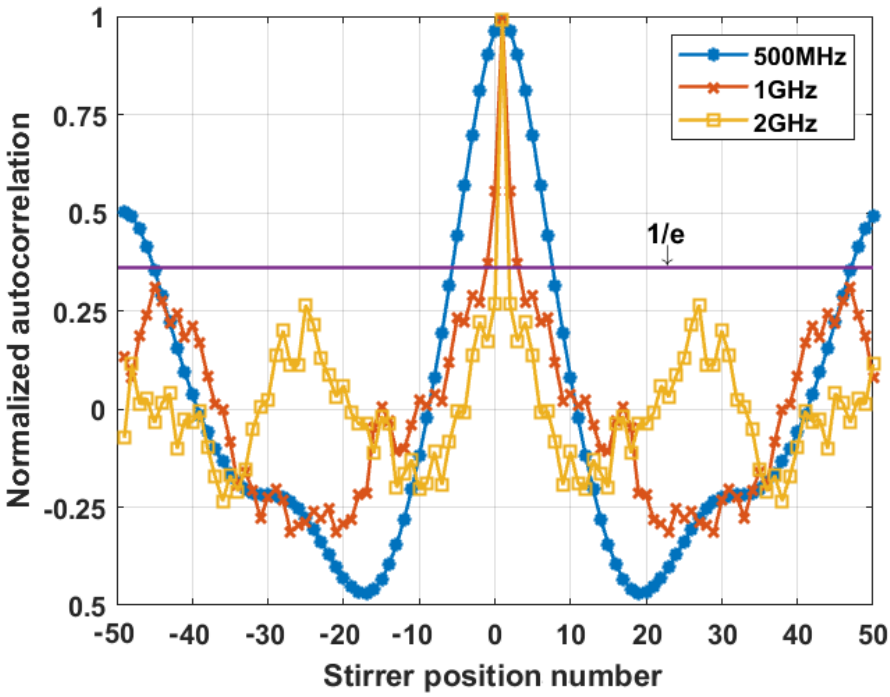

Figure 3. 5. Normalized autocorrelation of S21 for mechanical stirring in the reverberation chamber at the University of York.

are 5, 20 and 100. The number of independent samples determines the variance of the measurements. In order to reduce measurement uncertainty, there should be sufficient independent samples.

When frequency stirring is applied, the number of independent samples, $N_{fs;ind}$, is obtained in the similar way as that for mechanical stirring:

$$N_{fs;ind} = \frac{N_{fs;tot}}{N_{fs;cor}} \tag{3.7}$$

where $N_{fs;tot}$ is the total number of samples and $N_{fs;cor}$ is the number of correlated samples, both for frequency stirring. Figure 3.6 shows the autocorrelation of S_{21} for frequency stirring at different centre frequencies in the reverberation chamber at the University of York. The autocorrelation function of S_{21} was calculated by:

$$\mathrm{ACF}(S_{21}) = \mathrm{IFFT}\{\mathrm{FFT}(S_{21}) \cdot [\mathrm{FFT}(S_{21})]^{*}\} \tag{3.8}$$

where FFT and IFFT stand for Fast Fourier Transform and Inverse Fast Fourier Transform respectively. The symbol * means conjugate. The normalized autocorrelation function is obtained by:

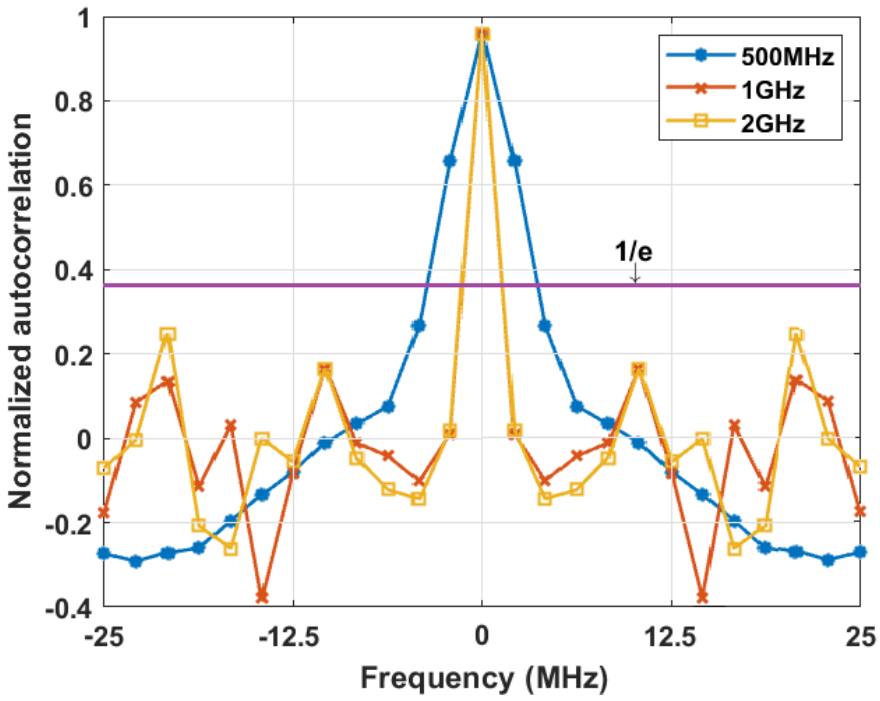

Figure 3. 6. Normalized autocorrelation of S21 for frequency stirring in the reverberation chamber at the University of York.

$$\text{Normalized ACF}(S_{21}) = \frac{\text{ACF}(S_{21}-\langle S_{21}\rangle)}{N[\text{std}(S_{21})]^2} \tag{3.9}$$

where std means standard deviation and N is the total number of S_{21}.

The S_{21} was measured from 200MHz to 20GHz with 10001 equally spaced points. Therefore, the frequency spacing between measurement points is 1.98MHz. The bandwidth for frequency stirring is set to be 50MHz, which means that there are $N_{fs;tot}$=25 samples within this bandwidth. From the result, it can be seen that at 500MHz, 1GHz and 2GHz, the number the number of correlated samples are 3, 1 and 1 respectively.

If both mechanical stirring and frequency stirring are applied to the same measurement, the total number of independent samples is:

$$N_{ind} = N_{ms;ind}N_{fs;ind} \tag{3.10}$$

The quality factor, Q, in formula (3.4) is a key quantity for a reverberation chamber. It describes how fast energy decays in the chamber and is defined as [3]:

$$Q = \omega \frac{U_s}{P_d} \tag{3.11}$$

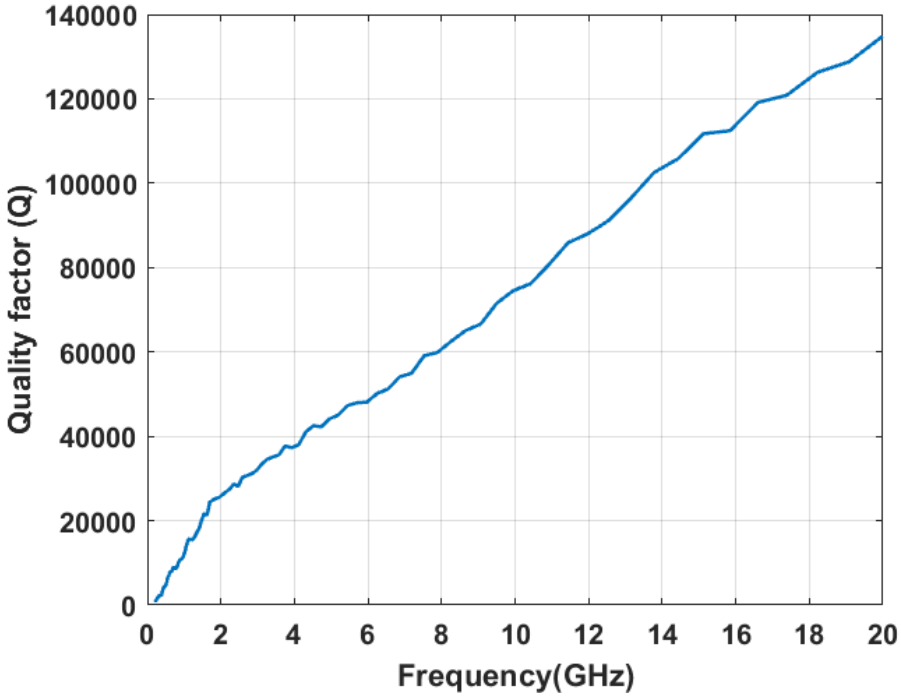

Figure 3. 7. Measured quality factor of the empty reverberation chamber at the University of York.

where ω is the angular frequency, U_s is the steady state energy and P_d is the dissipated power. The steady state energy, U_s, is the product of chamber volume and energy density, w:

$$U_s = WV \tag{3.12}$$

The energy density is calculated from the total (rms) electric field:

$$W = \varepsilon_0 E_{tot}^2 \tag{3.13}$$

where ε_0=8.85×10^{-12}F/m is the permittivity of free space.

In actual measurements, The Q of a reverberation chamber is calculated from the S-parameters between a transmitting antenna and a receiving antenna [14]:

$$Q = \eta_t \eta_r \frac{16\pi^2 V}{\lambda^3} \frac{\langle |S_{21}|^2 \rangle}{(1-|\langle S_{11} \rangle|^2)(1-|\langle S_{22} \rangle|^2)} \tag{3.14}$$

where λ is the wavelength, S_{ii} (i=1,2) is the reflection coefficient of the antenna, η_t and η_r are the efficiency of the transmitting antenna and receiving antenna. The symbol <·> means an average over a statistical ensemble of systems, for example, due to mechanical or frequency

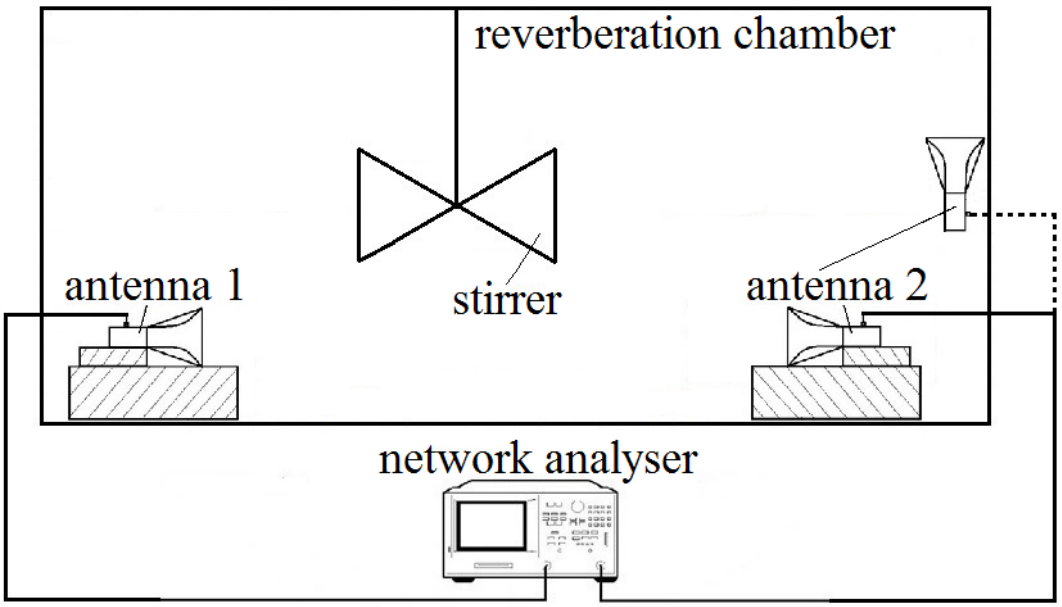

Figure 3. 8. Diagram of the K-factor measurements in the reverberation chamber at the University of York.

stirring in a reverberation chamber. Figure 3.7 shows the measured *Q* of the 4.7m×3m×2.37m reverberation chamber at the University of York. It can be seen that the quality factor rises gradually with frequency and reaches about 135000 at 20GHz. Here we used two identical blade antennas and assume η=1. The photo of the antenna can be seen in chapter 4.

The K-factor is another important quantity of a reverberation chamber. It quantifies the preponderance of non-stochastic energy in the chamber and it is defined as the ratio of stochastic energy to non-stochastic energy. In a reverberation chamber, non-stochastic energy represents direct coupling between transmitter and receiver. In real measurements, in order to get good field uniformity, the K-factor should be kept as low as possible. Currently there is no standard about the level of K-factor, empirically if the K-factor in a reverberation chamber is less than 0.2, then the field in the chamber is considered to be sufficiently uniform.

Figure 3.8 shows the configuration of K-factor measurement in the reverberation chamber at the University of York. Two measurements were performed. In measurement 1, two antennas were put on the floor. In measurement 2, antenna 1 was in the same position while antenna 2 was fitted on the wall. For both measurements, there were 100 stirrer positions over a full

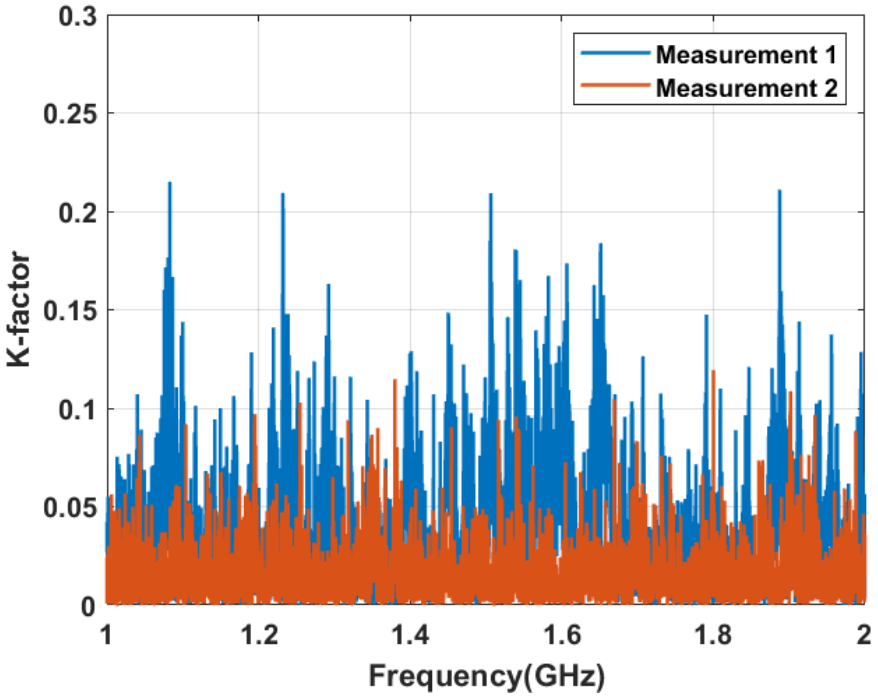

Figure 3. 9. Measured K-factor in the reverberation chamber of the University of York.

rotation and a vector network analyser was used to collect S-parameters. The K-factor is given by [29]:

$$K = \frac{|\langle S_{21}\rangle|^2}{\langle |S_{21} - \langle S_{21}\rangle|^2\rangle} \tag{3.15}$$

Figure 3.9 shows the measured K-factor in the empty reverberation chamber at the University of York. It can be noticed that the two measurement scenarios led to quite different results. This suggests that the K-factor is not an intrinsic property of the chamber, but depends on a number of factors, such as the position of antennas or the presence of other scattering objects.

3.2. Methods for shielding effectiveness measurements

The shielding effectiveness of an enclosure can be measured by using one, two or three antennas. It should be noted that the resonant frequencies of an enclosure do not change with different methods or measurement environments (reverberation chamber, anechoic chamber or open area test site).

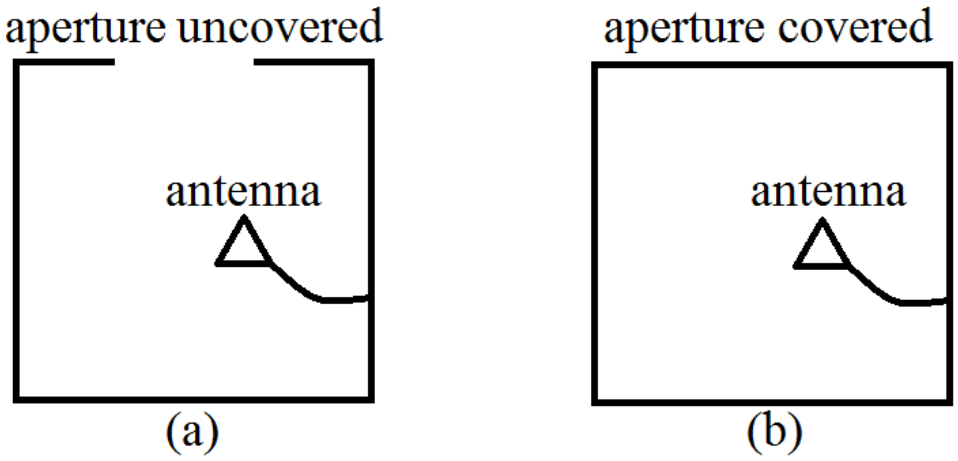

Figure 3. 10. Diagram of SE measurement by using one antenna. (a) An enclosure with an aperture uncovered. (b) An enclosure with an aperture covered.

3.2.1. One antenna method

In [30], Xu et al proposed a one-antenna method to measure the shielding effectiveness of electrically large enclosures. For an enclosure with an aperture, the shielding effectiveness can be estimated by comparing the quality factor (Q) with the aperture covered and uncovered:

$$SE = \frac{\left(Q_u^{-1} - Q_c^{-1}\right)^{-1}}{Q_u} \tag{3.16}$$

where Q_u and Q_c are the quality factors of the enclosure with the aperture uncovered and covered respectively.

In the time domain, the relationship between the quality factor and the time constant, τ, of an enclosure is given by [3]:

$$Q = \omega\tau \tag{3.17}$$

where ω is the angular frequency. Therefore, formula (3.14) can be expressed alternatively as:

$$SE = \frac{\tau_c}{\tau_c - \tau_u} \tag{3.18}$$

where τ_u and τ_c are the time constants of the enclosure with the aperture uncovered and covered.

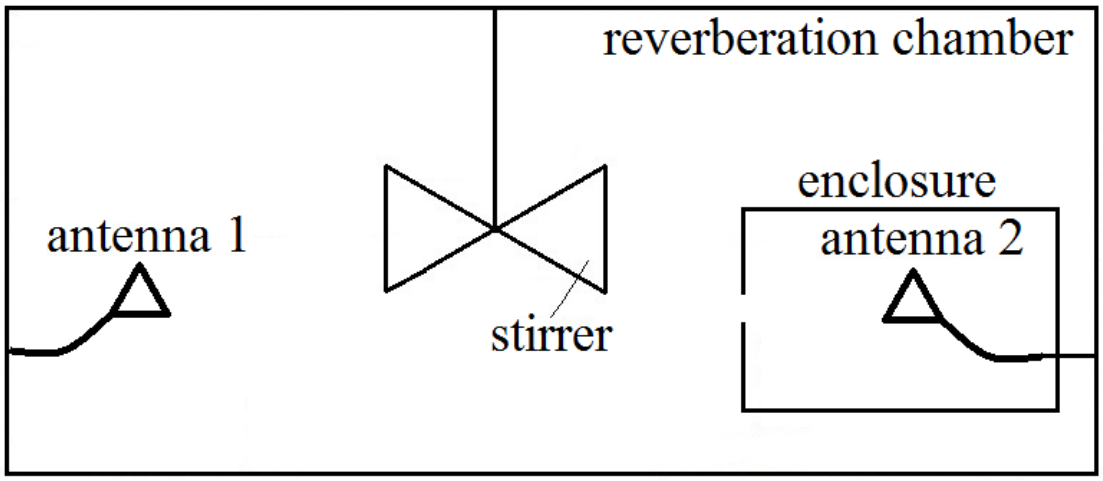

Figure 3. 11. Diagram of SE measurement by using two antennas.

Figure 3.10 shows the test configuration. During the measurement, an antenna is installed in the enclosure under test. First, it measures the $S_{11;u}$ with the aperture uncovered; then the $S_{11;c}$ with the aperture covered. The shielding effectiveness of the enclosure is:

$$SE = \frac{\langle |S_{11;c} - \langle S_{11;c} \rangle|^2 \rangle}{\langle |S_{11;c} - \langle S_{11;c} \rangle|^2 \rangle - \langle |S_{11;u} - \langle S_{11;u} \rangle|^2 \rangle} \tag{3.19}$$

The advantages of the one antenna method are simple measurement setup and cost effectiveness. There is no need to use a chamber for the measurement. Despite the simplicity, we did not use this method for our measurements. Because the main subject of this thesis, the diffusion model, requires the presence of a diffuse field. The one antenna method does not use a chamber, therefore the presence of a diffuse field in not guaranteed. The details of the diffusion model will be presented in chapter 5.

3.2.2. Two-antenna method

The two-antenna method comes from the definition of shielding effectiveness as has been expressed in formula (2.1). Figure 3.11 shows the diagram of two-antenna measurement. One antenna is outside the enclosure and the other one is insider it. First, they measure the $S_{21;i}$ with the presence of the enclosure; then $S_{21;o}$ with the absence of the enclosure. The shielding effectiveness is:

$$SE = \frac{S_{21;o}}{S_{21;i}} \tag{3.20}$$

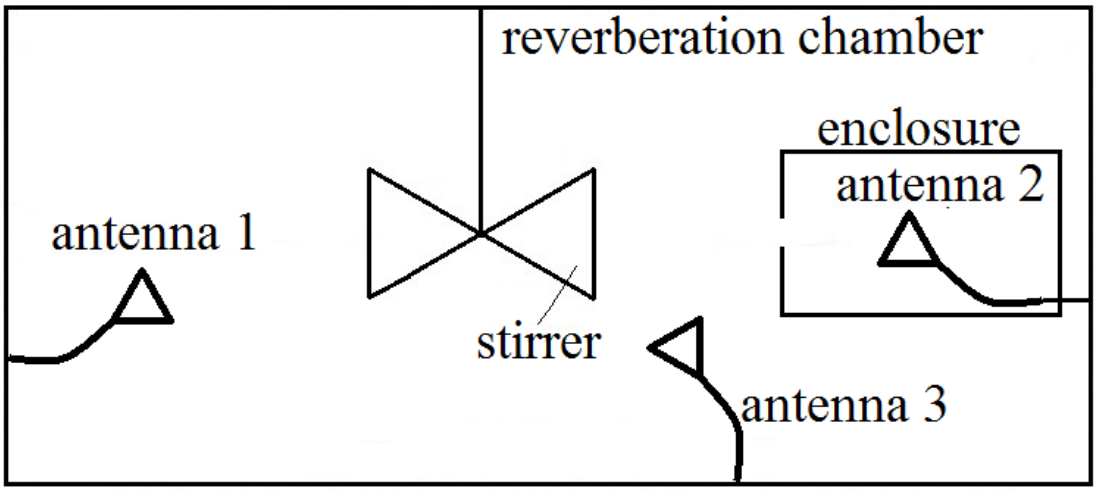

Figure 3. 12. Diagram of SE measurement by using three antennas.

The measurement can be performed in either reverberation chamber, anechoic chamber or open area test site. The disadvantage of this method is that we have to remove the enclosure during the measurement and this disturbs the measurement configuration. In addition, if the enclosure is heavy, it might not be convenient for its removal.

3.2.3. Three-antenna method

The IEEE standard 299.1 introduced a three-antenna method to measure shielding effectiveness of enclosure in reverberation chamber [31]. Figure 3.12 shows the diagram of the measurement set up. A third antenna is introduced as a reference antenna. During the measurement, there is no need to remove the enclosure. The S-parameters between antenna 1 and antenna 2 are collected first; then those between antenna 1 and antenna 3 are collected. The shielding effectiveness is estimated by:

$$SE = \frac{\langle |S_{31}|^2 \rangle}{\langle |S_{21}|^2 \rangle} \frac{1-|\langle S_{22} \rangle|^2}{1-|\langle S_{33} \rangle|^2} \tag{3.21}$$

The second term of formula (3.21) is the mismatch correction factor. The three-antenna method assumes that after correcting for mismatch, the external reference antenna and internal probe antenna behave in an identical way. Most of the shielding measurements presented in chapter 4 and 5 were performed by using the three-antenna method, because during the measurements, the only thing we had to move was a cable. Therefore, this method has the least perturbation to the measurement set up.

3.3. Summary

This chapter is about the facilities and methods for shielding effectiveness measurements. The shielding effectiveness of an enclosure can be measured in either an open area test site, an anechoic chamber or a reverberation chamber. The first two facilities provide a refection free environment while a reverberation chamber creates a uniform EM environment by multiple reflections from chamber walls and a mechanical stirrer that constantly change boundary conditions. Since most of the measurements in this thesis were performed in a reverberation chamber, it is introduced with more details. The lowest useable frequency, number of independent samples, quality factor and K-factor of the reverberation chamber at the University of York were provided.

The shielding effectiveness of an enclosure with an aperture can be measured by using one, two or three antenna methods. The one-antenna method requires the S_{11} parameter without and with the aperture. The two-antenna method measures the S_{21} parameter in the absence and presence of the enclosure. The three-antenna method compares S_{21} parameter between the transmitting antenna and the receiving antenna and that between the transmitting antenna and the reference antenna. Most of the shielding measurements presented later in this thesis were performed by using the three-antenna method because it has the least perturbation to the measurement configuration.

Chapter 4

The power balance method

4.1. Example of influence of contents on shielding effectiveness

The earliest models of shielding effectiveness focus mainly on empty enclosures. In reality, an enclosure always has contents that affect the internal field. This effect has been studied experimentally for many years. For example, Bakker et al used dissipative dielectric blocks to suppress resonance problems in shielded semi-anechoic rooms [32]. Thomas et al included printed circuit board in a circuit model for enclosure shielding problems by treating the board as a slab of dielectric [33]. Wallyn et al included printed circuit board in simulations of enclosures by modelling them as thin sheets of perfect electric conductors [34].The annex K of the aforementioned IEEE standard 299.1 describes how to use absorbing (dissipative) materials in equipment enclosures to measure its shielding effectiveness. More recently, Flintoft et al quantified printed circuit boards by their absorption cross sections in high-frequency shielding assessment [4]. The results presented in these work show that the contents in an enclosure absorb some of internal energy; hence, the field in a populated enclosure is lower than that in an empty enclosure. According to formula (2.1), when E_0 reduces, SE increases. Therefore, it is important to take contents into account when analysing shielding problems.

As a demonstration to begin with, we measured the shielding effectiveness of a personal computer enclosure with and without the contents to show their effect on shielding effectiveness. Figure 4.1 shows the personal computer enclosure under test. It has dimensions of 370mm×180mm×350mm. The side panel of the enclosure is removable and a hole was drilled on it to install a probe antenna. The measurement was performed in the reverberation chamber at the University of York by using the two-antenna method described in section 3.2.2. Figures 4.2 and 4.3 show the photos of the measurement configuration with and without the enclosure. The transmitting antenna, which is a blade antenna [35], and the enclosure were at two opposite corners of the chamber. The shielding effectiveness was measured from 2GHz to 20GHz with 10001 equally spaced points. We used the stepped

Figure 4. 1. Photos of the computer enclosure under test. (a) Front view. (b) Side view of the empty enclosure. (c) Side view of the loaded enclosure. (d) The front panel showing the position of the probe antenna.

Figure 4. 2. Photo of the shielding effectiveness measurement configuration with the presence of the computer enclosure.

stirring technique and the chamber was tuned using a mechanical stirrer with 100 equally spaced positions and frequency stirring was also employed with a bandwidth of 50MHz. There are 27 points within this bandwidth. By calculating the autocorrelation function, we know that the 100 stirrer positions are independent of each other and so do the 27 points within 50MHz (the autocorrelation function is not presented here). Therefore, according to formula (3.10), there are totally 2700 independent samples, which we believe is sufficient for our measurement. A network analyser measured the S-parameters between the transmitting antenna and the probe antenna and the shielding effectiveness was calculated by using formula (3.20).

Figure 4. 3. Photo of the shielding effectiveness measurement configuration with the absence of the computer enclosure.

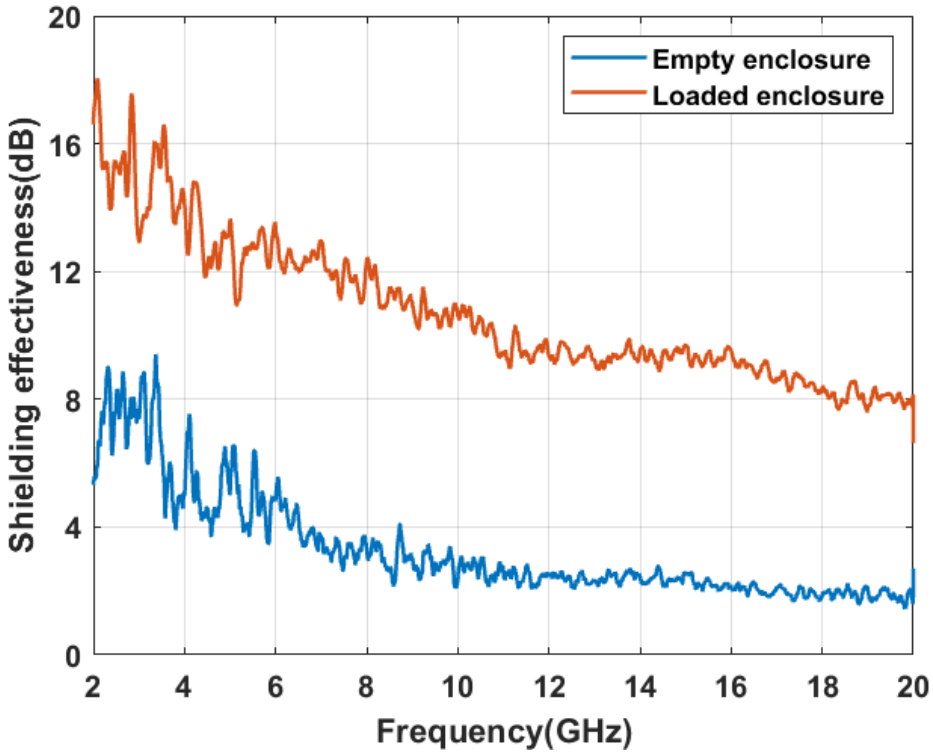

Figure 4. 4. Measured shielding effectiveness of the computer enclosure with and without the contents.

Figure 4.4 shows the measured shielding effectiveness of the computer enclosure with and without the contents. It can be seen that with the presence of the contents, the shielding effectiveness is approximately 6dB higher than that without the contents. As has been mentioned, this is because the contents absorb some energy and thus reduce the internal field. The comparison shows that the contents might have a great influence on the shielding effectiveness and we must take them into account when analysing shielding problems.

4.2. The basics of the power balance method

The aforementioned Robinson's intermediate level circuit model (ILCM) is able to provide fast approximations and predict resonant frequencies of enclosures. Although attempts have been made to include higher order modes and off-centre apertures [36], the circuit model could be of limited use when it comes to loaded enclosures. Because in reality, it would be insurmountable to find circuital alternatives for every content in it. In addition, ILCM is designed for non-reverberant regime where only a few modes exist and the field does not comply with Gaussian distribution. In reverberant regime where electromagnetic field tends to be uniform, shielding problems can be analysed from a power point of view.

Hill et al have proposed the power balance method that accounts for the contents of an enclosure from a macroscopic point of view [3].The main assumptions of the method are: 1. in the steady state, the distribution of power in uniform throughout the enclosure; 2. The dimension of the enclosure is much larger than the wavelength. The theory stems from electromagnetic topology where one large problem is divided into several smaller ones. In the steady state, the energy enters an enclosure equals to the energy dissipated inside. If the enclosure has an aperture, contents and an antenna inside it, then the dissipated power P_d in formula (3.11) can be written as the sum of four terms:

$$P_d = P_{d1} + P_{d2} + P_{d3} + P_{d4} \tag{4.1}$$

where P_{d1} is the power dissipated in the enclosure walls, P_{d2} is the power absorbed in the contents, P_{d3} is the power comes out through the aperture and P_{d4} is the power lost in the loads of the antenna. Accordingly, the quality factor of the enclosure is expressed as:

$$Q^{-1} = Q_1^{-1} + Q_2^{-1} + Q_3^{-1} + Q_4^{-1} \tag{4.2}$$

where $$Q_i = \omega \frac{U_s}{P_{di}}, \ i = 1,2,3,4 \tag{4.3}$$

Here ω is the angular frequency and U_s is the energy in the enclosure.

It is evident that the smallest Q_i is the largest contributor to the overall quality factor. Consider formulas (3.11), (3.12) and (3.13), it is useful to write the relationship between power density and energy density within the enclosure:

$$S_0 = \frac{E_{tot}^2}{\eta_0} = cW \tag{4.4}$$

where η_0=377Ω is the free space impedance, E_{tot} is the total (RMS) electric field, c is light speed and W is energy density.

Hill et al determined the expression of wall loss Q_1 from the skin depth approximation. In a reverberant environment, wall loss is obtained by averaging losses over all plane wave angles and polarisations [37]:

$$Q_1 = \frac{3V}{2\mu_r A\delta} \tag{4.5}$$

where μ_r, A and δ are the relative permeability, area and skin depth of the enclosure walls respectively. V is the volume of the chamber. μ_r and δ are given by:

$$\mu_r = \frac{\mu_w}{\mu_0} \tag{4.6}$$

$$\delta = \sqrt{\frac{2}{\omega\mu_w\sigma_w}} \tag{4.7}$$

where μ_0=4π×10^{-7}H/m is the vacuum permeability. μ_w and σ_w are the permeability and conductivity of the enclosure walls.

The power absorbed by the contents, P_{d2}, can be expressed as the product of power density S_0 and the absorption cross section of the contents $\sigma_{a;con}$:

$$P_{d2} = S_0\sigma_{a;con} \tag{4.8}$$

The absorption losses are derived from formulas (3.12), (4.3), (4.4) and (4.8):

$$Q_2 = \frac{2\pi V}{\lambda\sigma_{a;con}} \tag{4.9}$$

Hill et al pointed out that the absorption cross section of a dissipative object depends on incident angles and polarisations of plane waves. The absorption losses are obtained by averaging losses over all plane waves.

The aperture leakage is quantified by:

$$Q_3 = \frac{4\pi V}{\lambda \sigma_t} \tag{4.10}$$

where σ_t is the transmission cross section of the aperture. The transmission cross section of an aperture relies on angles and polarisations of incident plane waves. If there is a plane wave of power density S_i incident on an enclosure with an aperture, the power P_t transmitted into the enclosure is:

$$P_t = \sigma_t S_i \tag{4.11}$$

The power dissipated in the load of the antenna is given by:

$$P_{d4} = S_0 A_e \tag{4.12}$$

where A_e is the effective area of the antenna and it is calculated by [38]:

$$A_e = \frac{\lambda^2}{8\pi} \tag{4.13}$$

Assuming there is a matched load, the antenna loss can be derived by formulas (3.12), (4.3), (4.4) and (4.13):

$$Q_4 = \frac{16\pi^2 V}{\lambda^3} \tag{4.14}$$

The basic assumption of the power balance method is that, for steady state conditions, the power transmitted into the enclosure is equal to the power dissipated inside:

$$P_t = P_d \tag{4.15}$$

Substituting formulas (3.12), (4.3), (4.4) and (4.11) into (4.15) yield the shielding effectiveness of the enclosure:

$$SE = \frac{S_i}{S_0} = \frac{2\pi V}{\sigma_t \lambda Q} \tag{4.16}$$

It can be seen that the shielding effectiveness of an enclosure is related to the absorption cross section of the contents and transmission cross section of the aperture.

When calculating the power that leaks out through the aperture P_{d3}, Hill et al assumed that the field can be approximated by a superposition of plane waves of all incident angles and polarisations, but only planes waves the propagates towards the aperture contribute to the transmitted power. Therefore, they introduced a factor ½ in the product:

$$P_{d3} = \frac{S_0 \sigma_t}{2} \tag{4.17}$$

In chapter 5, we will present the details of using a superposition of plane waves to simulate a reverberant environment. We will show that 36 plane waves coming from a whole sphere is sufficient to create such an environment and if we only use the 18 plane waves that propagates towards the aperture, there will be a 2dB to 3dB difference in the result (the comparison between 36 and 18 plane waves is not presented here). Therefore, the factor ½ should be omitted. In accordance with this alteration, formula (4.10) should be:

$$Q_3' = \frac{2\pi V}{\lambda \sigma_t} \tag{4.18}$$

In [4], Flintoft et al used the absorption cross section of walls $\sigma_{a;wall}$ to calculate wall loss Q_1 in the same way Hill et al used to obtain content loss:

$$Q_1' = \frac{2\pi V}{\lambda \sigma_{a;wall}} \tag{4.19}$$

In this case, if the enclosure is empty, substituting formulas (4.18) and (4.19) to (4.16), we obtain the shielding effectiveness of the empty enclosure:

$$SE_e = 1 + \frac{\sigma_{a;wall}}{\sigma_t} \tag{4.20}$$

Similarly, if the enclosure is populated, substituting formulas (4.9), (4.18) and (4.19) to (4.16), the shielding effectiveness SE_p is:

$$SE_p = 1 + \frac{\sigma_{a;wall} + \sigma_{a;con}}{\sigma_t} = 1 + \frac{\sigma_{a;wall}}{\sigma_t} + \frac{\sigma_{a;con}}{\sigma_t} = SE_e + \frac{\sigma_{a;con}}{\sigma_t} \tag{4.21}$$

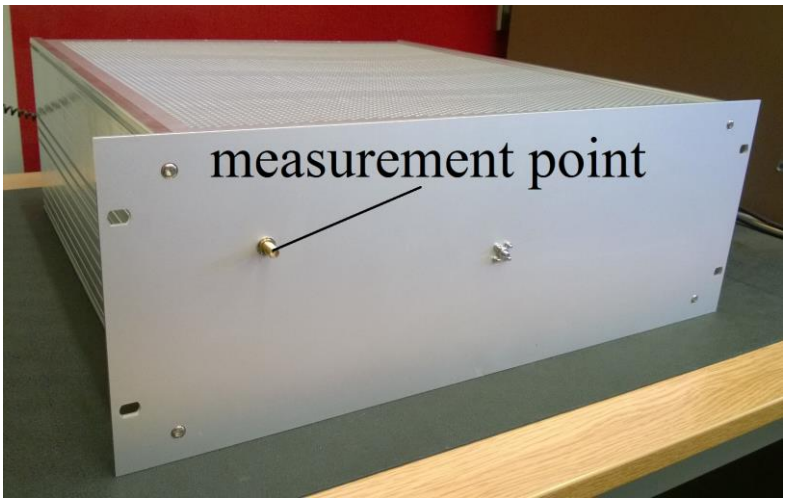

Figure 4. 5. Photo of the enclosure, showing the measurement point.

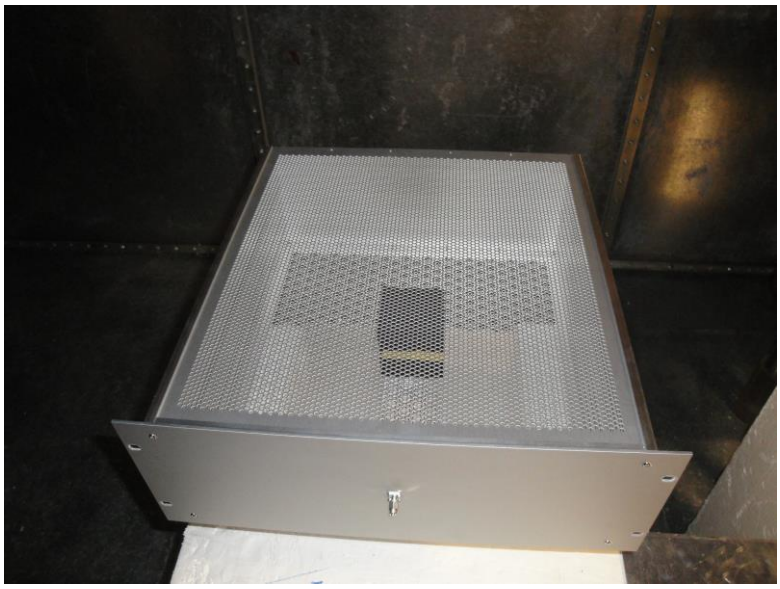

Figure 4. 6. Photo of the top view of the enclosure, showing the absorbing cube inside it.

To demonstrate formula (4.21), we measured the shielding effectiveness of an enclosure shown it Figure 4.5. It is made of highly conductive material and has dimensions of 465mm×430mm×170mm. The measurement point is in the front face. Figure 4.6 is the top view of the enclosure. There are a total 14784 circular apertures in the enclosure (7392 on the top face and 7392 on bottom face) and they have the same radius of 2mm.

We put an absorbing cube with dimensions of 55mm×55mm×55mm at the centre of the enclosure. The details of the material of this cube will be introduced in chapter 5.

Figure 4. 7. Photo of the shielding effectiveness measurement configuration in the reverberation chamber at the University of York.

The measurements were performed in the reverberation chamber at the University of York by using the three-antenna method described in section 3.2.3. Figure 4.7 shows the measurement set up. The blade antenna fitted on the wall was the transmitting antenna. Another blade antenna on a piece of polystyrene support was the reference antenna. The enclosure was put on another block of polystyrene support and there was a small probe antenna in it.

The stepped stirring technique was applied and the chamber was tuned by the mechanical stirrer with 100 equally spaced positions over a full rotation. Frequency stirring with a bandwidth of 50MHz was also applied to smooth the results. A network analyser was used to collect the S-parameters first between the transmitting antenna and the probe antenna, then between the transmitting antenna and the reference antenna. The shielding effectiveness of the empty and loaded enclosure was calculated by using formula (3.21) from 2GHz to 20GHz.

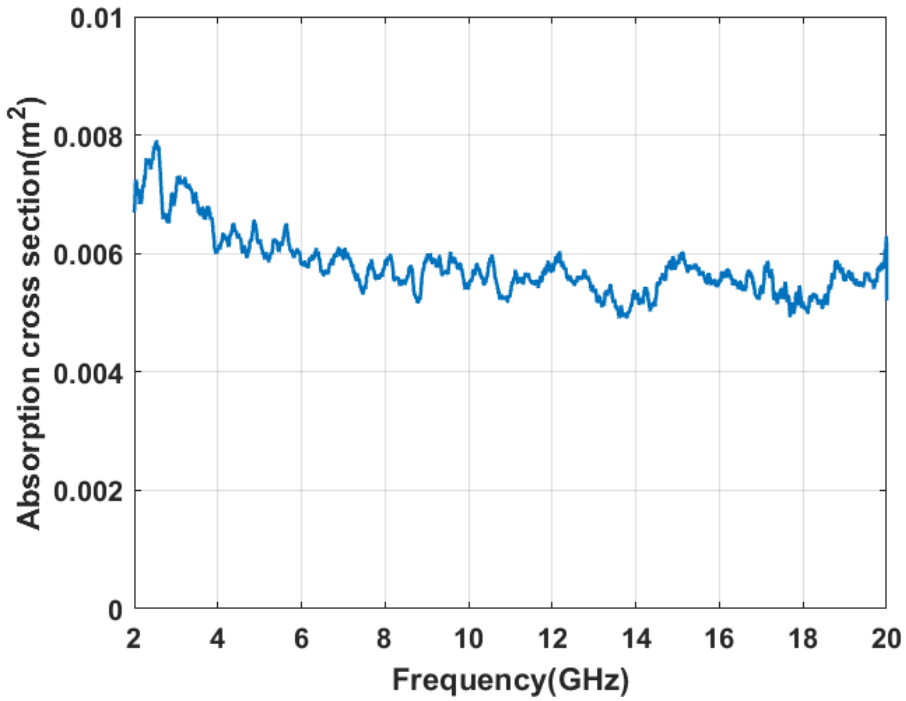

Figure 4. 8. Measured absorption cross section of the 55mm×55mm×55mm absorbing cube.

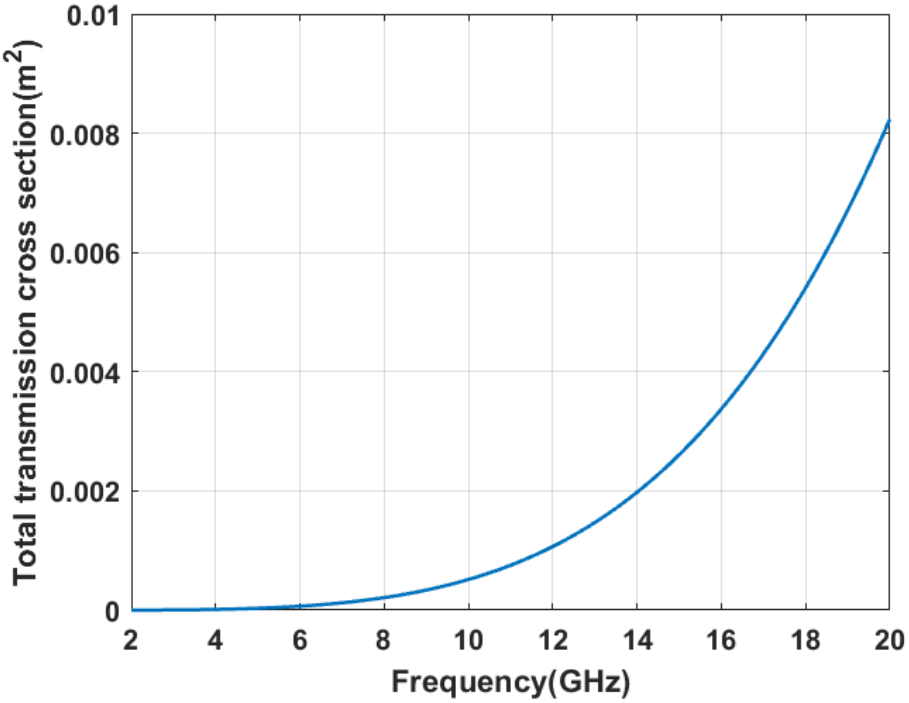

Figure 4. 9. Calculated total transmission cross section of the 14784 r=2mm circular apertures on the enclosure. The cut-off frequency of r=2mm circular aperture is above 20GHz and thus not showing in the figure.

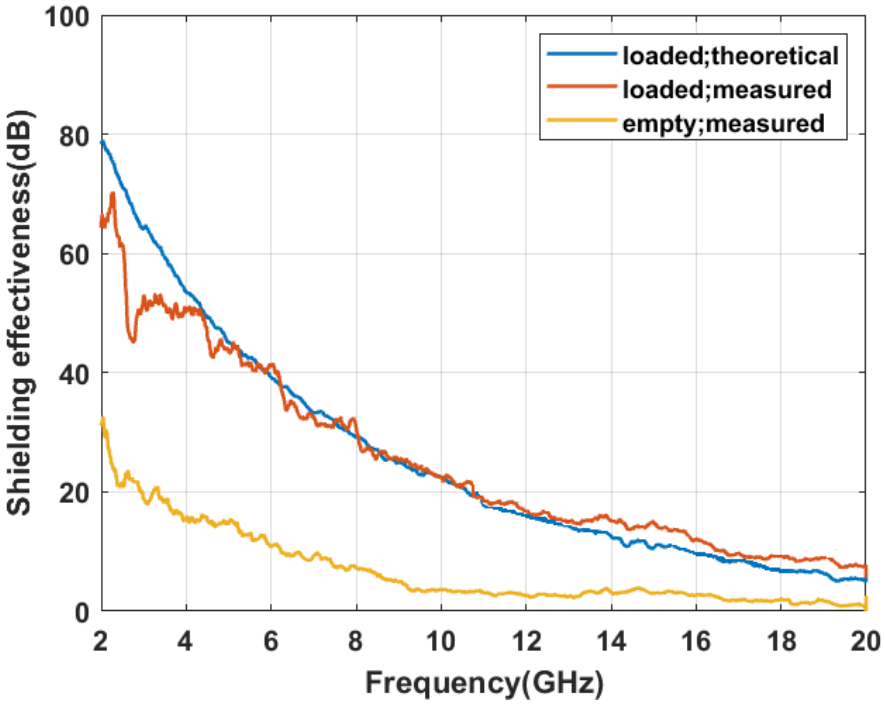

Figure 4. 10. Comparison between measured shielding effectiveness of the empty enclosure, measured shielding effectiveness of the enclosure with a 55mm×55mm×55mm absorbing cube and calculated shielding effectiveness of the enclosure with the same cube.

The absorption cross section of the cube and the total transmission cross section of the apertures have been measured and calculated previously. Here we only show the results. Later in this chapter, we will present the methods for measuring absorption cross section and calculating transmission cross section.

Figure 4.8 shows the measured absorption cross section of the 55mm×55mm×55mm absorbing cube, which is about 0.006m^2. Figure 4.9 shows the total transmission cross section of all the apertures on the enclosure. It can be seen that below the cut-off frequency, which is about 30.8GHz, the transmission cross section of an aperture is dependent on frequency. The method to calculate transmission cross section will presented in the following section.

By using formula (4.21), we calculated the shielding effectiveness of the 4U enclosure with the cube and compared the theoretical calculation with physical measurement. Figure 4.10 shows the comparison. The theoretical calculation is in good agreement with measurement at high frequency, demonstrating the usefulness of formula (4.21). Below 4GHz, the agreement is not good. This is because this are limited number of modes in the enclosure at

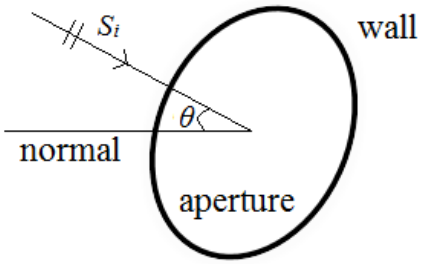

Figure 4. 11. Diagram of an external field incident on an aperture of arbitrary shape.

low frequency the internal field is not sufficiently reverberant. The shielding effectiveness of the empty enclosure is much lower than that of the loaded one. This fact proves again that contents might have a great influence on the shielding effectiveness.

4.3. Calculation of transmission cross section

The transmission cross section of an aperture shows its ability to transmit energy and it is defined as the ratio of transmitted power to power density. In [3], Hill stated a method to calculate the transmission cross section of an aperture of arbitrary shape. The method is based on the theory for electromagnetic penetration through apertures on an infinite, perfectly conducting plane [39]. He assumed that the thickness of the plane is small. Figure 4.11 shows a plane wave with power density S_i incident on an aperture in a perfectly conducting plane. The aperture has an area of A and the incident polar angle is ϑ.

If the aperture is electrically small, the polarizability theory yields a transmission cross section that is proportional to frequency to the fourth power [40]:

$$\sigma_t = Ck^4 \tag{4.22}$$

where k is the wave number. C depends on incident angle, the size and shape of the aperture, but is independent of frequency.

If the aperture is electrically large, the geometrical optics approximation yields:

$$\sigma_t = A\cos\theta \tag{4.23}$$

According to formula (4.22), it is clear that the transmission cross section is independent of frequency. For this case, the average transmission cross section is:

$$\sigma_t = \frac{A}{2\pi}\int_0^{2\pi} d\varphi \int_0^{\pi/2} sin\theta cos\theta d\theta = \frac{A}{2} \tag{4.24}$$

where φ is the azimuth angle of the plane wave. Hill restricted ϑ to π/2 because the plane wave is only incident on one side of the plane.

In [40], Bethe points out that an aperture in a perfectly conducting plane can be approximated by the field of an electric and magnetic dipole. The fields of the dipoles are related to their respective constants of proportionality that are only the functions of the shape and size of the aperture. These constants are known as the electric and magnetic polarizabilities of an aperture.

In a technical report, Junqua et al stated that the constant *C* in formula (4.22) can be calculated from the polarizability of apertures [41]. The polarizability of an aperture is dyadic quantity and it represents the moment of the equivalent electric and magnetic dipoles. The magnetic dipole is in the plane of the aperture while the electric dipole is in the direction of the normal.

The power transmitted through the aperture depends on its incident angle ϑ. When electric field is parallel to the plane of incidence, the polarisation is called parallel polarisation. When magnetic field is parallel to the plane of incidence, the polarisation is named perpendicular polarisation. The expressions for parallel polarisation are (in a Cartesian coordinate system):

$$\begin{aligned} \sigma_{t//}^{x} &= \frac{4k^4}{3\pi}(\alpha_{mx}^2 + \alpha_e^2 sin^2\theta) \\ \sigma_{t//}^{y} &= \frac{4k^4}{3\pi}\left(\alpha_{my}^2 + \alpha_e^2 sin^2\theta\right) \end{aligned} \tag{4.25}$$

where α_e is the electric polarizability, α_{mx} and α_{my} are magnetic polarizability along *x* and *y*-axis directions respectively. The expressions for perpendicular polarisation are:

$$\begin{aligned} \sigma_{t+}^{x} &= \frac{4k^4}{3\pi}(\alpha_{mx}^2 cos^2\theta) \\ \sigma_{t+}^{y} &= \frac{4k^4}{3\pi}\left(\alpha_{my}^2 cos^2\theta\right) \end{aligned} \tag{4.26}$$

If the aperture is illuminated by a random plane wave, Junqua et al defined the transmission cross section as:

$$\sigma_t = \frac{1}{2}\cdot\frac{1}{4}\int_0^{\frac{\pi}{2}}\left(\sigma_{t//}^{x} + \sigma_{t//}^{y} + \sigma_{t+}^{x} + \sigma_{t+}^{y}\right) sin\theta d\theta \tag{4.27}$$

Table 4. 1. Polarizabilities of various apertures in an infinite plane [39] [42].

Aperture	$\boldsymbol{\alpha_e}$	$\boldsymbol{\alpha_{mx}}$	$\boldsymbol{\alpha_{my}}$
Circle radius=*r*	$\frac{2r^3}{3}$	$\frac{4r^3}{3}$	$\frac{4r^3}{3}$
Square side=*l*	$\frac{2l^3}{3\pi^{\frac{3}{2}}}$	$\frac{4l^3}{3\pi^{\frac{3}{2}}}$	$\frac{4l^3}{3\pi^{\frac{3}{2}}}$
Rectangle length=*l* width=*w* Area *A*=*lw*	$\frac{A^{\frac{3}{2}}}{3\sqrt{\pi}E(e)}\cdot\frac{w}{l}$	$\frac{A^{\frac{3}{2}}e^2}{3\sqrt{\pi}[K(e)-E(e)]}\cdot\left(\frac{l}{w}\right)^{\frac{3}{2}}$	$\frac{A^{\frac{3}{2}}}{3\sqrt{\pi}}\cdot\frac{e^2\left(\frac{l}{w}\right)^{\frac{3}{2}}}{\left(\frac{l}{w}\right)^2[E(e)-K(e)]}$

The equiprobability of polarisations is taken into account through the factor ¼. The factor ½ represents the fact that the random plane wave spectrum is only integrated on a half solid angle. Substitute formulas (4.25) and (4.26) into (4.27) yield:

$$\sigma_t = \frac{2k^4}{9\pi}\left(\alpha_e^2 + \alpha_{mx}^2 + \alpha_{my}^2\right) \tag{4.28}$$

These quantities fully characterized the aperture as a function of its geometrical dimensions. Analytical formula are given in Table 4.1 for circular, rectangular and square apertures [39] [42]. Note that the rectangular aperture is approximated by an elliptical one with a semi-major axis of *l* and a semi-minor axis of *w*. The *K*(*e*) and *E*(*e*) are the complete elliptical integrals of the first and second kind respectively and they are expressed as:

$$K(e) = \int_0^{\pi/2}(1 - e^2 sin^2\theta)^{-\frac{1}{2}}\, d\theta \tag{4.29}$$

$$E(e) = \int_0^{\pi/2}(1 - e^2 sin^2\theta)^{\frac{1}{2}}\, d\theta \tag{4.30}$$

The *e* is the ellipse eccentricity and it is given by:

$$e = \sqrt{1 - \left(\frac{w}{l}\right)^2} \tag{4.31}$$

If the aperture is electrically large, the transmission cross section is obtained by formula (4.23). However, when calculating the averaged transmission cross section, Junqua et al introduced a factor ½ to formula (4.24):

$$\sigma_t = \frac{1}{2} \cdot \frac{A}{2\pi} \int_0^{2\pi} d\varphi \int_0^{\pi/2} sin\theta cos\theta d\theta = \frac{A}{4} \quad (4.32)$$

This is because they considered the fact that the aperture is illuminated only from one half space.

The cut-off frequency that marks the transition of an aperture from electrically small to electrically large is given by:

$$f_c = \frac{c}{2\pi} \sqrt[4]{\frac{9\pi A}{8(\alpha_e^2 + \alpha_{mx}^2 + \alpha_{my}^2)}} \quad (4.33)$$

4.4. Calculation of absorption cross section

The example in section 4.2 shows that when using the power balance method, objects can be represented by their absorption cross sections. An absorption cross section measurement is usually performed in a reverberation chamber and it contains two steps: 1. Measure S-parameters between the transmitting and receiving antenna when the object under test is in the chamber; 2. Measure S-parameters between the two antennas when the object is not in the chamber. The measurement configuration can be seen in figure 3.8. The absorption cross section of an object is calculated from the S-parameters by using either frequency or time domain method. The result shown in Figure 4.8 was obtained by using the frequency domain method.

4.4.1. Frequency domain method for calculating absorption cross section

By using the frequency method, the absorption cross section of an object is obtained from [14]:

$$\sigma_a = \frac{\lambda^2}{8\pi} \eta_t \eta_r \left(\frac{1}{G_{wo}} - \frac{1}{G_{no}} \right) \quad (4.34)$$

where η_t and η_r are the efficiency of the transmitting antenna and receiving antenna. G_{wo} and G_{no} are the mean net transfer function with and without the object in the chamber respectively. Mean net transfer function is defined as the ratio of received power and transmitted power. In real measurements, it is calculated from the *S*-parameters between the transmitting antenna and receiving antenna:

$$G = \frac{\langle |S_{21}|^2 \rangle}{(1 - |\langle S_{11} \rangle|^2)(1 - |\langle S_{22} \rangle|^2)} \quad (4.35)$$

where S_{11} and S_{22} are the reflection coefficients of the two antennas respectively.

The measurement uncertainty of the frequency domain method is:

$$\alpha_u = \frac{\mathrm{std}(\sigma_a)}{\sigma_a} \tag{4.36}$$

where std stands for standard deviation.

4.4.2. Time domain method for calculating absorption cross section

Alternatively, absorption cross section can be measured by using time domain method. The time constant, τ, of a reverberation chamber is the time it take for the stored energy to reduce to 1/e of the initial value [43]. The absorption cross section of an object can be obtained by [3]:

$$\sigma_a = \frac{2\pi V}{\lambda}\left(\frac{1}{Q_{wo}} - \frac{1}{Q_{no}}\right) \tag{4.37}$$

where Q_{wo} and Q_{no} are the quality factor of the chamber with and without the object. Quality factor and chamber time constant are related by [3]:

$$Q = \omega\tau \tag{4.38}$$

where ω is the angular frequency. Substitute formula (4.38) to (4.37) and consider the following relationships:

$$\omega = \frac{2\pi}{f} \tag{4.39}$$

and

$$\lambda = \frac{c}{f} \tag{4.40}$$

we obtain:

$$\sigma_a = \frac{V}{c}\left(\frac{1}{\tau_{wo}} - \frac{1}{\tau_{no}}\right) \tag{4.41}$$

where τ_{wo} and τ_{no} are the chamber time constant with and without object. Compared with the frequency domain method, the time domain method does not require the knowledge of antenna efficiency because the time constant is only a function of reverberation chamber [44].

The chamber time constant can be extracted from the power delay profile (PDP), which gives the intensity of a power received through a multipath channel as a function of time delay, of the chamber. The PDP is obtained by applying the invers fast Fourier transform (IFFT) technique to the S_{21} parameter (the transmission coefficient between two antennas in a reverberation chamber, measured in the frequency domain) with a band limited window [45]:

$$\mathrm{PDP} = \langle |\mathrm{IFFT}(S_{21} \cdot \mathrm{Win})|^2 \rangle \tag{4.42}$$

where Win is the window function. Since time constant varies with frequency, it is necessary to use a window function to select a particular frequency band from a broadband S_{21} measurement. The use of window function has the advantage of reducing the amount of data.

The chamber time constant is extracted from the slope of the PDP. In reality, measured PDP is not perfectly straight. Therefore, we need to apply either linear or non-linear curve fitting technique to PDP to obtain a straight line. By using the linear curve fitting technique, the time constant is the slope of the fitted PDP [46]:

$$\mathrm{PDP_{dB}}(t) = 10\log_{10}\left(C_0 e^{-\frac{t}{\tau}}\right) = \left(-\frac{10log_{10}e}{\tau}\right)t + 10\log_{10}C_0 \tag{4.43}$$

where e is the natural algorithm, C_0 is a constant which gives the power of signal. Both τ and C_0 are determining by applying the linear curve fitting technique to PDP on a decibel scale. The result is affected by the shape of window and the selection of range for the fit.

PDP is related to the channel impulse response (CIR) in the chamber, which is the reaction of a channel to a brief input signal as a function of time. By using the non-linear curve fitting technique, it is assumed that the CIR can be modelled as a sum of rays with random phase shifts and exponentially decaying magnitudes [46] [47]:

$$\mathrm{CIR}(t) = \sum_{i=0}^{\infty} \beta_i e^{j\theta_i} \delta(t - T_i) \tag{4.44}$$

where β_i is the magnitude of ray, $e^{j\theta_i}$ is the phase shift of ray, $\delta(\cdot)$ is the Dirac function and T_i is the propagation delay. According to the central limit theory, the CIR at any time in a reverberation chamber complies with complex Gaussian distribution [45]:

$$\mathrm{CIR}_r(t) = V_r e^{-\frac{t}{2\tau}} N_1(t) \tag{4.45}$$

where V_r is the voltage of received signal and $N_1(t)$ is the standard complex Gaussian random process with zero mean and variance of one.

Adding a window function Win(t) and the effect of noise floor to formula (4.45) gives the filtered CIR:

$$\mathrm{CIR}(t) \otimes \mathrm{Win}(t) = \left[V_r e^{-\frac{t}{2\tau}} N_1(t) + V_n N_2(t)\right] \otimes \mathrm{Win}(t) \tag{4.46}$$

where V_n is the noise level of background, $N_2(t)$ is another standard complex Gaussian random process that is independent of $N_1(t)$ and the symbol $\otimes$ stands for circular convolution. The circular convolution of two functions occurs when one of them is convolved in a normal way with a periodic summation of the other function.

In formula (4.46),

$$\mathrm{CIR}_n(t) = V_n N_2(t) \tag{4.47}$$

is the CIR of the noise.

Formulas (4.45) and (4.47) can be written in discrete form that lead to:

$$\mathrm{CIR}_r(m) = V_r e^{-\frac{-m\Delta t}{2\tau}} N_1(m) \tag{4.48}$$

$$\mathrm{CIR}_n(m) = V_n N_2(m) \tag{4.49}$$

where m is the response index in time domain and Δt is time step.

In a discrete Fourier transform, a signal filtered by a window function in frequency domain equals the circular convolution of their CIR in time domain. Therefore, when filtered by a window function Win(m) , a CIR can be written as:

$$\mathrm{CIR}(m) \otimes \mathrm{Win}(m) = \mathrm{CIR}_r(m) \otimes \mathrm{Win}(m) + \mathrm{CIR}_n(m) \otimes \mathrm{Win}(m) \tag{4.50}$$

where

$$\mathrm{CIR}(m) = \mathrm{CIR}_r(m) + \mathrm{CIR}_n(m) \tag{4.51}$$

In physical measurements, the power response of $\mathrm{CIR}(m) \otimes \mathrm{Win}(m)$ is:

$$|\mathrm{CIR}(m) \otimes \mathrm{Win}(m)|^2 = |\mathrm{CIR}_r(m) \otimes \mathrm{Win}(m)|^2 + |\mathrm{CIR}_n(m) \otimes \mathrm{Win}(m)|^2 + \overline{[CIR_r(m) \otimes \mathrm{Win}(m)]}[\mathrm{CIR}_n(m) \otimes \mathrm{Win}(m)] + [\mathrm{CIR}_r(m) \otimes \mathrm{Win}(m)]\overline{[\mathrm{CIR}_n(m) \otimes \mathrm{Win}(m)]} \quad (4.52)$$

where $\bar{a}$ is the complex conjugate of a. Since $N_1(m)$ and $N_2(m)$ are independent of each other, the two rightmost terms in formula (4.52) are eliminated. Therefore, the expectation of $|\mathrm{CIR}(m) \otimes \mathrm{Win}(m)|^2$ is:

$$E[|\mathrm{CIR}(m) \otimes \mathrm{Win}(m)|^2] = E[|\mathrm{CIR}_r(m) \otimes \mathrm{Win}(m)|^2] + E[|\mathrm{CIR}_n(m) \otimes \mathrm{Win}(m)|^2] \quad (4.53)$$

In a Gaussian random process, the random variables of two different moments are independent. Therefore, formula (4.53) can be simplified as (written in time domain) [48]:

$$E[\mathrm{PDP}(t_i)] = E(|h(t_i) \otimes \mathrm{Win}(t_i)|^2) = \left(V_r^2 e^{-\frac{t_i}{\tau}} + V_n^2\right) \otimes |\mathrm{Win}(t_i)|^2 \quad (4.54)$$

where $E(\cdot)$ is the expectation and t_i is the i th sample of time. Formula (4.54) is the full form the non-linear curve fitting model.

The initial value of time constant τ_0 is estimated by linear regression. Then a reference PDP signal $e^{-\frac{t_i}{\tau_0}} \otimes |\mathrm{Win}(t_i)|^2$ is generated to determine the start value of V_r, denoted as $V_{r;0}$ [45]:

$$\frac{\mathrm{PDP}_m(t_i)}{e^{-\frac{t_i}{\tau_0}} \otimes |\mathrm{Win}(t_i)|^2} \approx \frac{\left(V_r^2 e^{-\frac{t_i}{\tau}} + V_n^2\right) \otimes |\mathrm{Win}(t_i)|^2}{e^{-\frac{t_i}{\tau_0}} \otimes |\mathrm{Win}(t_i)|^2} = V_{r;0}^2 \quad (4.55)$$

where PDP_m is the measured power delay profile response. Zhang et al state that the assumption $\mathrm{PDP}_m(t_i) \approx E[\mathrm{PDP}(t_i)]$ holds if PDP_m is of good quality. After the estimation of τ_0 and $V_{r;0}$, the initial value of noise $V_{n;0}$ can be obtained by using a reference signal $I(t_i) \otimes \mathrm{Win}(t_i)$:

$$\frac{\mathrm{PDP}_m(t_i) - V_{r;0}^2 e^{-\frac{t_i}{\tau_0}} \otimes |\mathrm{Win}(t_i)|}{I(t_i) \otimes \mathrm{Win}(t_i)} \approx \frac{V_n^2 \otimes \mathrm{Win}(t_i)}{I(t_i) \otimes \mathrm{Win}(t_i)} = V_{n;0}^2 \quad (4.56)$$

where $I(t_i)$ is a constant function whose value is one.

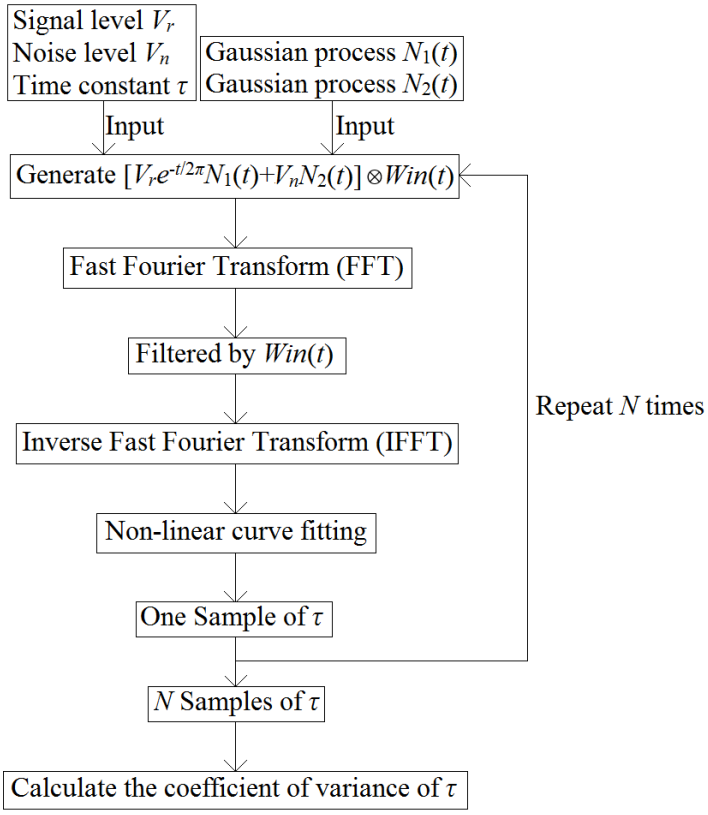

Figure 4. 12. Diagram of Monte Carlo method for estimating measurement uncertainty in time domain [46].

Since the non-linear curve fitting technique involves complex algorithms such as convolution and Fourier transform, it is difficult to derive analytical formula for measurement uncertainty. Zhang et al point out that the uncertainty of the non-linear curve fitting technique can be estimated by Monte Carlo method [48]. Figure 4.12 shows the diagram of the procedure. The Gaussian processes $N_1(t)$ and $N_2(t)$ are generated by built-in function of the Matlab software[49]. Each generated CIR represents a single measurement of CIR at one stirrer position in the reverberation chamber. The N is number of stirrer positions. One value of time constant τ is obtained by applying the non-linear curve fitting technique to the PDP that is calculated from averaging the power of N CIRs. Such process is repeated N times to get N samples of τ, then the distribution of them can be calculated to get the uncertainty.

In [46], Zhang et al state that the non-linear curve fitting technique is better than the linear one because the PDP obtained by using the former method is free from the influence of window function. In addition, the non-linear curve fitting technique allows a narrower window to be applied, which leads to fewer samples and less measurement time.

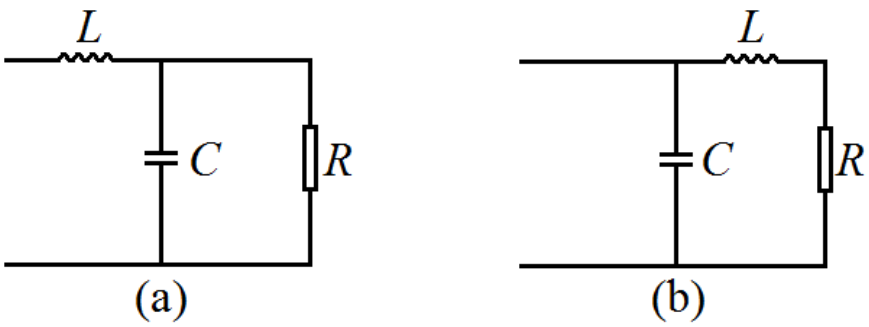

Figure 4. 13. Equivalent circuit models of a resistor at high frequency. (a) a resistor with high resistance; (b) a resistor with low resistance.

4.5. Effect of power state on absorption cross section

The example in section 4.2 shows that using the absorption cross section of an object is a helpful method for estimating the shielding effectiveness of a populated enclosure. In [4], Flintoft et al measured the absorption cross sections of stacked printed circuit boards and the boards were measured when they were not powered [4]. To the best of our knowledge, we have not found any paper that talk about the effect of power state on the absorption cross section of electronic components. We expected that the power state (power on or power off) might affect the absorption cross sections of electronic components since the active devices in the circuit have different behaviours when powered on or powered off. Taking a printed circuit board as an example. A printed circuit board has a variety of components. Based on the characteristics of port voltage/current, they can be classified as wires, resistors, capacitances, inductances and transformers [6]. We are interested in active devices because their behaviour is different in different power states.

Any wire, as long as it is not completely shielded, behaves like an antenna. Therefore, a unshielded wire might change the field in the vicinity and affect ACS measurement.

At low frequencies, resistors on a printed circuit board do not affect the surrounding field. In a radio frequency (RF) system, at high frequency, a resistor might be equivalent as a series parallel circuit that consists of a resistor, a capacitance and an inductance as shown in figure 4.13. At certain frequency, series resonances might occur and cause EMI problems.

In real cases, a capacitance has parasitic inductance and parasitic resistance. At high frequency, it can be modelled as a series circuit that consists of a resistor, a capacitance and

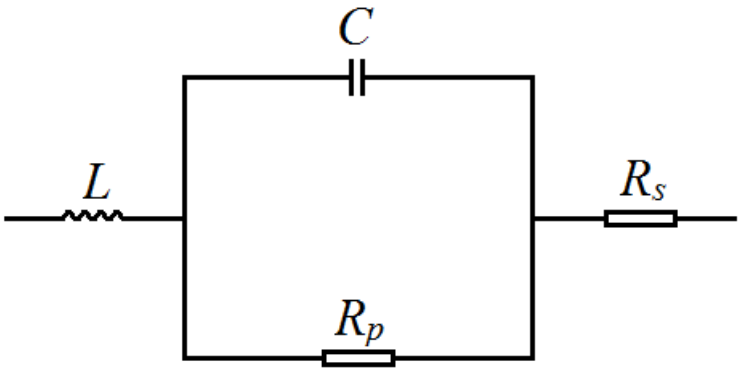

Figure 4. 14. Equivalent circuit model of a capacitance at high frequency.

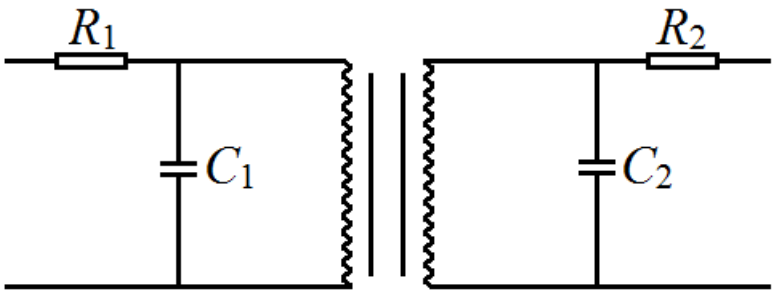

Figure 4. 15. Equivalent circuit of a transformer.

an inductance as shown in figure 4.14, where R_p and R_s are the parallel and series resistors respectively. The parasitic resistors cause attenuation to the signal that goes through the capacitance. The parasitic inductance and the capacitance form a series resonant circuit. Therefore, there are self-resonance at certain frequency.

At high frequency, an inductance can be equivalent as a parallel circuit that consists of a resistor and a capacitance. Therefore, it has the damping effect and is able to absorb some high frequency energy. In real circuits, especially digital circuits, inductance is used to suppress EMI.

A transformer on a printed circuit board can be modelled as a circuit that consists of a resistor, a capacitance and a coil as shown in figure 4.15, where R_1 and R_2 are the coil impedances; C_1 and C_2 are the distributed capacitances. Here we ignore the core loss, the capacitance between the core and the leakage inductance. When two circuits on a printed circuit board are very close, there is mutual electromagnetic induction and this mechanism is equivalent to that of a transformer.

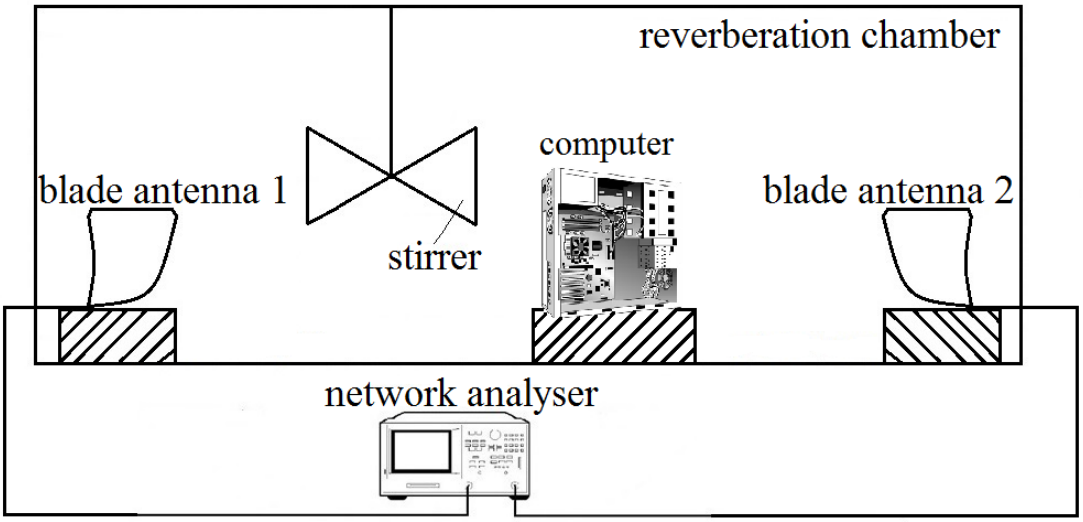

Figure 4. 16. Diagram of the absorption *cross section measurement configuration of the computer in the reverberation chamber at the University of York.*

According to the introduction above, it can be seen that a printed circuit board contains components with different natures, among them there are active devices. When the board is powered on or powered off, these active devices have different behaviours. In addition, if the board is powered on, their behaviours change with frequency. Previously, Flintoft et al have proved that the re-emission spectrum of digital hardware under the influence of EMI contains information about the interaction of the incident energy with digital circuits in a system [50]. We expected a change on power state might result in a change in the power absorbed by the components and thus affect the absorption cross section.

To test this assumption, we measured the absorption cross section of the computer components shown in figure 4.1 in both powered and unpowered states to compare the difference. Inside the enclosure, there are a printed circuit board, a power supply unit, a CD-ROM, a hard drive and several wires. The measurements were performed in the reverberation chamber at the University of York. Figure 4.16 shows the diagram of the measurement configuration. Two blade antennas were used as transmitting and receiving antenna [35]. A network analyser collected *S*-parameters from the two antennas. Figure 4.17 shows the photograph of the measurement set up. The blade antennas were at two corners in the chamber. The monitor, mouse and keyboard of the computer were removed during the measurements. We also took off the side panel of the computer to expose the circuity to the electromagnetic energy in the chamber thus enabling the overall absorption cross section to

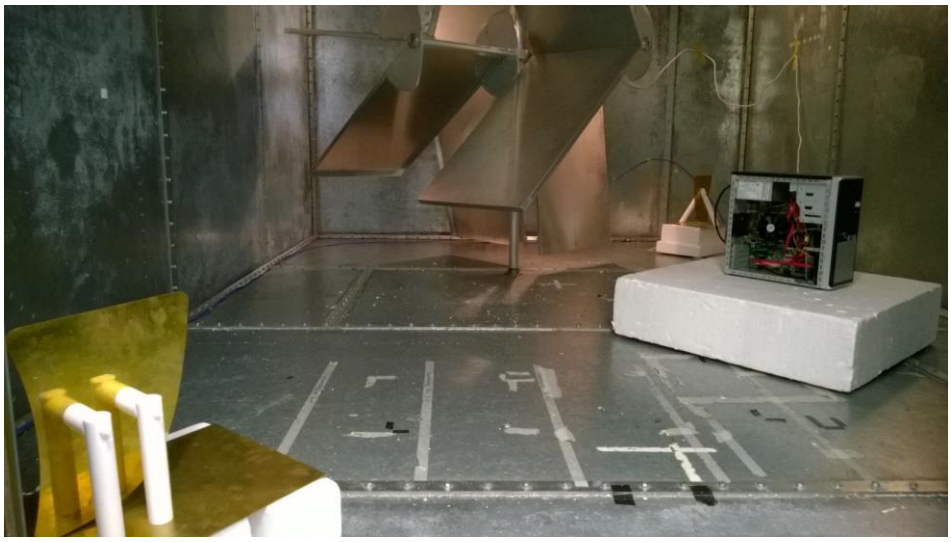

Figure 4. 17. Photograph of the absorption cross section measurement configuration of the computer in the reverberation chamber at the University of York, showing the two blade antennas and the computer without side panel.

be measured. The absorption cross section of the powered and unpowered computer was measured three times each for comparison.

When the computer was powered, we turned it on during the measurements so Windows 7 system was activated. To make the computer operate at full capacity, we used a stress test software HeavyLoad to test the central processing unit (CPU), graphics processing unit (GPU) and hard drive at the same time [51]. In addition, we activated windows media player to play a CD so that the CD-ROM was also in full use. During the measurements, the computer remained at the same place and the only thing that changed was its power state.

The absorption cross section of the powered and unpowered computer was measured from 1GHz to 18GHz by using both frequency and time domain method. For the former method, we used stepped stirring technique. The mechanical stirrer in the reverberation chamber was set to move 100 equally spaced positions over a full rotation. The network analyser recorded 10001 uniformly spaced points over the measurement frequency range. We also applied frequency stirring technique with a bandwidth of 50MHz to further reduce measurement error. The net transfer function with and without the computer was calculated from *S*-parameters by using formula (4.35) and then we used formula (4.34) to obtain the absorption cross section. We assumed the efficiency of the blade antennas is one.

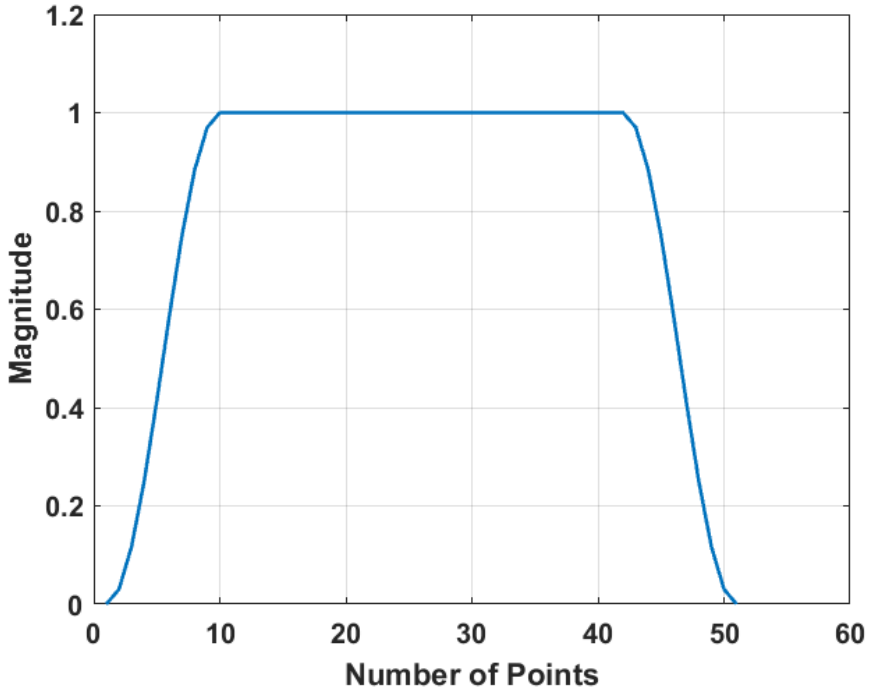

Figure 4. 18. Shape of a raised cosine window that is used to obtain segmented S_{21} parameter for the calculation of absorption cross section using the time domain method.

As for the time domain method, due to the robustness of the non-linear curve fitting technique, the shape and size of the window function in formula (4.42) can be chosen randomly. Here we follow Zhang et al in using a raised cosine window function to obtain segmented frequency information [48]. Figure 4.18 shows its shape. One windows contains 51 points. The rising part on the left and the falling part on the right contain 11 points each and are given by:

$$\begin{aligned} Win_{rise} &= 0.5 - 0.5cos\left(\frac{\pi}{10}i\right) \\ Win_{fall} &= 0.5 + 0.5cos\left(\frac{\pi}{10}i\right) \end{aligned} \quad i = 0,1,2 \dots \dots 10 \tag{4.57}$$

The magnitude of the flat part in the middle is one and it contains 39 points.

Figure 4.19 shows the diagram of the frequency segments. There are totally 171 segments evenly distributed throughout the measurement range with a distance of 100MHz. Each segment has a bandwidth of 5MHz and contains 51 points.

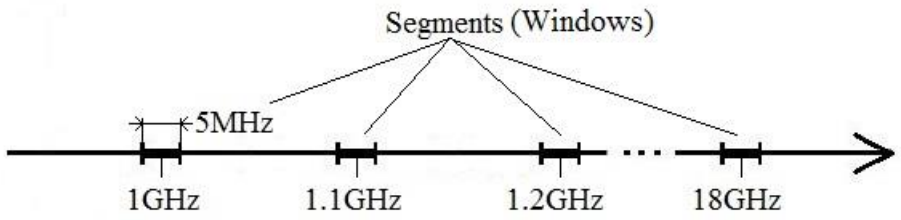

Figure 4. 19. Diagram of the frequency segments for the calculation of absorption cross section by using the time domain method.

Table 4. 2. Number of independent samples in the reverberation chamber at the University of York when using the continuous stirring technique. Taken from [45].

	Speed=0.5625 deg/s	Speed=1.25 deg/s
Number of independent sample at 1GHz	247	185
Number of independent sample at 7GHz	370	185
Number of independent sample at 13GHz	370	185
Number of independent sample at 18GHz	370	185
Total number of samples	740	370
Measurement time (s)	630	312

To reduce measurement time, we follow Zhang et al is using the continuous stirring technique [45] [52]. In the process of measurement, the network analyser collected data while the stirrer was constantly moving. As has been discussed in Section 3.1.3, it requires sufficient independent samples to build a uniform electromagnetic environment in a reverberation chamber. Zhang et al tested two stirrer speeds to find out the number of independent samples that can be generated over a full rotation. The measurement delay of the network analyser was set as 65μs to leave sufficient time for data sweep. As an example, Zhang et al showed the autocorrelation of S_{21} parameter of the empty chamber at 1GHz in figure 4.20. It can be seen that when the stirrer moves at 0.5625 deg/s, there are three correlated samples; when the speed is 1.25 deg/s, there are two correlated samples. The number of independent samples were calculated by using formula (3.6) and Zhang et al plotted the results in table 4.3. Clearly, a speed of 0.5625 deg/s leads to more independent samples. Therefore, in our measurements, we used this speed that resulted in 800 stirrer positions over one complete rotation. Zhang et al suggest that the stirrer speed can be altered to make a trade-off between measurement time and number of independent samples.

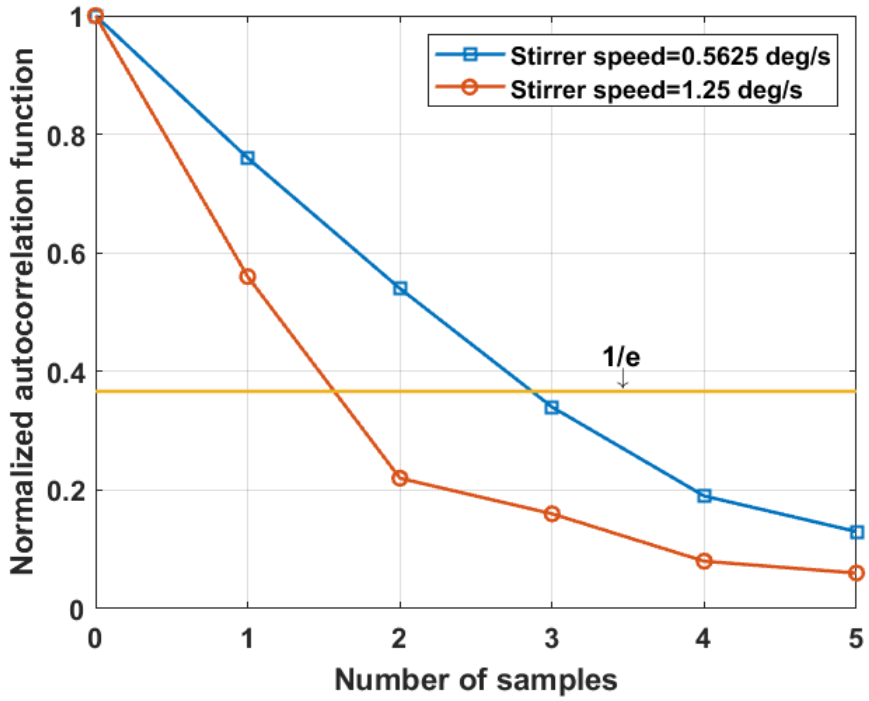

Figure 4. 20. Normalized autocorrelation of S_{21} at 1GHz for continuous stirring in the empty reverberation chamber at the University of York. Taken from [45].

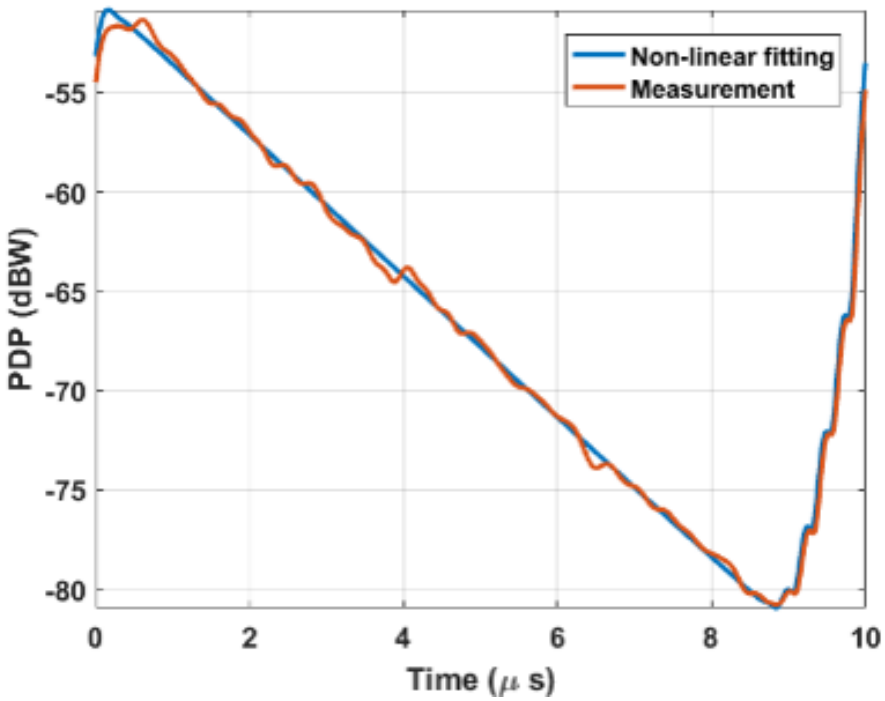

Figure 4. 21. Power delay profile(PDP) in the reverberation chamber at the University of York at 1GHz with the presence of the unpowered computer.

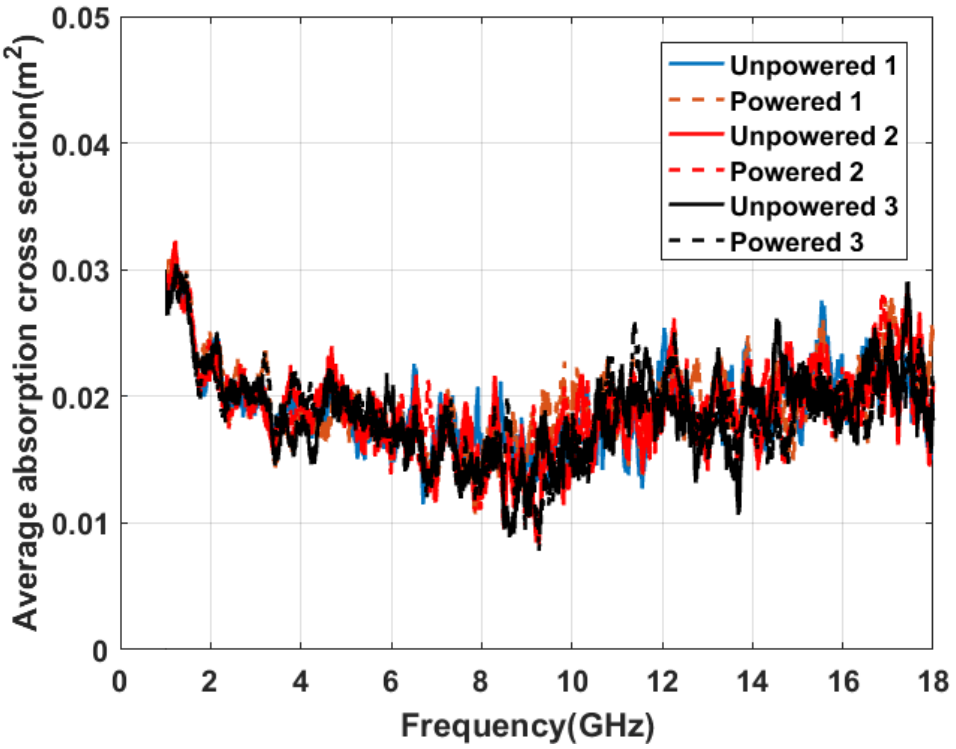

Figure 4. 22. Measured absorption cross section of the computer in different power states by using the frequency domain method.

The power delay profile (PDP) of the chamber was calculated by using formula (4.42). As an example, we show the PDP of the chamber with the unpowered computer at 1GHz at figure 4.21. It can be seen that the power in the chamber decreases gradually with time. However, there is a sudden rise after 9μs. This is an artefact of the inverse fast Fourier transform technique. The PDP of a chamber is periodic and the rise in the end of one period is the start of another.

With the power delay profile obtained, the time constant of the chamber can be obtained by using the non-linear curve fitting model and the absorption cross section of the computer can be calculated by formula (4.41).

Figures 4.22 and 4.23 show the measured absorption cross section of the powered and unpowered computer by using frequency and time domain method. It can be seen that the computer has an absorption cross section of about 0.02m^2. The frequency domain method produces much more variable results than the time domain method. Based on formula (4.36) and figure 4.12, the measurement uncertainty of the frequency and time domain method are

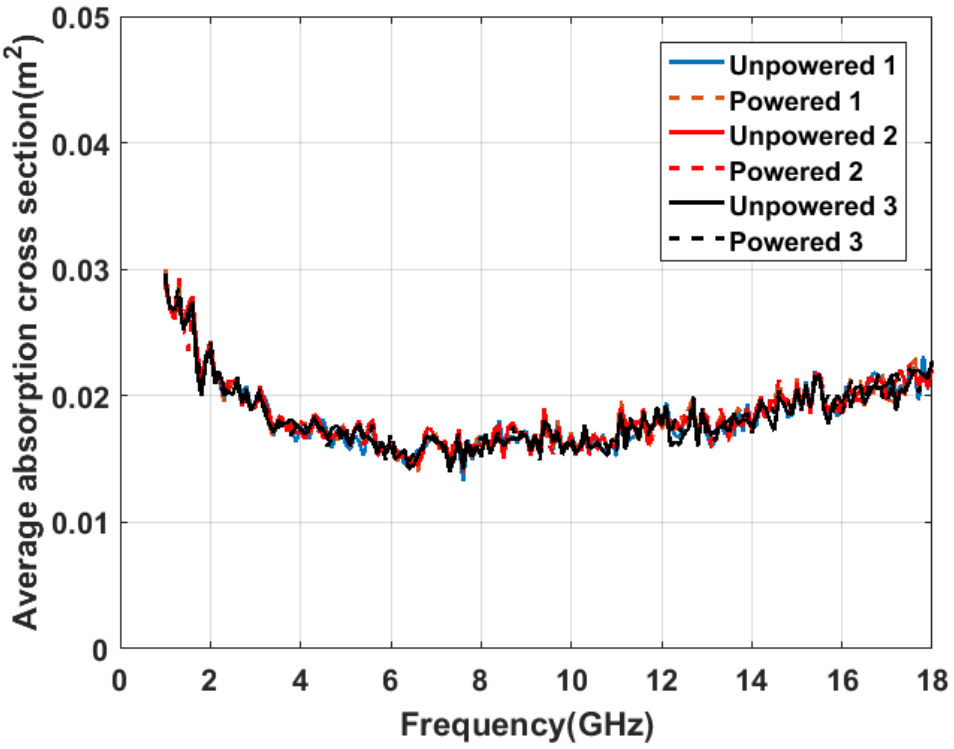

Figure 4. 23. Measured absorption cross section of the computer in different power states by using the time domain method.

calculated to be 20% and 1% respectively. For the frequency domain method, one way to reduce the measurement uncertainty is to increase the number of stirrer positions, but this would also increase the measurement time.

As has been mentioned, we applied stepped stirring technique when using the frequency domain method and it took about 50 minutes for the stirrer to finish one full rotation. When using the continuous stirring technique and the time domain method, the measurements lasted only about 10 minutes for 800 stirrer positions.

Figure 4.24 compares the measured absorption cross section by using the two methods. The results in figure 4.24 are the averages of the six measurements presented in figures 4.22 and 4.23. The comparison suggests that both methods led to similar results and that the absorption cross section of the computer is independent of power state within the 1% measurement variability. Therefore, we can come to the conclusion that the power state has little influence on the absorption cross section and this conclusion can be applied to other electronic equipment. When performing similar measurements in the future, there will be no

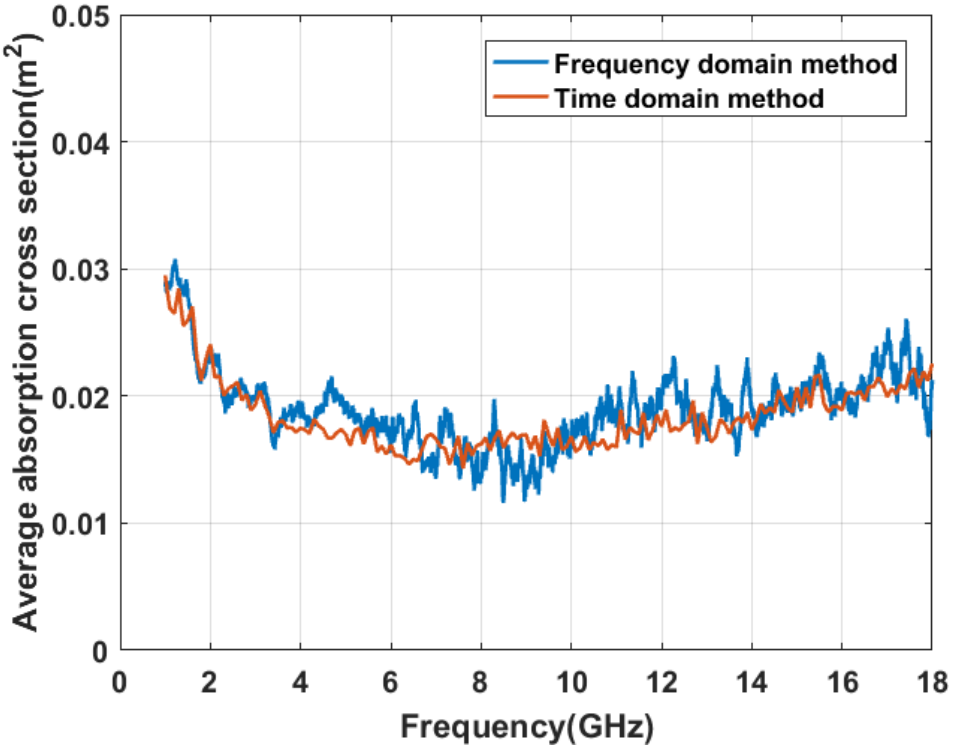

Figure 4. 24. Comparison between the measured absorption cross section of the computer obtained by using the frequency and time domain methods.

need to consider the power state of the equipment under teat, which will bring convenience to the measurements.

4.6. Effect of measurement position on absorption cross section

Most of the measurements presented in this thesis were performed in the reverberation chamber shown in figure 3.3. As has been discussed in section 3.1.3, a reverberation chamber provides a uniform electromagnetic environment. Therefore, when performing measurements such as those shown in figures 4.2, 4.7 and 4.17, we did not give particular consideration to the positions of the antennas and the equipment under test. In reality, the reverberation chamber at the University of York is not ideal. There are bolts and joints on the chamber walls. In addition, there is a nested reverberation chamber with dimensions of 0.6m×0.7m×0.8m as shown in figure 4.25. We suspected that their presence might perturb the field uniformity and thus affect the absorption cross section measurements. Therefore, we measured the absorption cross section of the powered and unpowered computer at two different locations in the reverberation chamber at the University of York.

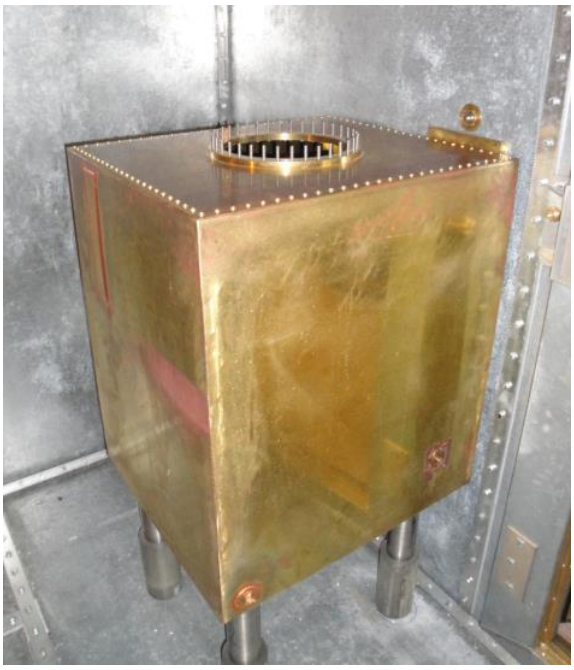

Figure 4. 25. Photograph of the nested reverberation chamber at the University of York.

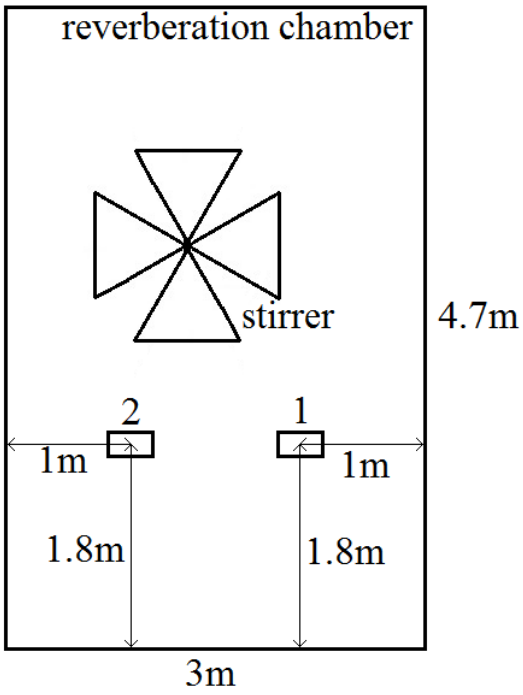

Figure 4. 26. Diagram of the top view of the Absorption cross section measurement configuration of the computer at different positions in the reverberation chamber at the University of York.

Figure 4.26 shows the diagram of the two positions and figures 4.27, 4.28 show the configuration of the measurement. Due to the fact that the time domain method has much

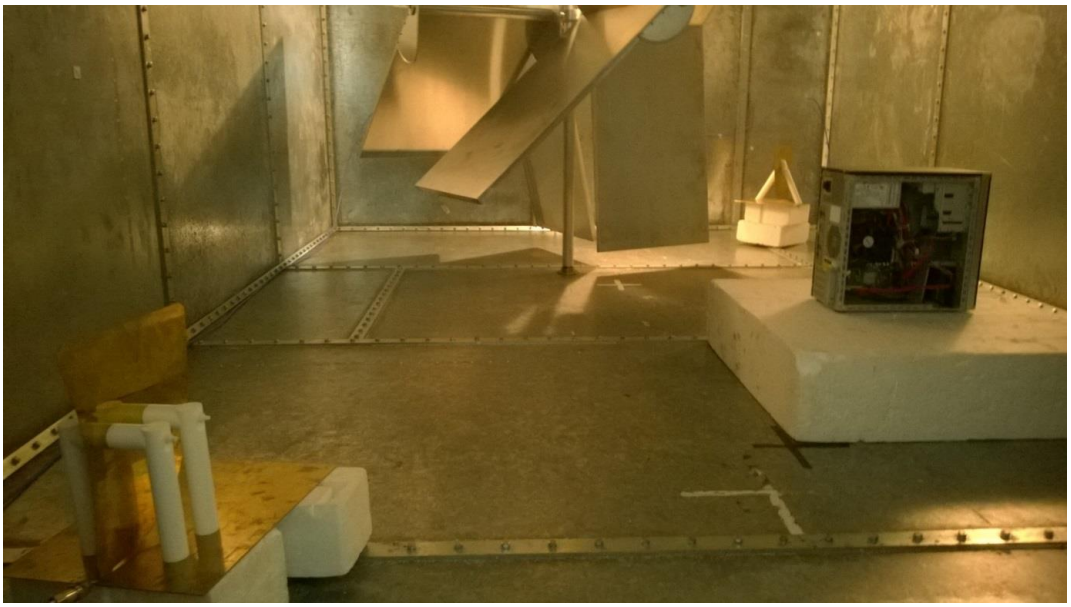

Figure 4. 27. Photograph of the Absorption cross section measurement configuration of the computer at position 1 in the reverberation chamber at the University of York.

Figure 4. 28. Photograph of the Absorption cross section measurement configuration of the computer at position 2 in the reverberation chamber at the University of York.

lower uncertainty than the frequency domain method, for these four measurements we only used the former. Besides the difference in measurement location, the rest of the measurement procedure are the same as those in section 4.5 and they will not be repeated here.

Figure 4.29 shows the measurement results. It can be seen that all four measurements produced similar results. Comparing figures 4.24 and 4.29, it can be concluded that for this

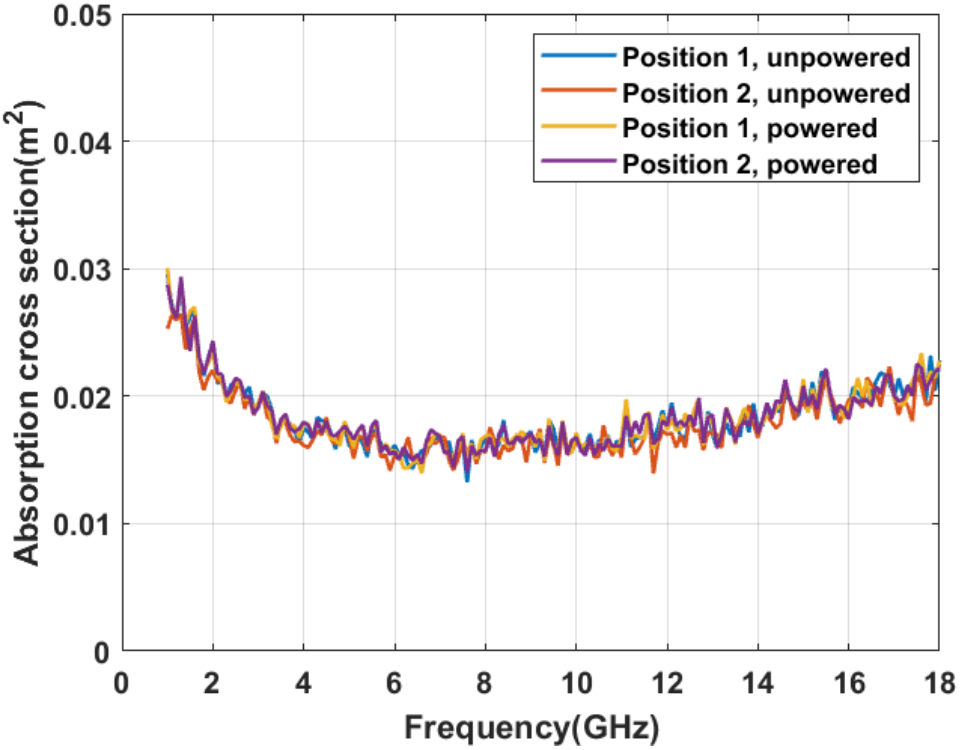

Figure 4. 29. Measured absorption cross section of the powered and unpowered computer at different positions in the reverberation chamber at the University of York. The time domain method was used to obtain the results.

application, the differences in power state and measurement location has little effect on the absorption cross section within the 1% measurement uncertainty.

4.7. Summary

This chapter is about the shielding problems of populated enclosures. To begin with, we present the shielding measurement of a computer enclosure with and without contents. Comparison suggests that the shielding effectiveness of the loaded enclosure is much higher than that of the empty one. Therefore, the contents of an enclosure should not be ignored when analysing shielding problems.

We then introduce the widely used power balance (PWB) method. It divides the dissipated power to several parts according to their loss mechanisms. In this way, one big complex problem is replaced by some smaller and simpler ones. The most distinctive feature of the PWB method is that it does not require the detailed geometry of the contents or the enclosure since it only considers average energy.

By using the power balance method, the apertures are represented by their transmission cross sections (TCS) and the contents by their absorption cross sections (ACS). The transmission cross section of an aperture is calculated by its polarizability tensors. The absorption cross section of an object can be obtained by using either frequency or time domain method. The former obtains ACS from net transfer function and the latter from the time constant of the reverberation chamber. Compared with the frequency domain method, the time domain method has the advantage of independent of antenna efficiency and lower measurement uncertainty.

Since contents have a great influence on shielding effectiveness, it is important to obtain accurate ACS of them when using the power balance method. Previously the absorption cross sections of some printed circuit boards have been measured their power state have been ignored. To the best of our knowledge, we have not found any reference that centres on the influence of power state on ACS. We suspected a change in power state might affect the ACS of electronic components due to the difference in the behaviour of active components. Therefore, we measured the ACS of a computer that contains a printed circuit board in both powered and unpowered states at different locations in a reverberation chamber. The results obtained by using both frequency and time domain method indicate that power state has little effect on the ACS. In the future, when performing similar measurements, there will be no need to consider the power state.

Chapter 5

The diffusion equation based model

5.1. Limitation of the power balance method

The previous chapter introduced the power balance method, which has been used for many years in high frequency shielding problems. The power balance method takes only a few seconds to provide results, which is much faster than full wave solvers, since all we need to do is solve a simple equation (4.21). For a populated enclosure, the power balance method assumes that reflections of energy from the walls and contents lead to a uniform electromagnetic field throughout the enclosure. This assumption only holds when the loss in the enclosure is small. For moderate or high loss, while there are still multiple reflections in the enclosure, the electromagnetic field is no longer uniform and the power balance method cannot describe this non-uniformity [5]. Later in this chapter, we will present examples to demonstrate the failure of the power balance method in high loss case.

This limitation affects some EMC applications. For measurements performed in a reverberation chamber with significant loading, such as measuring the absorption cross sections of printed circuit boards [4] or using loads to represent a multipath environment [53], the absorption of the contents induces inhomogeneity and contributes to systematic error[5]. This error is usually dealt with on a statistical basis, for example, measuring average fields at different locations in a reverberation chamber and characterizing the non-uniformity (proximity effect) from the deviation of the samples [54]. It would be desirable to find a method to account for this field non-uniformity directly.

5.2. The diffusion model

The acoustics community has developed an approach that is able to account for the variation of the diffuse energy density in enclosed spaces due to the presence and distribution of losses on the walls and contents (if there are any) of an enclosure. Recent developments of the acoustical diffusion model are given in [55] [56]. The diffusion method can be derived from the transport theory of rays in an enclosure [57] and can be seen as a natural generalization

of the power balance method. The computational burden of the diffusion model, while higher than that of the power balance method, is still substantially lower than that of full-wave simulation. Later in this chapter, we will give the time required to obtain the power density inside an enclosure by using the diffusion model (took minutes) as well as full wave simulation (took hours).

Sound waves are longitudinal while electromagnetic waves are transverse. This difference in nature makes it impossible to apply the acoustical diffusion model to electromagnetic applications directly. In [5], Flintoft et al put the acoustical formalism into the context of electromagnetics. For the initial evaluation, Flintoft et al made use of a dimensional reduction technique to construct two-dimensional models for some canonical test cases consisting of single and dual cavities loaded with radio absorbing material (RAM). The results compared reasonably well with experimental data.

In this chapter, we follow the work of Flintoft et al and evaluate the usefulness of a three-dimensional diffusion model, which is clearly more applicable than the two-dimensional one. The differences between our research and that of Flintoft et al are: 1. we use an enclosure that contains an aperture, which is more realistic since real equipment enclosures have apertures; 2. we perform the measurements in a reverberation chamber so that the electromagnetic environment around the enclosure is reverberant; 3. we provide full wave simulations as a reference.

5.2.1. Overview of the diffusion model

The diffusion model assumes the existence of the diffuse electromagnetic field in the space under test. The average energy density of the field at position **r** within the space is:

$$w(\mathbf{r}) = \langle \frac{1}{2} [\varepsilon_0 E^2(\mathbf{r}) + \mu_0 H^2(\mathbf{r})] \rangle \tag{5.1}$$

where ε_0 and μ_0 are the vacuum permittivity and permeability, $E(\mathbf{r})$ and $H(\mathbf{r})$ are the total electric and magnetic fields. Here the term total field means the root of the sum of the squares of the field components. In terms of Cartesian coordinate system, the components of electric and magnetic fields are E_x, E_y, E_z and H_x, H_y, H_z respectively. The symbol <·> denotes an average of a statistical ensemble of fields due to, for instance, mechanical stirring in a

reverberation chamber. The scalar power density $S(\mathbf{r})$ and the energy density $w(\mathbf{r})$ are related by:

$$S(\mathbf{r}) = cw(\mathbf{r}) \tag{5.2}$$

where c is the velocity of light.

The basic assumptions of the electromagnetic diffusion model are: 1. the propagation of electromagnetic waves complies with Geometric optics, which means the wavelength is small compared to the size of the space under test and the contents (if there are any) in it; 2. the propagation directions of the waves are randomized by the statistical ensemble of fields due to, for example, mechanical stirring in a reverberation chamber; 3. within the space reflection dominates absorption, so after sufficient reflections the field tends to be uniform.

Consider the assumptions stated above, the diffuse electromagnetic energy within an enclosed space with a volume of V satisfies a diffusion equation [58]:

$$(D\nabla^2 + \Lambda)w(\mathbf{r}) = P\delta^{(3)}(\mathbf{r} - \mathbf{r}_s) \quad \mathbf{r} \in V \tag{5.3}$$

where D is the diffusion coefficient (diffusivity) that measures the degree of scattering produced on reflection, Λ is the volumetric loss rate due to content (if there are any) absorption in the space, P is the total radiated power and here we assume there is an isotropic point source, δ is the Dirac function and $\mathbf{r}_s$ is the location of the source.

The diffusion coefficient (diffusivity) accounts for the scattering from the walls and contents (if there are any) within the space. It is related to the mean free path, l_{MFP}, which is the average distance travelled by a wave between successive impacts [59]:

$$D = \frac{cl_{MFP}}{3} \tag{5.4}$$

For an empty enclosure without a high aspect ratio, the mean free path for scattering from the walls is given by [60]:

$$l_{MFP;wall} = \frac{4V}{A_{wall}} \tag{5.5}$$

where A_{wall} is the surface area of the walls and V is the space volume.

If there are contents in the enclosure, the mean free path for scattering due to the contents alone can be estimated as [61]:

$$l_{MFP;con} = \frac{4V}{A_{con}} \tag{5.6}$$

Where A_{con} is the surface area of the contents.

Therefore, for a populated enclosure, the mean free path is calculated by [61]:

$$\frac{1}{l_{MFP}} = \frac{1}{l_{MFP;wall}} + \frac{1}{l_{MFP;con}} \tag{5.7}$$

where $l_{MFP;wall}$ and $l_{MFP;con}$ are the contributions to mean free path due to the walls and presence of contents. It is obvious the shortest mean free path has the biggest influence on the diffusion coefficient.

If the contents are dissipative and penetrable, then we need to consider the volumetric loss rate due to content absorption in formula (5.3), which is given by [62]:

$$\Lambda = \frac{c\alpha_{con}}{l_{MFP;con}} \tag{5.8}$$

where α_{con} is the absorption efficiency of the contents.

Absorption in the boundary area (enclosure walls) is assumed to satisfy a Robin boundary condition [5]:

$$[D\hat{\mathbf{n}} \cdot \nabla + c\sum_{\alpha}(\mathbf{r})]w(\mathbf{r}) = 0 \quad \mathbf{r} \in \partial V \tag{5.9}$$

where $\hat{\mathbf{n}}$ is the outward unit normal vector, $\sum_{\alpha}(\mathbf{r})$ is the absorption factor of the enclosure walls. According to Fick's first law, energy density and energy density flux are related by [63]:

$$J(\mathbf{r}) = -D\nabla w(\mathbf{r}) \tag{5.10}$$

which states that the energy density flux is proportional to the gradient of the energy density. In any dissipative enclosure, there must be a non-zero energy density flux in order to transport the energy from the source to the surrounding space and absorptive objects.

Various models have used in acoustic literature to estimate the absorption factor of walls and the simplest one is Sabine's formula [64]:

$$\sum_{\alpha}(\mathbf{r}) = \frac{\alpha_{wall}(\mathbf{r})}{4} \tag{5.11}$$

where α_{wall} is the absorption efficiency of the enclosure walls. The method for calculating absorption efficiency will be presented in the next section. Flintoft et al point out that formula

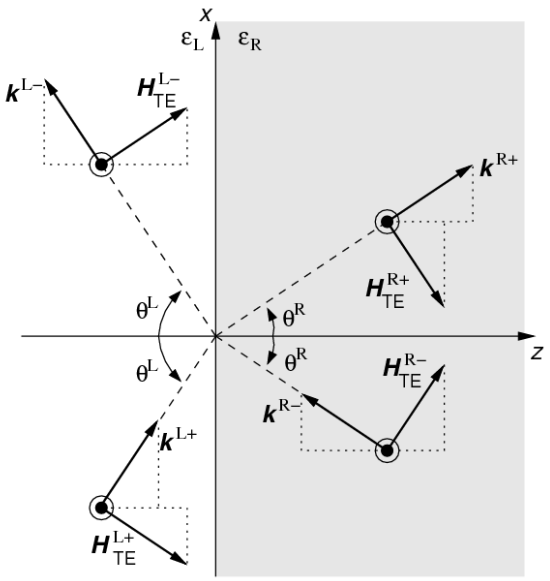

Figure 5. 1. Diagram of interfacial transmission of TE waves at Z-normal plane.

(5.11) is accurate only when $0<\alpha_{wall}<0.2$. A modified form based on the Eyring reverberation time has also been applied [65]:

$$\sum_{\alpha}(\mathbf{r}) = \frac{\log_{10}[1-\alpha_{wall}(\mathbf{r})]}{4} \tag{5.12}$$

Flintoft et al state that formula (5.12) empirically provides better results for moderate absorption $0<\alpha_{wall}<0.5$, but it becomes singular when $\alpha_{wall}=1$. More recently, a relation based on a radiative transport model has been proposed which appears to be suitable for the full range of absorption efficiency [66]:

$$\sum_{\alpha}(\mathbf{r}) = \frac{\alpha_{wall}(\mathbf{r})}{2[2-\alpha_{wall}(\mathbf{r})]} \tag{5.13}$$

5.2.2. Calculation of the absorption efficiency of enclosure walls

For the electromagnetic diffusion model, the absorption efficiency of enclosure walls, α_{wall}, in formulas (5.11), (5.12) and (5.13) can be obtained using the standard estimate of wall losses in a reverberation chamber [67] [41]. The Fresnel reflection coefficient for the reflection of TE and TM plane waves at an infinite large plane between two half space, as shown in figures 5.1 and 5.2, are given by:

$$\Gamma_{\mathrm{TE}}(\theta) = \frac{\mu_{\mathrm{R}} k_{\mathrm{L}} \cos\theta - \mu_{\mathrm{L}} \sqrt{k_{\mathrm{R}}^2 - k_{\mathrm{L}}^2 \sin^2\theta}}{\mu_{\mathrm{R}} k_{\mathrm{L}} \cos\theta + \mu_{\mathrm{L}} \sqrt{k_{\mathrm{R}}^2 - k_{\mathrm{L}}^2 \sin^2\theta}} \tag{5.14}$$

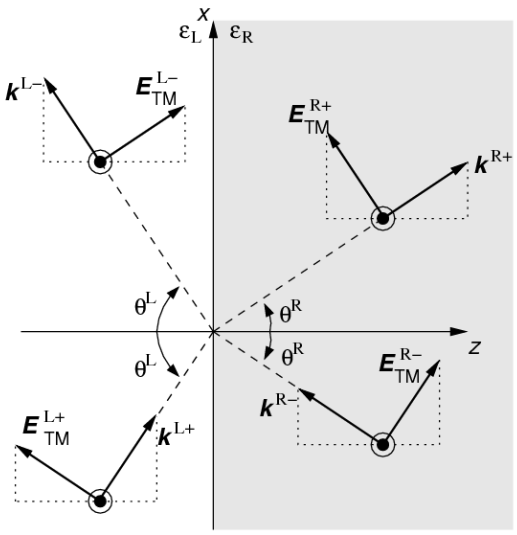

Figure 5. 2. Diagram of interfacial transmission of TM waves at Z-normal plane.

$$\Gamma_{\mathrm{TM}}(\theta) = \frac{\mu_{\mathrm{L}} k_{\mathrm{R}} \cos\theta - \mu_{\mathrm{R}} k_L \sqrt{k_{\mathrm{L}}^2 - k_{\mathrm{R}}^2 \sin^2\theta}}{\mu_{\mathrm{L}} R \cos\theta + \mu_{\mathrm{R}} k_L \sqrt{k_{\mathrm{L}}^2 - k_{\mathrm{R}}^2 \sin^2\theta}} \tag{5.15}$$

where ϑ is the incident angle, μ_{L}, k_{L} and μ_{R}, k_{R} are the permeability and complex wave vector of the media on the left and right side of the infinite plane respectively. The wave vectors are given by:

$$k_{\mathrm{L}} = \omega\sqrt{\mu_{\mathrm{L}}\varepsilon_{\mathrm{L}}} \tag{5.16}$$

$$k_{\mathrm{R}} = \omega\sqrt{\mu_{\mathrm{R}}\left(\varepsilon_{\mathrm{R}} - j\frac{\sigma_{\mathrm{R}}}{\omega}\right)} \tag{5.17}$$

where ω is the angular frequency, ε_{L} and ε_{R} are the permittivity of the media on the left and right side of the plane respectively, σ_{R} is the conductivity on the right side of the plane.

The power absorbed by an area *A* of the surface can be obtained by integrating the Poynting flux into the walls over the surface:

$$P_{a;wall} = \iint_A S\hat{\mathbf{k}} \cdot \mathbf{dS} = AS(1 - |\Gamma|^2)\cos\theta \stackrel{\text{def}}{=} \sigma_a(\theta)S \tag{5.18}$$

In a diffuse field, we assume that the power density arriving at the walls from all directions is <*S*>/4π, shared between the two independent polarisations. However, since the walls are large and non-convex, the power only arrives from a half space. Therefore, we only integrate over 2π steradian. The total power absorbed by the walls in the two polarisations are:

$$P_{a;wall}^{\mathrm{TE}} = A \iint_A [1 - |\Gamma_{\mathrm{TE}}(\theta)|^2] \cdot \frac{1}{2} \cdot \frac{\langle S \rangle}{4\pi} \cdot \cos\theta dV \tag{5.19}$$

$$P_{a;wall}^{\mathrm{TM}} = A \iint_A [1 - |\Gamma_{\mathrm{TM}}(\theta)|^2] \cdot \frac{1}{2} \cdot \frac{\langle S \rangle}{4\pi} \cdot \cos\theta dV \tag{5.20}$$

The total absorbed power is:

$$\begin{aligned} P_{a;wall} &= P_{a;wall}^{\mathrm{TE}} + P_{a;wall}^{\mathrm{TM}} \\ &= \frac{A}{4\pi} \int_0^{2\pi} \int_0^{\pi/2} \left\{ 1 - \frac{1}{2} [|\Gamma_{\mathrm{TE}}(\theta)|^2 + |\Gamma_{\mathrm{TM}}(\theta)|^2] \right\} \cos\theta d\theta d\varphi \cdot \langle S \rangle \end{aligned} \tag{5.21}$$

giving the absorption cross section:

$$\sigma_{a;wall} = \frac{A}{4\pi} \int_0^{2\pi} \int_0^{\pi/2} \left\{ 1 - \frac{1}{2} [|\Gamma_{\mathrm{TE}}(\theta)|^2 + |\Gamma_{\mathrm{TM}}(\theta)|^2] \right\} \cos\theta d\theta d\varphi \tag{5.22}$$

where φ is the polar angle.

Absorption cross section and absorption efficiency are related by:

$$\sigma_{a;wall} = \frac{\alpha_{wall} A}{4} \tag{5.23}$$

Substituting formula (5.22) into (5.23), we obtain the absorption efficiency:

$$\alpha_{wall} = \frac{1}{\pi} \int_0^{2\pi} \int_0^{\pi/2} \left\{ 1 - \frac{1}{2} [|\Gamma_{\mathrm{TE}}(\theta)|^2 + |\Gamma_{\mathrm{TM}}(\theta)|^2] \right\} \cos\theta d\theta d\varphi \tag{5.24}$$

5.2.3. Radiation source

In the electromagnetic diffusion model, either point source or surface source can be used [62]. In formula (5.3), we assume there is a point source. The Green's function for the diffusion equation in a bounded space is given by [63]:

$$G(\mathbf{r}|\mathbf{r}_s) = \frac{P}{4\pi D|\mathbf{r}-\mathbf{r}_s|} \exp\left(-\sqrt{\frac{\Lambda}{D}} |\mathbf{r} - \mathbf{r}_s| \right) \tag{5.25}$$

In [63], Visentin et al state that the energy near such a source contains a spurious term:

$$w_d(\mathbf{r}) = \frac{P}{4\pi D|\mathbf{r}-\mathbf{r}_s|} \tag{5.26}$$

This term arises from the fact that a diffuse field has not been established in the vicinity of the source. Therefore, the energy near the source should be subtracted to give the reverberant energy density:

$$w_r(\mathbf{r}) = w(\mathbf{r}) - w_d(\mathbf{r}) \tag{5.27}$$

The spurious effect can also be got rid of by smearing the source out over a volume of space using a surface source [62].

With the correction in formula (5.27), the corresponding reverberant energy density flux is:

$$J_r(\mathbf{r}) = J(\mathbf{r}) - \frac{P}{4\pi|\mathbf{r}-\mathbf{r}_s|^3}(\mathbf{r} - \mathbf{r}_s) \tag{5.28}$$

If a surface source is used, a source term should be included into the Robin boundary condition. Suppose a portion of the domain boundary with an area A_s is used as a surface source, then the boundary condition is:

$$D\hat{\mathbf{n}} \cdot \nabla w(\mathbf{r}) - J_s(\mathbf{r}) = 0 \tag{5.29}$$

The term $J_s(\mathbf{r})$ is:

$$J_s(\mathbf{r}) = \frac{P}{A_s} \tag{5.30}$$

If a volume source (a 3D source of emission) is used, the volume power density is:

$$p = \frac{P}{V_s} \tag{5.31}$$

where V_s is the volume of the source.

5.2.4. Coupled enclosures

In the electromagnetic diffusion model, either single domain or multiple domain model can be used. For the latter case, the enclosures are coupled through apertures. We assume that the field in the aperture is well diffused, which is only holds for apertures above their cut-off frequency. In this thesis, we only use a two domain model.

Consider two enclosures forming domains V_1 and V_2 with diffusion coefficients D_1 and D_2 coupled by a translucent part of their shared boundary; the domain 1 side of the shared boundary is denoted by ∂V_{12} and the domain 2 side by ∂V_{21}. If the coupled area is not too large, we assume each cavity satisfies a diffusion equation:

$$(D_1\nabla^2 + \Lambda_1)w_1(\mathbf{r}) = P_1\delta^{(3)}(\mathbf{r} - \mathbf{r}_{s1}) \quad \mathbf{r} \in V_1 \tag{5.32}$$

$$(D_2\nabla^2 + \Lambda_2)w_2(\mathbf{r}) = P_2\delta^{(3)}(\mathbf{r} - \mathbf{r}_{s2}) \quad \mathbf{r} \in V_2 \tag{5.33}$$

On the non-shared walls, the Robin boundary condition applies:

$$[D_1\hat{\mathbf{n}}_1 \cdot \nabla + c\sum_{\alpha 1}(\mathbf{r})]w_1(\mathbf{r}) = 0 \quad \mathbf{r} \in \partial V_1/\partial V_{12} \tag{5.34}$$

$$[D_2\hat{\mathbf{n}}_2 \cdot \nabla + c\sum_{\alpha 2}(\mathbf{r})]w_2(\mathbf{r}) = 0 \quad \mathbf{r} \in \partial V_2/\partial V_{21} \tag{5.35}$$

where $\hat{\mathbf{n}}_1$ and $\hat{\mathbf{n}}_2$ are outward normal vectors in their respective domains. On the shared wall, the energy exchange boundary condition (EEBC) is applied [68]:

$$\hat{\mathbf{n}}_1 \cdot [D_1(\mathbf{r})\nabla w_1(\mathbf{r})] + h_{11}(\mathbf{r})w_1(\mathbf{r}) - h_{12}(\mathbf{r})w_2(\mathbf{r}) = 0 \quad \mathbf{r} \in \partial V_{12} \tag{5.36}$$

$$\hat{\mathbf{n}}_2 \cdot [D_2(\mathbf{r})\nabla w_2(\mathbf{r})] + h_{22}(\mathbf{r})w_2(\mathbf{r}) - h_{21}(\mathbf{r})w_1(\mathbf{r}) = 0 \quad \mathbf{r} \in \partial V_{21} \tag{5.37}$$

where the exchange coefficients $h_{11}(\mathbf{r})$ and $h_{22}(\mathbf{r})$ describe the power lost on their respectively sides of the boundary while $h_{12}(\mathbf{r})$ and $h_{21}(\mathbf{r})$ describe the power coupled in from the other side. If the aperture is lossless and reciprocal then:

$$h_{ij} = \frac{c\alpha_{ape}}{4} \quad i,j = 1,2 \tag{5.38}$$

where α_{ape} is the transmission efficiency of aperture. In the geometric optics regime the energy lost through an aperture is indistinguishable from that absorbed in a perfect absorber of the same area. Therefore, Flintoft et al argued that the energy exchange coefficient for an aperture should be given by [5]:

$$h_{ij} = \frac{c\alpha_{ape}}{2(2-\alpha_{ape})} \quad i,j = 1,2 \tag{5.39}$$

in order to be consistent with Jing et al's exchange coefficient for absorption, which is given in formula (5.13).

5.2.5. Relationship between the diffusion model and PWB method

The electromagnetic diffusion model is a generalization of the power balance (PWB) method. In this section, we show their relationship. Integrating the diffusion formula (5.3) over the whole volume of the space under test, applying Green's theorem and the inserting the Robin boundary condition on the space boundaries, we obtain the general energy balance relationship [69]:

$$c \oiint_A \sum_{\alpha}(\mathbf{r})\, w(\mathbf{r})dA + \Lambda U = P \tag{5.40}$$

where *U* is the total energy in the space and *A* is the boundary of the space. When the energy density *w*(**r**) is static and homogenous, inserting the Sabine's formula (5.11) and using formula (5.8), the diffusion formula (5.3) reduces to:

$$\left(\frac{1}{4}\alpha_{wall}A_{wall} + \frac{1}{4}\alpha_{con}A_{con}\right)cw = P \tag{5.41}$$

where α_{wall} and α_{con} are the absorption efficiencies of the walls and contents; A_{wall} and A_{con} are the surface areas of the walls and contents. Absorption efficiency and absorption cross section are related by:

$$\sigma_{a;wall} = \frac{\alpha_{wall}A_{wall}}{4} \tag{5.42}$$

$$\sigma_{a;con} = \frac{\alpha_{con}A_{con}}{4} \tag{5.43}$$

Substituting formulas (5.42) and (5.43) to (5.41), considering formula (5.2), we obtain the classic power balance relationship [3]:

$$\left(\sigma_{a;wall} + \sigma_{a;con}\right)S = P \tag{5.44}$$

The diffusion model is thus seen to be a natural generalization of the power balance method that treats the distributed nature of losses more accurately when the losses are significant.

5.3. Finite element solution of the diffusion model

The diffusion question can be solved numerically using a number of approaches such as the finite element method (FEM) and the Finite-Difference Time-Domain (FDTD) method. In this thesis, we follow Flintoft et al in using the FreeFEM++ software that is based on the FEM [70].

5.3.1. Weak form of the diffusion model

In order to use the finite element method to solve the diffusion formula (5.3), we need to derive its weak form. Weak form allows the transfer of the concepts of linear algebra to solve problems in other fields such as partial differential equations. An equation in its weak form is not required to hold absolutely and has weak solutions only with respect to certain test functions. The weak form of the diffusion equation is achieved by multiplying a test function *u*(**r**) and then integrating over the whole space to give [71]:

$$D\iiint_V u(\mathbf{r})\nabla^2 w(\mathbf{r})dV + \Lambda\iiint_V u(\mathbf{r})w(\mathbf{r})dV = P\iiint_V u(\mathbf{r})dV \tag{5.45}$$

Assume the all the functions are sufficiently smooth, we apply the divergence theorem:

$$\iiint_V \nabla \cdot \mathbf{F}(\mathbf{r}) dV = \oiint_{\partial V} \mathbf{F}(\mathbf{r}) dA \tag{5.46}$$

First putting **F**(**r**)=φ(**r**)**G**(**r**) we obtain:

$$\iiint_V [\varphi(\mathbf{r}) \nabla \cdot \mathbf{G}(\mathbf{r}) + \mathbf{G}(\mathbf{r}) \cdot \nabla \varphi(\mathbf{r})] dV = \oiint_{\partial V} \varphi(\mathbf{r}) \mathbf{G}(\mathbf{r}) dA \tag{5.47}$$

Then letting **G**(**r**)=γ(**r**)$\nabla\psi$(**r**) gives:

$$\iiint_V \{\varphi(\mathbf{r}) \nabla \cdot [\gamma(\mathbf{r}) \nabla \psi(\mathbf{r})] + \gamma(\mathbf{r}) \nabla \psi(\mathbf{r}) \cdot \nabla \varphi(\mathbf{r})\} dV = \oiint_{\partial V} \varphi(\mathbf{r}) \gamma(\mathbf{r}) \nabla \psi(\mathbf{r}) dA \tag{5.48}$$

where **F**(**r**), **G**(**r**), φ(**r**), γ(**r**) and ψ(**r**) are all test functions.

Now letting φ(**r**)= u(**r**), γ(**r**)=D, and ψ(**r**)=w(**r**), we have:

$$D \iiint_V u(\mathbf{r}) \nabla^2 w(\mathbf{r}) dV = D \oiint_{\partial V} u(\mathbf{r}) \nabla w(\mathbf{r}) dA - D \iiint_V \nabla u(\mathbf{r}) \nabla w(\mathbf{r}) dV \tag{5.49}$$

Formula (5.49) can be used to reduce the second order derivative term in formula (5.45) to obtain:

$$D \oiint_{\partial V} u(\mathbf{r}) \nabla w(\mathbf{r}) dS + D \iiint_V \nabla u(\mathbf{r}) \nabla w(\mathbf{r}) dV +$$

$$\Lambda \iiint_V u(\mathbf{r}) w(\mathbf{r}) dV = P \iiint_V u(\mathbf{r}) dV \tag{5.50}$$

The general form of the Robin boundary condition, which has been given in formula (5.9), is now inserted into formula (5.50) to give the weak form of the diffusion problem:

$$D \iiint_V \nabla u(\mathbf{r}) \nabla w(\mathbf{r}) dV + \Lambda \iiint_V u(\mathbf{r}) w(\mathbf{r}) dV$$

$$+c \oiint_{\partial V} u(\mathbf{r}) \sum_{\alpha}(\mathbf{r}) \, dA = P \iiint_V u(\mathbf{r}) dV \tag{5.51}$$

5.3.2. Discretisation and finite element space

In the FreeFEM++ software, the mesh is a discrete tessellation of the space using n elements of T_k:

$$V \approx \bigcup_{k=1}^{n} T_k \tag{5.52}$$

According to the user's menu of FreeFEM++, the meshes are typically triangles for 2D models and tetrahedral for 3D models [71]. The size of meshes for an accurate approximate solution is determined by the mean free path in the diffusion equation instead of frequency. Therefore, coarser meshes can be used in the diffusion model than in the full wave model. The boundary of the discrete space in denoted by ∂V and the finite element space on T_k is denoted by:

$$V_k(T_k, X) = \{w(\mathbf{r}) = \sum_{k=1}^{M} w_k \phi_k(\mathbf{r})\} \tag{5.53}$$

where X is the type of finite elements. In the version 3.6.1 of FreeFEM++, there are discontinuous, piecewise continuous, quadratic Lagrangian, Raviart-Thomas and a few other elements [71]. In this thesis, we follow Flintoft et al and use the piecewise continuous elements. M is the dimension of V_k. For example, M could be the total number of vertices, which is the number of elements times the number of matching points on each element. The term w_k is the degree of freedom of w. The basis function $\phi_k(\mathbf{r})$ is usually defined in terms of barycentric coordinates. For a point $\mathbf{r} \in T_k$, the barycentric coordinates ζ_i are:

$$\mathbf{r} = \sum_{i=1}^{L} \zeta_i \mathbf{r}_i \tag{5.54}$$

with

$$\sum_{i=1}^{L} \zeta_i = 1 \tag{5.55}$$

where $\mathbf{r}_i$ is the Lth vertices of T_k. The restriction of ϕ_i on T_k is then ζ_i.

Now using the Galerkin method we approximate both the energy density $w(\mathbf{r})$ and the test function $u(\mathbf{r})$ using the same finite element space:

$$w(\mathbf{r}) \approx \sum_{m=1}^{L} w_m \phi_m(\mathbf{r}) \tag{5.56}$$

$$u(\mathbf{r}) \approx \sum_{n=1}^{L} u_n \phi_n(\mathbf{r}) \tag{5.57}$$

where w_m and u_n are the degree of freedoms of w and u. Substituting formulas (5.56) and (5.57) to (5.51) to obtain:

$$D \sum_{n=1}^{L} \sum_{m=1}^{L} u_n w_m \iiint_V \nabla\phi_n(\mathbf{r}) \nabla\phi_m(\mathbf{r}) dV + \Lambda \sum_{n=1}^{L} \sum_{m=1}^{L} u_n w_m \iiint_V \phi_n(\mathbf{r}) \phi_m(\mathbf{r}) dV +$$
$$c \sum_{n=1}^{L} \sum_{m=1}^{L} u_n w_m \oiint_{\partial V} \sum_{\alpha}(\mathbf{r}) \phi_n(\mathbf{r}) \phi_m(\mathbf{r}) dA = P \sum_{n=1}^{L} u_n \iiint_V \phi_n(\mathbf{r}) dV \tag{5.58}$$

Denoting the discrete matrix operators by:

$$D_{nm} = D \iiint_V \nabla\phi_n(\mathbf{r})\nabla\phi_m(\mathbf{r})dV \tag{5.59}$$

$$M_{nm} = \Lambda \iiint_V \phi_n(\mathbf{r})\phi_m(\mathbf{r})dV \tag{5.60}$$

$$H_{nm} = c \oiint_{\partial V} \sum_{\alpha}(\mathbf{r})\phi_n(\mathbf{r})\phi_m(\mathbf{r})dA \tag{5.61}$$

$$P_n = P \iiint_V \phi_n(\mathbf{r})dV \tag{5.62}$$

where D_{nm} is the stiffness matrix, M_{nm}+H_{nm} is the dissipation matrix and P_n is the source matrix. Formula (5.58) can then be written as:

$$\sum_{n=1}^{L}\sum_{m=1}^{L} D_{ij}\, u_n w_m + \sum_{n=1}^{L}\sum_{m=1}^{L} M_{ij}\, u_n w_m + \sum_{n=1}^{L}\sum_{m=1}^{L} H_{ij}\, u_n w_m = \sum_{n=1}^{L} u_n\, P_n \tag{5.63}$$

Formula (5.63), when written in matrix form, is:

$$\mathbf{u}^{\mathrm{T}} D\mathbf{w} + \mathbf{u}^{\mathrm{T}} M\mathbf{w} + \mathbf{u}^{\mathrm{T}} H\mathbf{w} = \mathbf{u}^{\mathrm{T}} P \tag{5.64}$$

where **u** and **w** are column vectors containing the degree of freedoms and the superscript T denotes the transpose. Since the system is linear, formula (5.64) can be solved by testing each basis function separately. Therefore, it is equivalent to the linear system of ordinary differential equations:

$$(D + M + H)\mathbf{w} = P \tag{5.65}$$

5.3.3. Iterative methods for coupled domains

As has been mentioned, either single or dual domain model can be used in the diffusion approach. For the case of two domains coupled through a shared boundary where the energy exchange boundary condition (EEBC) is applied, the weak forms in each domain are:

$$D_1 \iiint_V \nabla w_1(\mathbf{r})\,\nabla u_1(\mathbf{r})dV + \Lambda_1 \iiint_V w_1(\mathbf{r})u_1(\mathbf{r})dV + c \oiint_{\partial V_1/\partial V_{12}} \sum_{\alpha 1}(\mathbf{r})\, w_1(\mathbf{r})u_1(\mathbf{r})\, dS +$$

$$\oiint_{\partial V_{12}} h_{11}(\mathbf{r})\, w_1(\mathbf{r})u_1(\mathbf{r})dS - \oiint_{\partial V_{12}} J_{12}(\mathbf{r})u_1(\mathbf{r})dS = P \iiint_V u_1(\mathbf{r})dV \tag{5.66}$$

$$D_2 \iiint_V \nabla w_2(\mathbf{r})\,\nabla u_2(\mathbf{r})dV + \Lambda_2 \iiint_V w_2(\mathbf{r})u_2(\mathbf{r})dV + c \oiint_{\partial V_2/\partial V_{21}} \sum_{\alpha 2}(\mathbf{r})\, w_2(\mathbf{r})u_2(\mathbf{r})\, dS +$$

$$\oiint_{\partial V_{21}} h_{22}(\mathbf{r})\, w_2(\mathbf{r})u_2(\mathbf{r})dS - \oiint_{\partial V_{21}} J_{21}(\mathbf{r})u_2(\mathbf{r})dS = P \iiint_V u_2(\mathbf{r})dV \tag{5.67}$$

The energy density flux coupled between the domains are:

$$J_{12}(\mathbf{r}) = h_{12}(\mathbf{r})w_2(\mathbf{r}) \quad \mathbf{r} \in \partial V_{12} \tag{5.68}$$

Figure 5. 3. Photograph of the 300mm×300mm×120mm enclosure under test with the 75mm×75mm square aperture.

$$J_{21}(\mathbf{r}) = h_{21}(\mathbf{r})w_1(\mathbf{r}) \quad \mathbf{r} \in \partial V_{21} \tag{5.69}$$

The system can be solved by using a Robin-Robin iterative algorithm [72]. We first initialise $J_{12}(\mathbf{r})$ using the power balance solution, $w_{2;PWB}$, in V_2:

$$J_{12}(\mathbf{r}) = h_{12}(\mathbf{r})w_{2;\mathrm{PWB}} \quad \mathbf{r} \in \partial V_{12} \tag{5.70}$$

Then solve formula (5.66) in domain V_1 using this solution to give $w_1(\mathbf{r})$. $J_{21}(\mathbf{r})$ can then be calculated from formula (5.69). In the same way, formula (5.67) in domain V_2 can be solved for $w_2(\mathbf{r})$. The process is repeated until the solution has converged. This typically requires a small number of iterations, for our case usually less than 10.

5.4. Test case specifications

In order to verify the usefulness of the diffusion model, we estimated the power density in a loaded enclosure by using the diffusion model and compared the estimation with those of full wave simulation and physical measurement. Figure 5.3 shows the photo of the enclosure under test. The length, width and height are 300mm, 300mm and 120mm respectively. We assume that the enclosure walls have a homogenous absorption efficiency α_{wall}. In [5], Flintoft

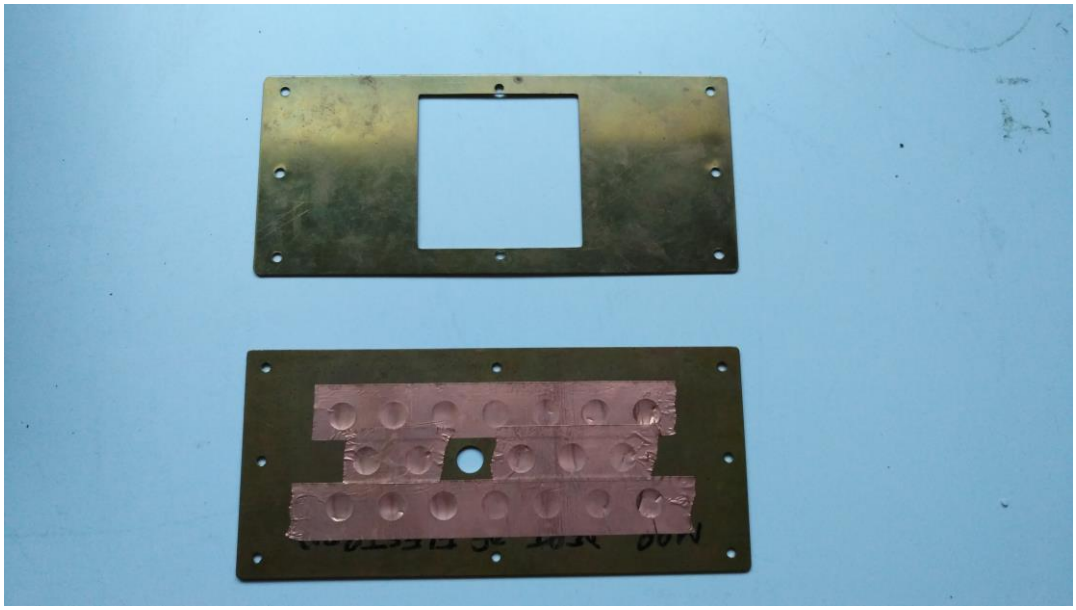

Figure 5. 4. Photograph of the 75mm×75mm square aperture and *r*=6mm circular aperture on removable planes.

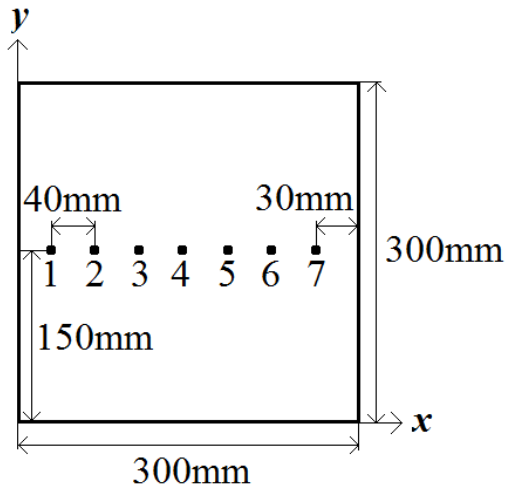

Figure 5. 5. Diagram of measurement points on the lid of the enclosure lid.

et al calculated the absorption efficiency of another enclosure by using the method detailed in section 5.2.2. Since the two enclosures are made from the same brass sheet, we consider them to have the same absorption efficiency α_{wall}=0.0027. The front face of the enclosure is removable to allow different apertures to be installed. In this work, we tested two scenarios, a 75mm×75mm square aperture and an *r*=6mm circular aperture which are shown in figure 5.4. The lid of the enclosure is removable as well to allow access and it is fitted with gaskets to ensure good electrical contact. There are seven measurement points with an interval of

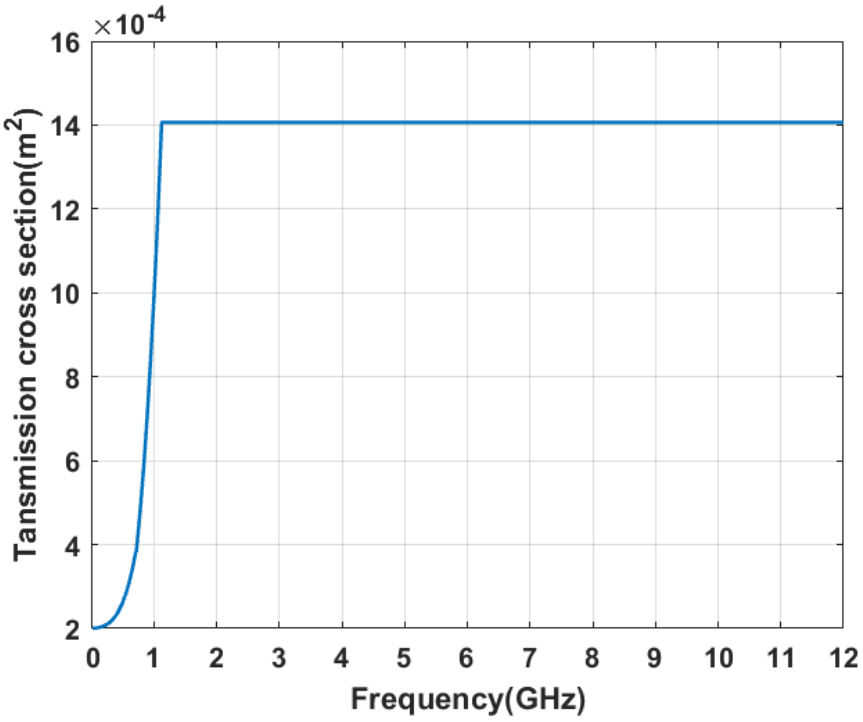

Figure 5. 6. Transmission cross section of the 75mm×75mm square aperture, showing the cut-off frequency at about 1GHz.

40mm along the central line of the lid in which a monopole probe can be installed. Figure 5.5 shows the diagram of the measurement points.

The transmission cross sections of the two apertures were calculated by the method presented in section 4.3 and the results are shown in figures 5.6 and 5.7. It can be seen that the cut-off frequencies of the 75mm×75mm square aperture and r=6mm circular aperture are about 1GHz and 10.2GHz respectively. Below the cut-off frequencies, their transmission cross sections increases with frequency; above the cut-off frequencies, the transmission cross sections become a constant, which is a quarter of their areas. For simplicity, the resonances around the cut-off frequency are neglected.

A series of absorbing cubes were placed the centre of the enclosure to introduce loss. Figure 5.8 shows the photograph of the three cubes used in this thesis. Their side lengths are 55mm, 70mm and 90mm respectively. Figure 5.9 shows the photograph of the enclosure that contains an absorbing cube. The cubes are made from the same LS22 radio absorbing material as the cylinder in [5] and hence we assume them to have the same absorption efficiency α_{con}=0.95. More details about the LS22 radio absorbing material will be given in section 5.6.

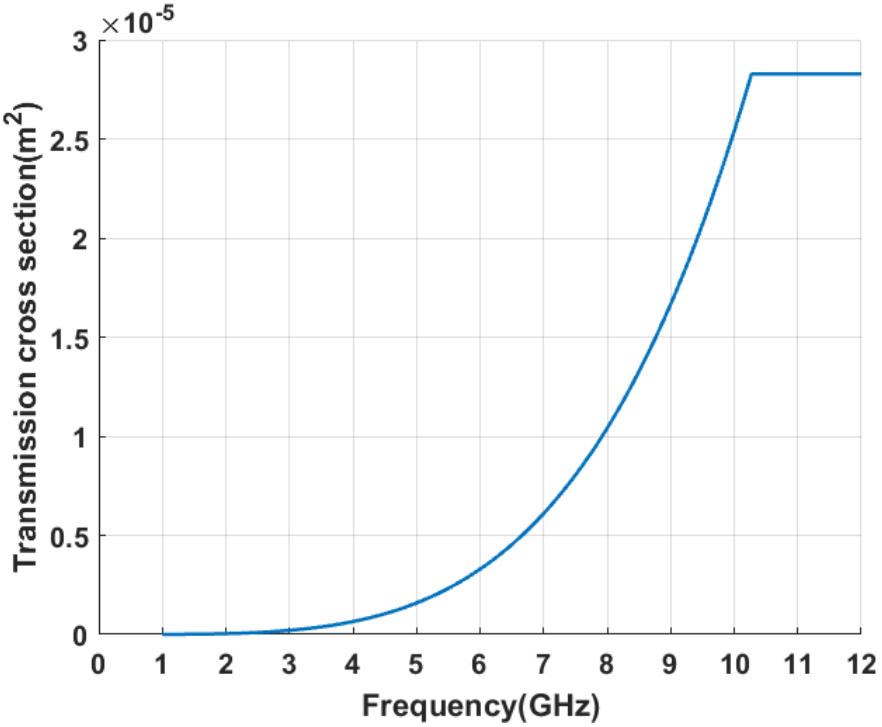

Figure 5. 7. Transmission cross section of the *r*=6mm circular aperture.

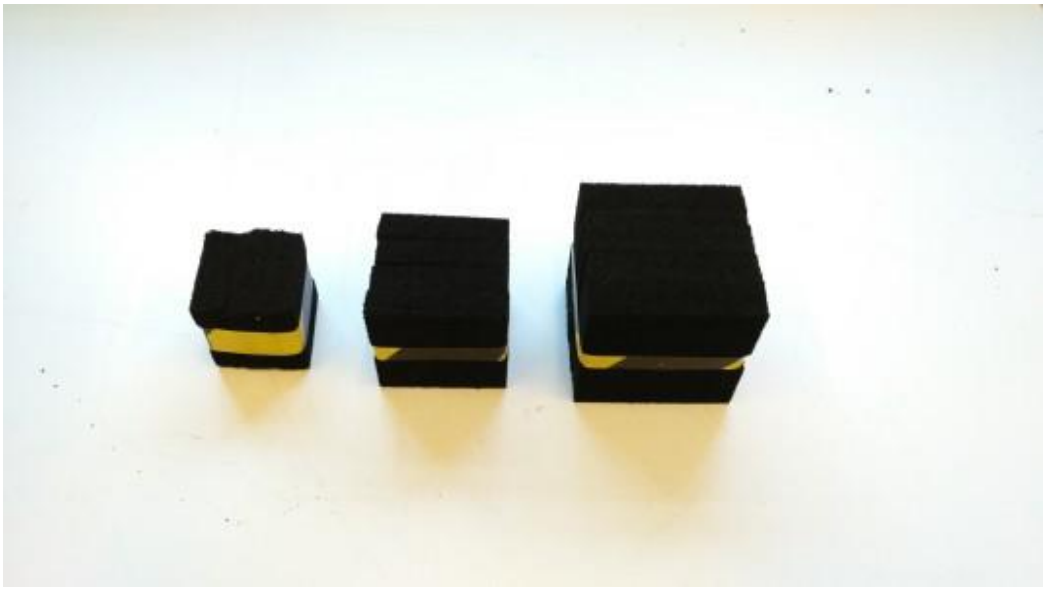

Figure 5. 8. Photograph of the absorbing cubes used in this thesis. Their side lengths are (from left to right) 55mm, 70mm and 90mm.

5.5. 3D Diffusion model of the enclosure under test

For the diffusion model, we tried both single and dual domain models and compared the results. The models were built by using the previously mentioned FreeFEM++ software [70].

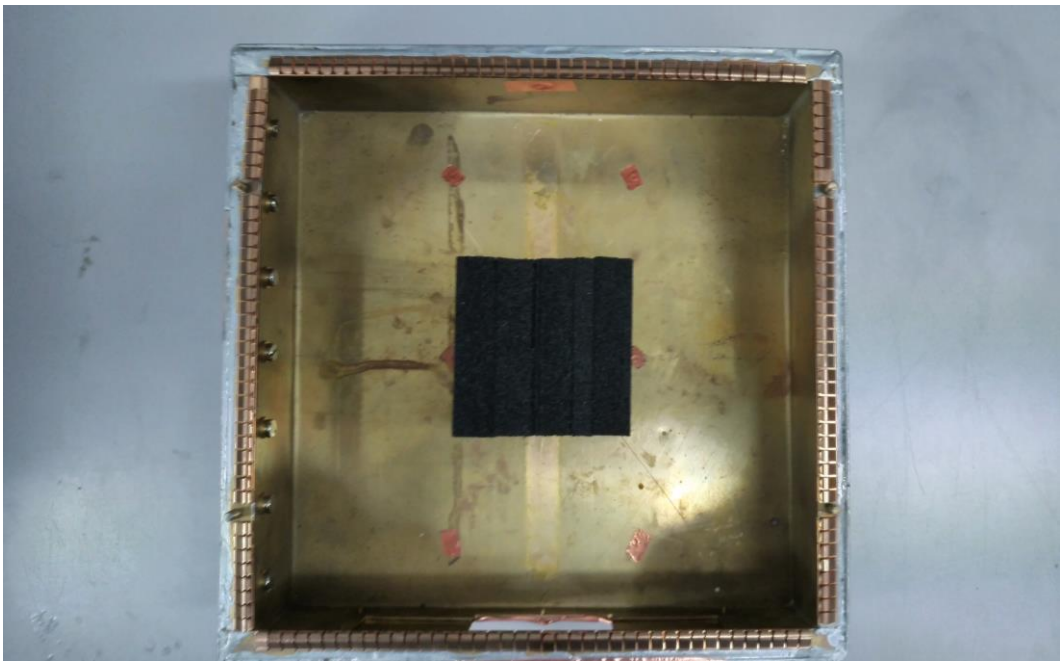

Figure 5. 9. Photograph of the top view of the 300mm×300mm×120mm enclosure without lid, showing the absorbing cube.

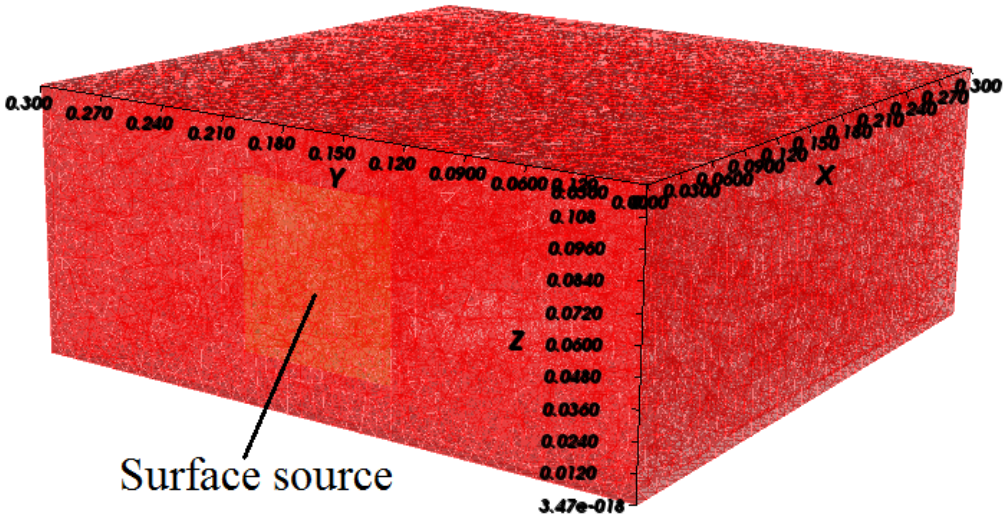

Figure 5. 10. Single domain diffusion model of the 300mm×300mm×120mm enclosure under test, showing the 75mm×75mm aperture, which serves as a surface source.

5.5.1. Single domain model

Figures 5.10 and 5.11 show the single domain model of the enclosure under test with the 75mm×75mm square aperture. The 3D mesh is created by a built-in generator TetGen [73]. The walls and the cube are modelled by including their surfaces in the mesh and applying the Robin boundary condition, with a proper absorption efficiency. Since there is only surface loss

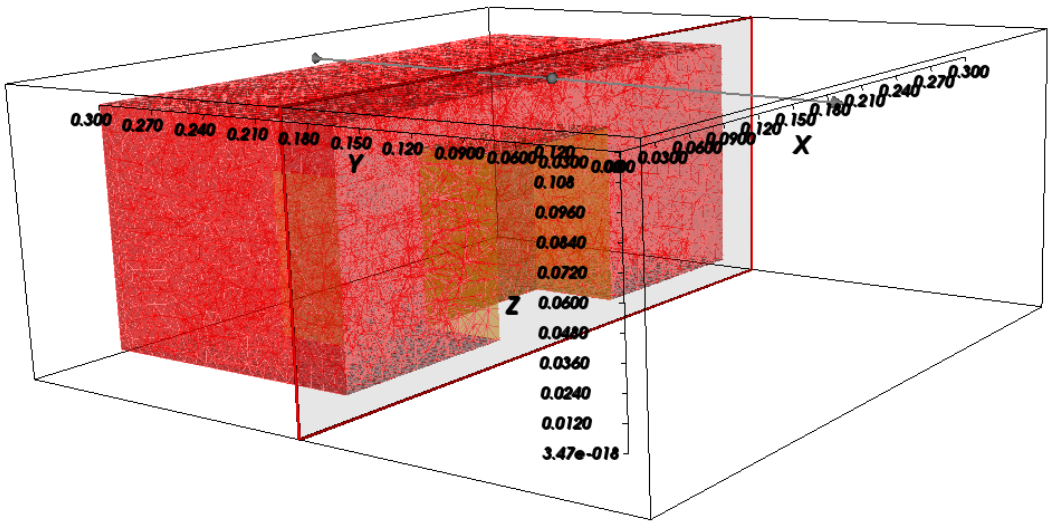

Figure 5. 11. Cross sectional view of the single domain diffusion model of the 300mm×300mm×120mm enclosure under test with the 75mm×75mm aperture, showing the absorbing cube inside it.

in the model, the volumetric loss rate Λ in formula (5.3) is zero. The aperture area serves as a surface source and the exitance is determined by formula (5.30), where the power P can be manually set. In both single and dual domain diffusion models, the mesh size is between 10mm and 30mm.

As has been mentioned in formula (5.53), FreeFEM++ offers a variety of finite elements. Here we follow Flintoft et al and use the piecewise P1 type continuous elements. In addition, FreeFEM++ contains several linear direct and iterative solvers such as lower-upper (LU), Crout, Cholesky, conjugate gradient (CG) and so on. Since the problem is linear, we choose the CG solver with the stopping criteria of 0.001 on the residual. The simulation took less than 10 iterations and only a few seconds to finish on a desktop computer (Windows 7, Intel Core i7-870 @ 2.93GHz, 8GB RAM).

5.5.2. Dual domain model

Figure 5.12 shows the diagram of the top view of the dual domain model. Domain B represents the enclosure under test and domain A represents a reverberation chamber. Both domains are modelled as continuous while the diffusivity in formula (5.3) is inhomogeneous in order to assign appropriate values in each domain:

$$D = \begin{cases} D_1 & x < 0 \\ D_2 & x \geq 0 \end{cases} \tag{5.71}$$

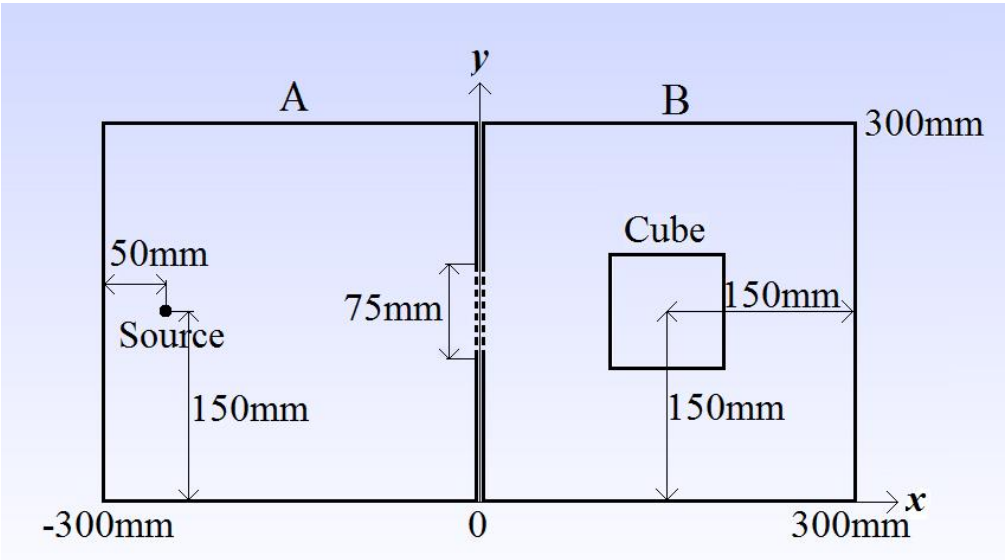

Figure 5. 12. Diagram of the top view of the dual domain diffusion model of the 300mm×300mm×120mm enclosure with the 75mm×75mm square aperture. Domain A represents a reverberation chamber that contains a point source while domain B represents the enclosure under test. The two domains are coupled through a shared boundary that represents the aperture.

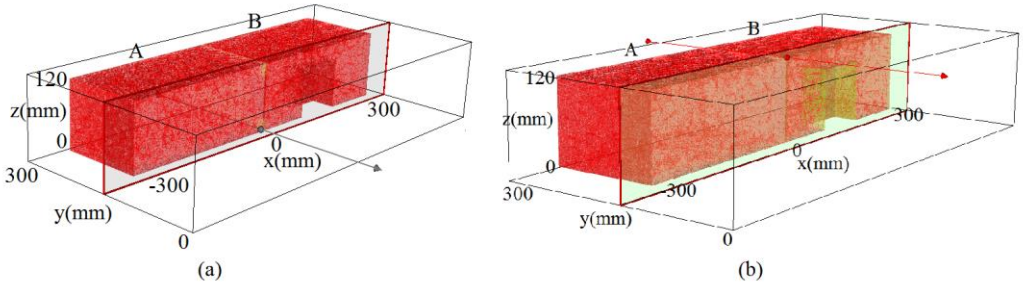

Figure 5. 13. Cross section view along y-axis of the dual domain diffusion model of the 300mm×300mm×120mm enclosure with: (a) the 75mm×75mm square aperture and (b) *r*=6mm circular aperture. Domains A and B are in accordance with those shown in figure 5.12.

The two domains are not connected, only coupled through a shared boundary (the aperture) to which the energy exchange boundary condition (EEBC) is applied with a unity transmission efficiency. The dimension of domain A is not significant as long as the aperture is an adequate distance (at least a quarter wavelength) away from the source. Here we use a small domain to represent a reverberation chamber to reduce the computational effort and we let the two domains have the same dimension only for convenience. Figures 5.13 and 5.14 show different cross sectional views of the dual domain model.

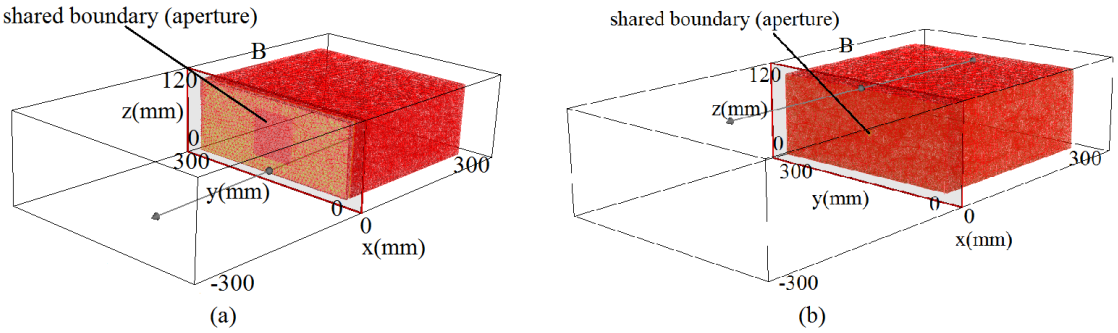

Figure 5. 14. Cross section view along x-axis of the dual domain diffusion model of the 300mm×300mm×120mm enclosure with: (a) the 75mm×75mm square aperture and (b) *r*=6mm circular aperture, showing only domain B and the shared boundary.

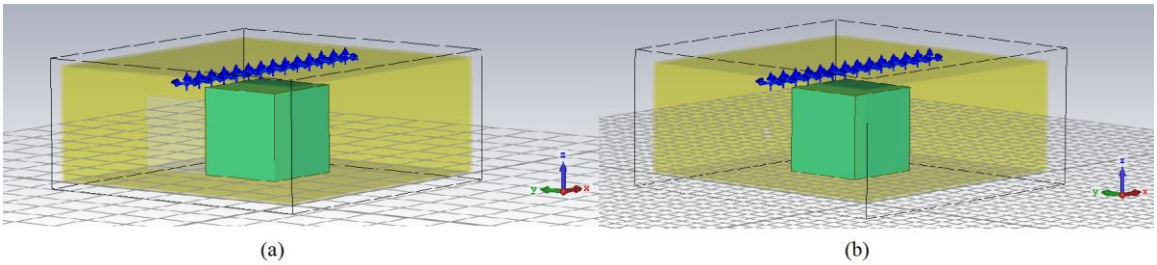

Figure 5. 15. Full wave model of the 300mm×300mm×120mm enclosure with: (a) the 75mm×75mm square aperture and (b) *r*=6mm circular aperture, showing the absorbing cube and the probes.

In domain A, an ideal point source is set at half height. According to formula (5.27), the energy density in the vicinity of the source should be discarded. To the best of our knowledge, we have not found any guidance on choosing the distance to discard. Therefore, we decided to get rid of the energy density within 50mm, which is about half the mean free path of the domain, of the point source.

5.6. Full wave model of the enclosure under test

In this thesis, full wave simulations are presented as a reference and they were performed by using the CST Microwave Studio 2016 software [74].

5.6.1. CST model of the enclosure and the cube

Figure 5.15 shows the full wave model of the enclosure with the cube. A number of probes was defined along the central line of the lid. They record both electric and magnetic fields in *x*, *y* and *z* directions. The power density can be calculated by using formulas (5.1) and (5.2). Figure 5.16 shows a diagram of the top view of the CST model, which provides a better view

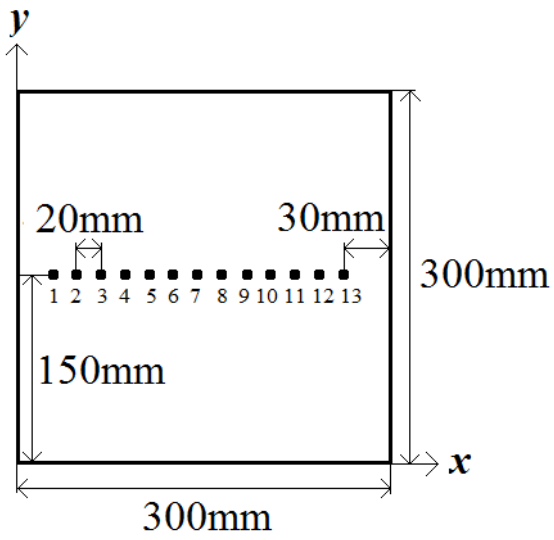

Figure 5. 16. Diagram of the top view of the full wave model of the 300mm×300mm×120mm enclosure, showing the probe positions.

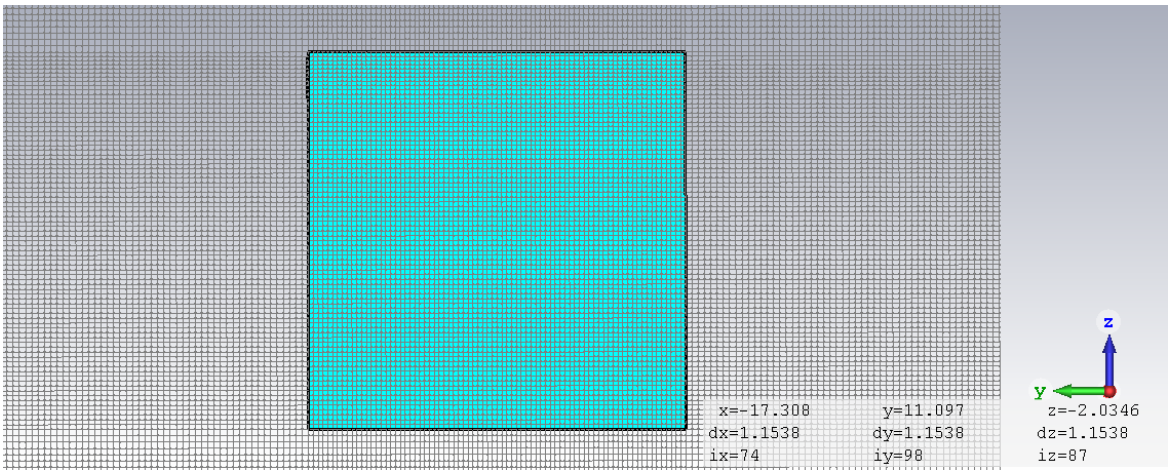

Figure 5. 17. Cross sectional view of the mesh lines for the full wave model of the absorbing cube.

of the probe positions. It can be noticed that there are more probes in the full wave model than in the actual enclosure. This is because in CST, it takes no extra effort to define a probe and we put more probes in order to get results with better resolution.

The absorbing cubes were modelled by using a three-pole Debye dispersion model [75]:

$$\hat{\varepsilon} = \varepsilon_{\infty} + \sum_{i=1}^{3} \frac{\Delta\varepsilon_i}{1+j\omega\tau_i} + \frac{\sigma_{DC}}{j\omega\varepsilon_0} \tag{5.72}$$

where ω is the angular frequency, ε_0=8.85×10^{-12} F/m is the vacuum permittivity, ε_∞=1.1725, $\Delta\varepsilon_1$=1.04×10^{-3}, $\Delta\varepsilon_2$=17.9, $\Delta\varepsilon_3$=0.49, time constants τ_1=55.3ms, τ_2=0.188ns, τ_3=6.2ps and the

conductivity σ_{DC}=0.1mS/m. The CST software has built-in support for calculating the ACS of an object illuminated by plane waves using a far-field monitor. This also supports parametric sweeps. The absorption cross section for each plane wave can be exported for post-processing. Figure 5.17 shows the full wave model of the absorbing cube. Previously, Zhang has measured the absorption cross sections of the absorbing cubes by using the time domain method detailed in section 4.4.2 [76]. In order to validate the full wave models of the cubes, we compared the simulated ACSs of them to those of physical measurements. The results will be presented later in this chapter.

Considering the computation time and memory requirement, we only simulated the field from 1GHz to 10GHz. We used the time domain solver and hexahedral mesh. The mesh density was set as 15 mesh cells per wavelength at central frequency, which is the default setting. For the empty enclosure and the enclosure loaded with the 55mm×55mm×55mm, 70mm×70mm×70mm and 90mm×90mm×90mm absorbing cube, the total number of mesh cells are 2.8 million, 3.4 million, 3.7 million and 4 million respectively.

Because a computer can only calculate problems that have a finite expansion, it is necessary to specify the boundary. Here we use the default open boundary as the boundary condition of the CST model. According to the user's manual, open boundary behaves like free space with minimal reflections and the default reflection coefficient is 0.0001. The minimum distance from the boundary to the enclosure is a quarter wavelength, which is the default setting. Here the wavelength is determined by the centre frequency and for this case is 5.5GHz.

The energy convergence criterion was set as -60dB. It is a value for the accuracy of the frequency domain signals that are calculated by Fourier Transformation of the time signals. Every simulation stops at some time. This means that the signals that are calculated are truncated at this point, regardless of their values. If these values are non-zero, the Fourier Transformation will produce an error because only a part of the "whole" signal with all of its non-zero values has been used for the transformation. Apparently, the "smaller" the signals are, the more accurate the frequency domain values will be. Currently there is no standard or guidance on choosing the accuracy for a specific type of simulation, but empirically a 30dB energy decay would provide acceptable results in most cases. Figure 5.18 shows an example of the energy convergence criterion in CST simulation.

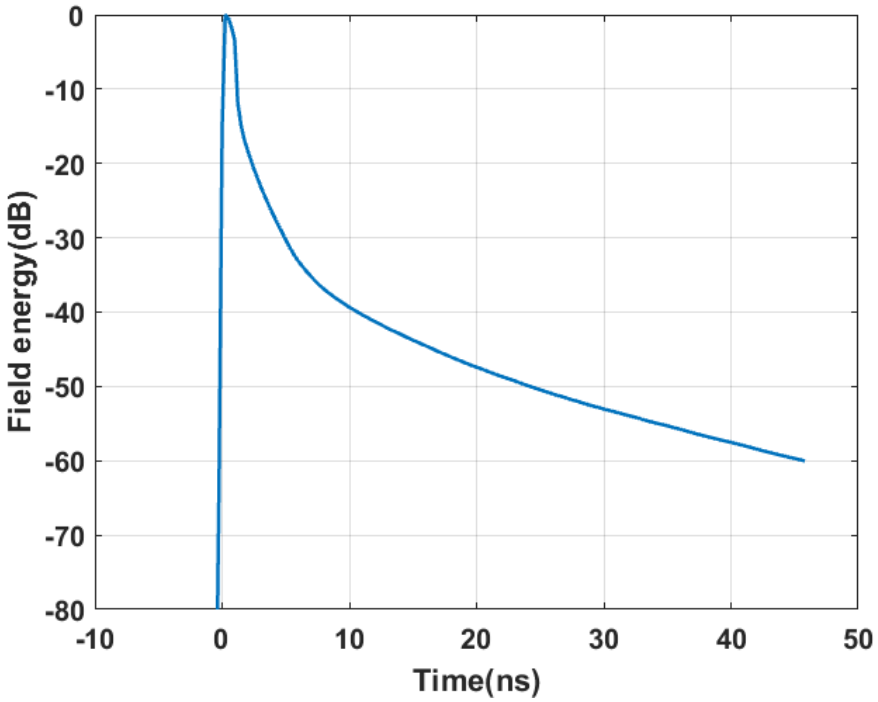

Figure 5. 18. Example of energy convergence criterion in full wave simulation. The simulation stops when the defined accuracy level is reached.

In this work, all the full wave simulations were performed on the York Advanced Research Computing Cluster (YARCC), which has a variety of processor types, typically Intel E5-2760 v2 @ 2.5GHz with 16 cores [77]. For the enclosure loaded with the 55mm×55mm×55mm, 70mm×70mm×70mm and 90mm×90mm×90mm absorbing cube, the CST simulations took 10, 25 and 42 hours to finish respectively.

5.6.2. Creation of a reverberant electromagnetic environment in CST

As has been mentioned, the use of the diffusion model requires the presence of a diffuse field. There are two methods to meet this requirement in CST: 1. Put a mechanical stirrer in the enclosure under test; 2. Use a superposition of a finite number of plane waves to illuminate the enclosure under test from different positions. The first method would greatly increase the number of mesh cells and thus the simulation time because a stirrer is a complex structure. Therefore, we adopted the second method.

In [78], Hill introduced a plane wave integral representation that satisfies Maxwell's equations for fields in a well-stirred reverberation chamber. Figure 5.19 shows an illustration of

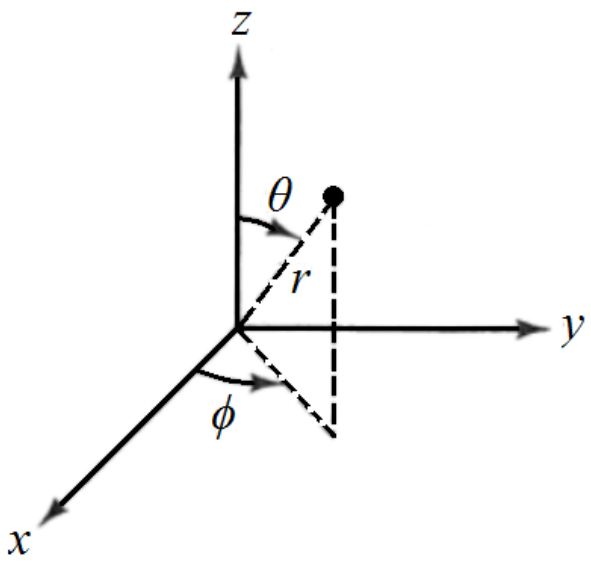

Figure 5. 19. Illustration of spherical coordinate. ϑ and φ are polar and azimuthal angles respectively.

spherical coordinate. The electric field at a certain location **r** within a chamber can be represented as an integral of plane waves over all solid angles:

$$E(\mathbf{r}) = \iint_{4\pi} \mathbf{F}(\Omega) e^{j\mathbf{k}\cdot\mathbf{r}} \sin\theta d\theta d\varphi \tag{5.73}$$

where the solid angle Ω is the shorthand for ϑ and φ and $d\Omega=\sin\vartheta d\vartheta d\varphi$. The vector wavenumber **k** is given by (in Cartesian coordinate):

$$\mathbf{k} = k(\hat{\mathbf{x}}\sin\theta\cos\varphi + \hat{\mathbf{y}}\sin\theta\sin\varphi + \hat{\mathbf{z}}\cos\theta) \tag{5.74}$$

where k is scalar wave number.

The angular spectrum **F**(Ω) is given by:

$$\mathbf{F}(\Omega) = \hat{\boldsymbol{\theta}} F_\theta(\Omega) + \hat{\boldsymbol{\varphi}} F_\varphi(\Omega) \tag{5.75}$$

where $\hat{\boldsymbol{\theta}}$ and $\hat{\boldsymbol{\varphi}}$ are unit vectors that are mutually orthogonal and they both are orthogonal to **k**. $F_\vartheta(\Omega)$ and $F_\varphi(\Omega)$ are complex field amplitudes that can be expressed by their real and imaginary parts:

$$F_\theta(\Omega) = F_{\theta r}(\Omega) + jF_{\theta i}(\Omega) \tag{5.76}$$

$$F_\varphi(\Omega) = F_{\varphi r}(\Omega) + jF_{\varphi i}(\Omega) \tag{5.77}$$

Hill pointed out that in an ideal reverberation chamber, the mean value of angular spectrum should be zero since the phase of the spectrum is random due to multiple bounces from chamber walls [78]:

$$\langle F_{\boldsymbol{\theta}}(\Omega)\rangle = \langle F_{\varphi}(\Omega)\rangle = 0 \tag{5.78}$$

where the symbol <·> denotes ensemble average such as mechanical stirring or frequency stirring. In addition, the bounces change the polarization as well. Therefore, angular spectrum with orthogonal polarizations or quadrature phases should be uncorrelated:

$$\langle F_{\boldsymbol{\theta r}}(\Omega_1)F_{\boldsymbol{\theta i}}(\Omega_2)\rangle = \langle F_{\varphi \boldsymbol{r}}(\Omega_1)F_{\varphi \boldsymbol{i}}(\Omega_2)\rangle = \langle F_{\boldsymbol{\theta r}}(\Omega_1)F_{\varphi \boldsymbol{r}}(\Omega_2)\rangle = \langle F_{\boldsymbol{\theta i}}(\Omega_1)F_{\varphi \boldsymbol{i}}(\Omega_2)\rangle =$$
$$\langle F_{\boldsymbol{\theta r}}(\Omega_1)F_{\varphi \boldsymbol{i}}(\Omega_2)\rangle = \langle F_{\boldsymbol{\theta i}}(\Omega_1)F_{\varphi \boldsymbol{r}}(\Omega_2)\rangle = 0 \tag{5.79}$$

In a numerical simulation, electric field E(**r**) in formula (5.73) is discretised by using the Legendre/uniform sampling method [79]:

$$E(\mathbf{r}) = \sum_{l=1}^{L_{GL}}\sum_{m=1}^{L_{GL}} \mathbf{F}_{lm} e^{j\mathbf{k}_{lm}\cdot\mathbf{r}} \tag{5.80}$$

Here the polar angle ϑ is sampled at the L_{GL} zeros of the Legendre polynomial $P_L(\cos\vartheta)$ and the azimuthal angle φ is sampled at $2L_{GL}$ uniformly spaces points. The discretized wavenumber $\mathbf{k}_{lm}$ is given by:

$$\mathbf{k}_{lm} = k(\hat{\mathbf{x}}\sin\theta_l\cos\varphi_m + \hat{\mathbf{y}}\sin\theta_l\sin\varphi_m + \hat{\mathbf{z}}\cos\theta_l) \tag{5.81}$$

where $\cos\vartheta_l$ and φ_m are given by:

$$P_L(\cos\theta_l) = 0 \;\; (l = 1,2,\dots\dots,L_{GL}) \tag{5.82}$$

$$\varphi_m = \frac{m\pi}{L_{GL}} \quad (m = 1,2,\dots\dots,2L_{GL}) \tag{5.83}$$

The Legendre polynomial is given by (in terms of Rodriguez's formula) [80]:

$$P_n(x) = \frac{1}{2^n n!}\frac{d^n}{dx^n}(x^2-1)^n \tag{5.84}$$

where n=L_{GL} that is the order of the polynomial and x=$\cos\vartheta_l$.

By using the Legendre/uniform sampling method, the mean squared of electric field is given by:

$$\langle |E(\mathbf{r})|^2\rangle = \sum_{l=1}^{L_{GL}}\sum_{m=1}^{2L_{GL}}\sum_{l'=1}^{L_{GL}}\sum_{m'=1}^{2L_{GL}}\langle \mathbf{F}_{lm}\cdot\mathbf{F}^*_{l'm'}\rangle\, e^{j(\mathbf{k}_{lm}-\mathbf{k}_{l'm'})} = \sum_{l=1}^{L_{GL}}\sum_{m=1}^{2L_{GL}}\langle|\mathbf{F}_{lm}|^2\rangle \tag{5.85}$$

According to formulas (5.78) and (5.79), $\mathbf{F}_{lm}$ are mutually independent and therefore:

$$\langle \mathbf{F}_{lm} \cdot \mathbf{F}^*_{l'm'} \rangle = 0 \text{ when } l \neq l' \text{ or } m \neq m' \tag{5.86}$$

Same as formulas (5.75), (5.76) and (5.77), discretized spectrum $\mathbf{F}_{lm}$ in formula (5.80) can be expressed by their real and imaginary parts as well [79]:

$$\mathbf{F}_{lm} = \widehat{\boldsymbol{\theta}} F_{lm;\theta} + \widehat{\boldsymbol{\varphi}} F_{lm;\varphi} = \widehat{\boldsymbol{\theta}} \left(F_{lm;\theta r} + F_{lm;\theta i} \right) + \widehat{\boldsymbol{\varphi}} \left(F_{lm;\varphi r} + F_{lm;\varphi i} \right) \tag{5.87}$$

Applying uniform sampling method to azimuthal angle φ and Legendre/uniform sampling method to polar angle ϑ, formula (5.85) is satisfied when:

$$\langle |\mathbf{F}_{lm}|^2 \rangle = w_l \frac{E_0^2}{4L_{GL}} \tag{5.88}$$

where w_l is Gauss-Legendre quadrature weighting factor on interval [-1, 1] and

$$E_0^2 = \langle |E(\mathbf{r})|^2 \rangle \tag{5.89}$$

West et al state that formula (5.88) is satisfied when all terms in formula (5.87) follow normal distribution N (mean, standard deviation):

$$F_{lm;\theta r}, F_{lm;\theta i}, F_{lm;\varphi r}, F_{lm;\varphi i} \sim \mathcal{N}\left(0, w_l \frac{E_0^2}{16 L_{GL}}\right) \tag{5.90}$$

The spatial bandwidth of the field in a reverberation chamber needs to be adequately sampled by the discretisation of the plane-wave expansion. West et al showed an empirical formula to determine the order L_{GL} required [79]:

$$L_{GL} \geq \pi + 10 D_{\max} f_{\max} \tag{5.91}$$

where $D_{\max}$ is the maximum dimension of the working volume in metre and $f_{\max}$ is the upper frequency limit of the simulation in gigahertz.

The workload required to simulate a reverberant electromagnetic environment is related to a linear operator [79]:

$$O(\mathbf{r}) = \hat{O}[E(\mathbf{r})] \tag{5.92}$$

Substitute formulas (5.80) and (5.87) into (5.92) gives:

$$O(\mathbf{r}) = \sum_{l=1}^{L_{GL}} \sum_{m=1}^{2L_{GL}} \left(F_{lm;\theta} O_{lm;\theta} + F_{lm;\varphi} O_{lm;\varphi} \right) \tag{5.93}$$

where

$$O_{lm;\theta} = \hat{O}\left(\hat{\boldsymbol{\theta}} e^{j\mathbf{k}_{lm}\cdot\mathbf{r}}\right) \tag{5.94}$$

$$O_{lm;\varphi} = \hat{O}\left(\hat{\boldsymbol{\varphi}} e^{j\mathbf{k}_{lm}\cdot\mathbf{r}}\right) \tag{5.95}$$

are the values of the operator due to a single unit amplitude plane wave. Formula (5.93) indicates that $4\,L_{GL}^2$ simulations are required to replicate a diffuse environment (two orthogonal field polarizations from $2L_{GL}^2$ directions).

The implication of the analysis above is that an accurate simulation of a diffuse field could be computationally expensive. For example, for an upper frequency of 10GHz and working volume of a cube with side length of 0.09m, we find L_{GL}≥12.14. Let L_{GL}=13, then $4L_{GL}^2$=676. This is beyond our practical simulation resources. Consideration of the theoretical derivation of the spatial sampling in [81] suggests that it is defined to make the truncation error negligible. In [75], Flintoft et al used 64 plane waves (which means L_{GL}=4) to illuminate dissipative objects in full wave simulations in order to obtain their absorption cross sections. They stated that using 64 plane waves achieved an absorption cross section within 1 dB accuracy.

In the CST software, electric and magnetic fields are parameterized as:

$$\mathbf{E} = E_0\left(-\cos\psi\hat{\boldsymbol{\theta}} + \sin\psi\hat{\boldsymbol{\varphi}}\right) \tag{5.96}$$

$$\mathbf{H} = \eta_0^{-1}\mathbf{k}\times\mathbf{E} = \eta_0^{-1}E_0\left(\cos\psi\hat{\boldsymbol{\varphi}} + \sin\psi\hat{\boldsymbol{\theta}}\right) \tag{5.97}$$

where η_0≈377Ω is the free space impedance and ψ is the polarization angle of the incident waves. ψ=0 and ψ=π/2 correspond to horizontal and vertical polarizations. The Cartesian components of the incident electric and magnetic fields are given by:

$$\mathbf{E} = -E_0\cos\psi\begin{pmatrix}\cos\theta\cos\varphi\\ \cos\theta\sin\varphi\\ -\sin\theta\end{pmatrix} + E_0\sin\psi\begin{pmatrix}-\sin\varphi\\ \cos\varphi\\ 0\end{pmatrix} \tag{5.98}$$

$$\mathbf{H} = \eta_0^{-1}E_0\cos\psi\begin{pmatrix}-\sin\varphi\\ \cos\varphi\\ 0\end{pmatrix} + \eta_0^{-1}E_0\sin\psi\begin{pmatrix}\cos\theta\cos\varphi\\ \cos\theta\sin\varphi\\ -\sin\theta\end{pmatrix} \tag{5.99}$$

The CST software uses formulas (5.74) and (5.98) to determine the plane wave directions. The angles ϑ and φ are chosen by using formulas (5.82) and (5.83). During the full wave simulation,

we used the parametric sweep function over plane waves' directions. The directions of the 64 plane waves are listed in table 5.1.

Table 5. 1. Incident angles of the 64 plane waves in full wave simulation in order to create a reverberant electromagnetic environment. ϑ, ϕ and ψ are polar, azimuthal and polarization angles respectively.

ϑ	φ	ψ
0.8π	0.25π	0
0.8π	0.5π	0
0.8π	0.75π	0
0.8π	π	0
0.8π	1.25π	0
0.8π	1.5π	0
0.8π	1.75π	0
0.8π	2π	0
0.6π	0.25π	0
0.6π	0.5π	0
0.6π	0.75π	0
0.6π	π	0
0.6π	1.25π	0
0.6π	1.5π	0
0.6π	1.75π	0
0.6π	2π	0
0.4π	0.25π	0
0.4π	0.5π	0
0.4π	0.75π	0
0.4π	π	0
0.4π	1.25π	0
0.4π	1.5π	0
0.4π	1.75π	0
0.4π	2π	0
0.2π	0.25π	0

0.2π	0.5π	0
0.2π	0.75π	0
0.2π	π	0
0.2π	1.25π	0
0.2π	1.5π	0
0.2π	1.75π	0
0.2π	2π	0
0.8π	0.25π	0.5π
0.8π	0.5π	0.5π
0.8π	0.75π	0.5π
0.8π	π	0.5π
0.8π	1.25π	0.5π
0.8π	1.5π	0.5π
0.8π	1.75π	0.5π
0.8π	2π	0.5π
0.6π	0.25π	0.5π
0.6π	0.5π	0.5π
0.6π	0.75π	0.5π
0.6π	π	0.5π
0.6π	1.25π	0.5π
0.6π	1.5π	0.5π
0.6π	1.75π	0.5π
0.6π	2π	0.5π
0.4π	0.25π	0.5π
0.4π	0.5π	0.5π
0.4π	0.75π	0.5π
0.4π	π	0.5π
0.4π	1.25π	0.5π
0.4π	1.5π	0.5π
0.4π	1.75π	0.5π
0.4π	2π	0.5π

0.2π	0.25π	0.5π
0.2π	0.5π	0.5π
0.2π	0.75π	0.5π
0.2π	π	0.5π
0.2π	1.25π	0.5π
0.2π	1.5π	0.5π
0.2π	1.75π	0.5π
0.2π	2π	0.5π

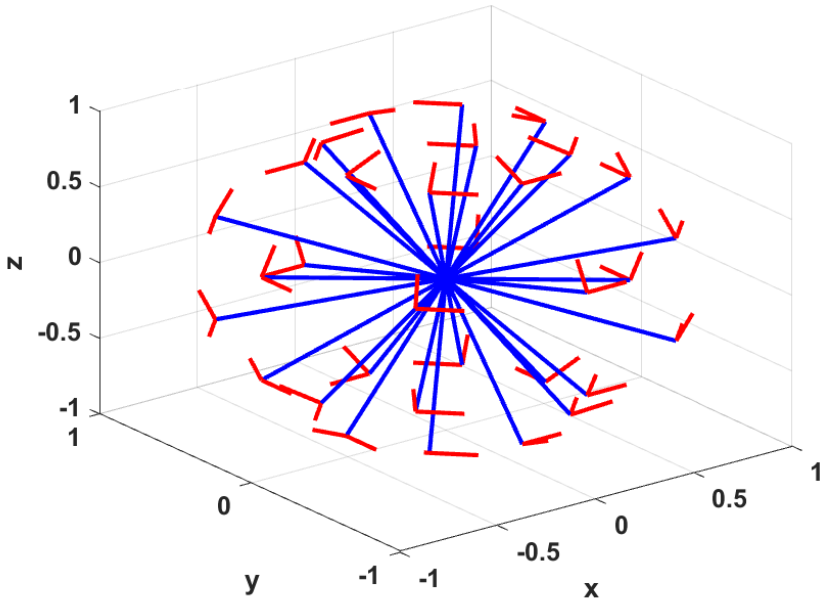

Figure 5. 20. Diagram of the incident angles of the 64 plane waves in full wave simulation in order to create a reverberant electromagnetic environment. There are 32 positions and at each position, there are two polarizations.

Figure 5.20 shows a diagram of the incident angles of the 64 plane waves. It can be seen that there are 32 incident positions and at each position, there are two polarizations. In this thesis, in order to further save time, we used L_{GL}=3 that leads to 36 plane waves. Later in this chapter, we will present examples to show that 36 plane waves and 64 plane waves produce very similar results. Table 5.2 lists the incident angles of the 36 plane waves.

Table 5. 2. Incident angles of the 36 plane waves in full wave simulation in order to create a reverberant electromagnetic environment. ϑ, ϕ and ψ are polar, azimuthal and polarization angles respectively.

ϑ	φ	ψ
0.8π	π/3	0
0.8π	2π/3	0
0.8π	π	0
0.8π	4π/3	0
0.8π	5π/3	0
0.8π	2π	0
0.5π	π/3	0
0.5π	2π/3	0
0.5π	π	0
0.5π	4π/3	0
0.5π	5π/3	0
0.5π	2π	0
0.2π	π/3	0
0.2π	2π/3	0
0.2π	π	0
0.2π	4π/3	0
0.2π	5π/3	0
0.2π	2π	0
0.8π	π/3	0.5π
0.8π	2π/3	0.5π
0.8π	π	0.5π
0.8π	4π/3	0.5π
0.8π	5π/3	0.5π
0.8π	2π	0.5π
0.5π	π/3	0.5π
0.5π	2π/3	0.5π
0.5π	π	0.5π

0.5π	4π/3	0.5π
0.5π	5π/3	0.5π
0.5π	2π	0.5π
0.2π	π/3	0.5π
0.2π	2π/3	0.5π
0.2π	π	0.5π
0.2π	4π/3	0.5π
0.2π	5π/3	0.5π
0.2π	2π	0.5π

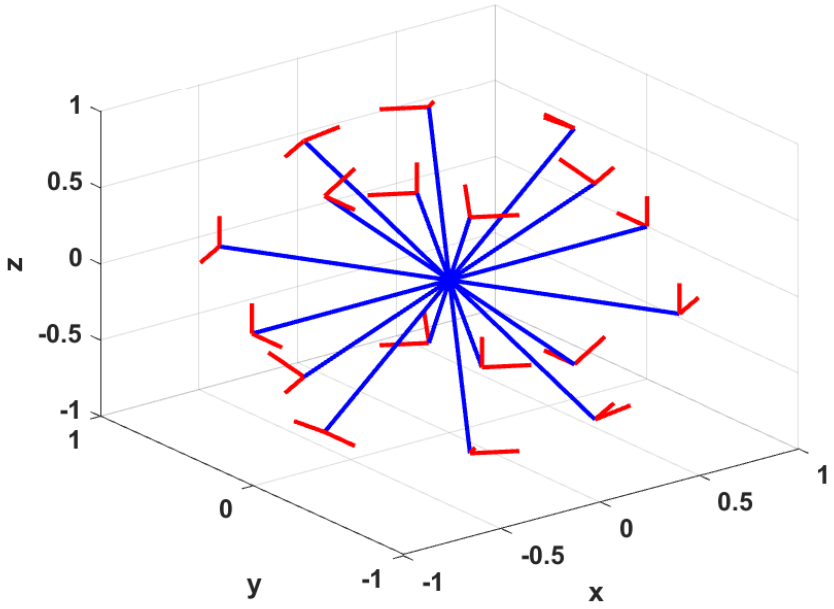

Figure 5. 21. Diagram of the incident angles of the 36 plane waves in full wave simulation in order to create a reverberant electromagnetic environment. There are 18 positions and at each position, there are two polarizations.

Figure 5.21 shows a diagram of the incident angles of the 36 plane waves. It can be seen that there are 18 incident positions and at each position, there are two polarizations.

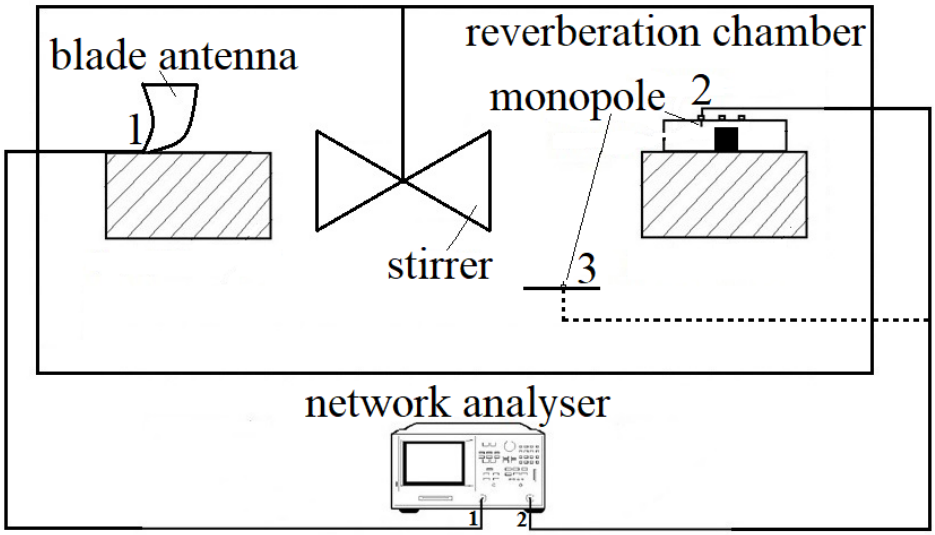

Figure 5. 22. Diagram of the validation measurements set up. The measurements were performed in the reverberation chamber at the University of York. Antenna 1 is the radiation source. Antennas 2 and 3 are two monopoles that are fitted in the enclosure and a metal plane respectively.

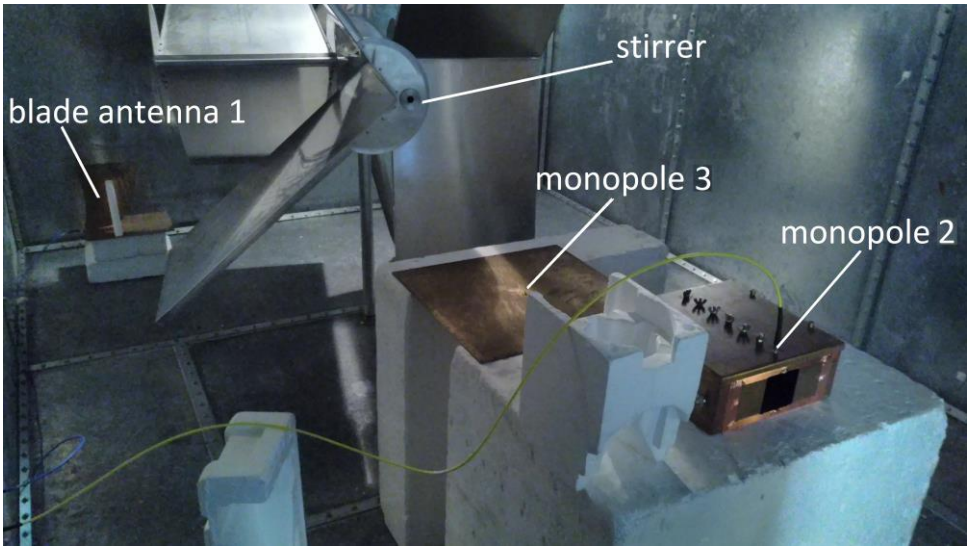

Figure 5. 23. Photograph of the validation measurements set up. The antennas 1, 2 and 3 are in accordance with those shown in figure 5.22.

5.7. Validation measurements

Beside the full wave simulations, the predictions of the diffusion model were also validated against physical measurements. The measurements were performed in the reverberation chamber at the University of York that has been presented in figure 3.3. Figure 5.22 and 5.23 show a diagram and a photograph of the measurement configuration. A blade antenna (antenna 1) served as the radiation source. A monopole with a length of 10mm was fitted

Figure 5. 24. Close up look at the monopole, which is antenna 3 shown in figures 5.22 and 5.23.

through each hole in the removable lid (see figures 5.3 and 5.5) of the enclosure in turn to measure the internal field. Another similar monopole (antenna 3), which can be seen in figure 5.24, was fitted at the centre of a 480mm×480mm metal plane to measure the external field.

The reverberation chamber was mode-tuned by a mechanical stirrer using 100 equally spaced positions over one complete rotation. A network analyser was used to collect the measurement data. First, we measured the S-parameters between antenna 1 and antenna 2; then between antenna 1 and antenna 3. The measurement range was 1GHz to 10GHz with 10001 equally spaced points. During the measurements, the unused holes on the enclosure lid were covered and the unused monopole (either antenna 2 or antenna 3) was attached to a 50Ω load.

The mismatch corrected insertion gain, IG, between antenna 1 and antenna 2 or 3 was calculated from the S-parameters [5]:

$$\mathrm{IG}_{1i} = \frac{\langle |S_{i1}|^2 \rangle}{(1-|\langle S_{11} \rangle|^2)(1-|\langle S_{ii} \rangle|^2)} \quad i = 2,3 \tag{5.100}$$

where S_{11}, S_{22} and S_{33} are the refection coefficients of antenna 1, 2 and 3 respectively. S_{21} and S_{31} are the transmission coefficients between the transmitting antenna 1 and receiving antennas 2 and 3. The power densities in the chamber and in the enclosure are proportional to the insertion gain:

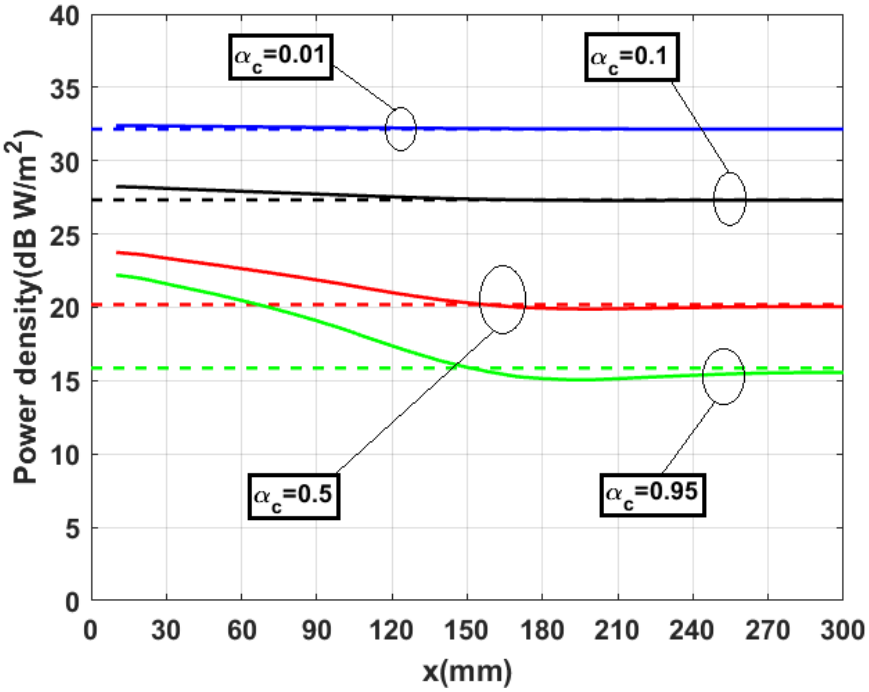

Figure 5. 25. Power density along the central line of the enclosure lid with the 75mm×75mm square aperture and 90mm×90mm×90mm absorbing cube as a function of the cube's absorption efficiency, comparing predictions of the diffusion model (solid lines) and the power balance model (dashed lines).

$$\frac{\mathrm{IG}_{13}}{\mathrm{IG}_{12}} = \frac{S_{ch}}{S_{en}} \tag{5.101}$$

where S_{ch} and S_{en} are the power densities in the reverberation chamber and in the enclosure respectively. S_{ch} can be set as any value in order to in accordance with that in the diffusion model and the full wave simulations.

5.8. Results and discussions

5.8.1. Comparison between the PWB method and diffusion model

In order to show the limitation of the power balance method, we built a diffusion model of the enclosure with the 75mm×75mm square aperture and the 90mm×90mm×90mm absorbing cube (see figures 5.12, 5.13 and 5.14). The radiated power, *P* in formula (5.3), was set as 1W. Figure 5.25 shows the power density along the central line of the enclosure lid for different values of the cube's absorption efficiency, comparing the predictions of the power balance method and the diffusion model. It can be seen that the power balance method assumes a constant power density regardless of positions. This assumption is true when the cube's absorption efficiency is 0.01, which suggests this is a low loss case, where the power

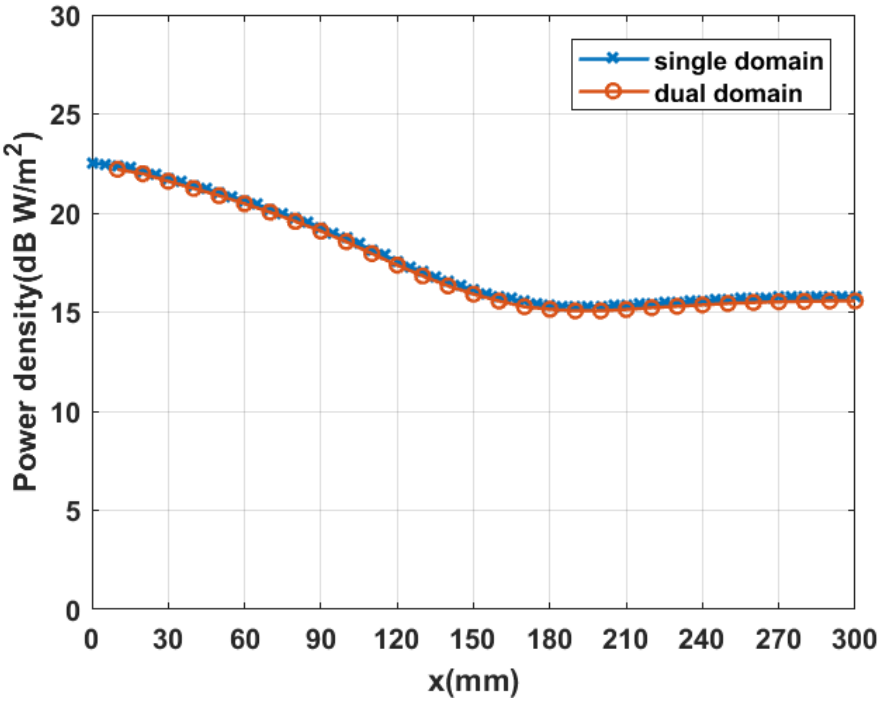

Figure 5. 26. Power density, normalized to 1W input power, along the central line of the enclosure lid with the 75mm×75mm square aperture and 90mm×90mm×90mm absorbing cube, comparing single and dual domain diffusion models.

balance method and the diffusion model lead to very similar results. As the absorption efficiency increases, the difference between the two methods becomes more and more obvious. This comparison indicates that the power balance method is unable to accurately predict the uniform field caused by high losses.

5.8.2. Comparison between the single and dual domain diffusion models

As has been mentioned, either single or dual domain models can be used for our test case. Figure 5.26 shows the power density along the central line of the enclosure lid with the 75mm×75mm square aperture and the 90mm×90mm×90mm absorbing cube, comparing the two models (see figures 5.10 and 5.11 for the single domain model; figures 5.12, 5.13 and 5.14 for the dual domain model). It can be noticed that they produce almost identical results. This suggests that the number of domain has little influence on the diffusion mode. Therefore, for simplicity, we will presented result obtained by the dual domain model for the rest of the thesis.

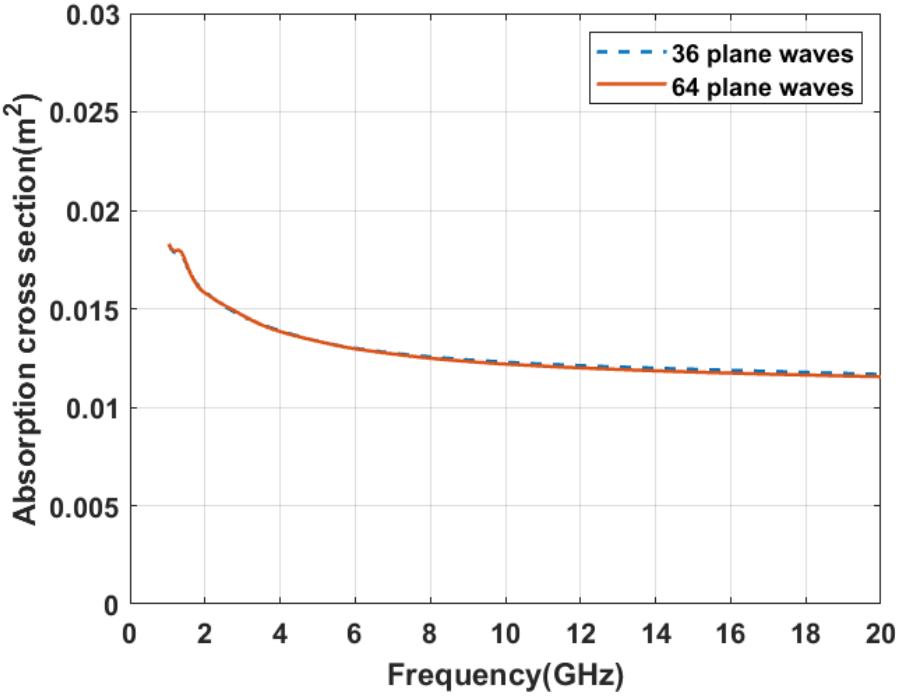

Figure 5. 27. Simulated absorption cross section of the 90mm×90mm×90mm cube, comparing the illumination of 36 and 64 plane waves.

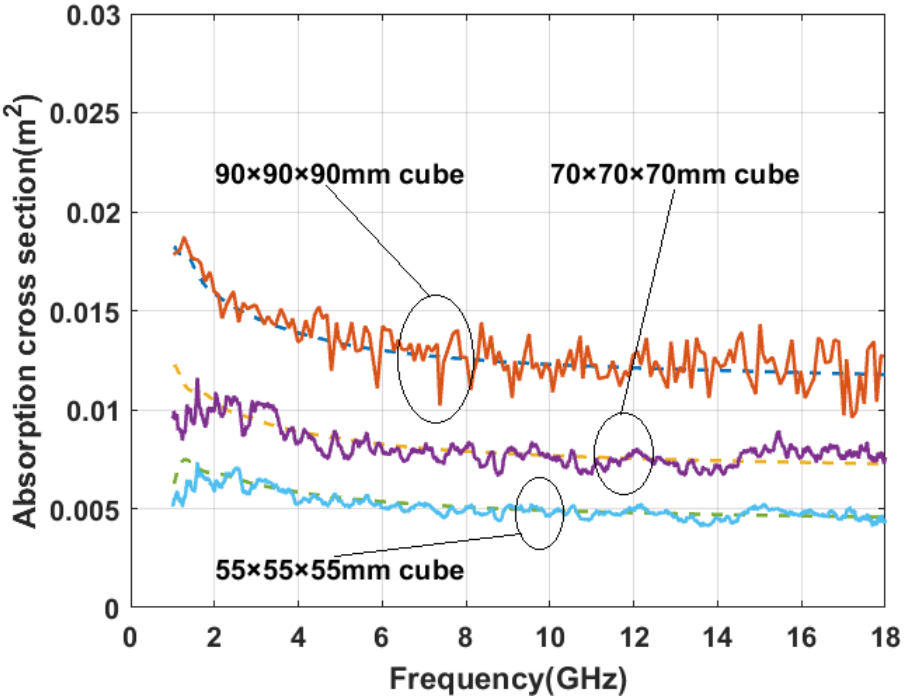

Figure 5. 28. Absorption cross sections of the three absorbing cubes, comparing full wave simulations (dashed lines) and measurement data (solid lines). The measurement were performed by X. Zhang [76].

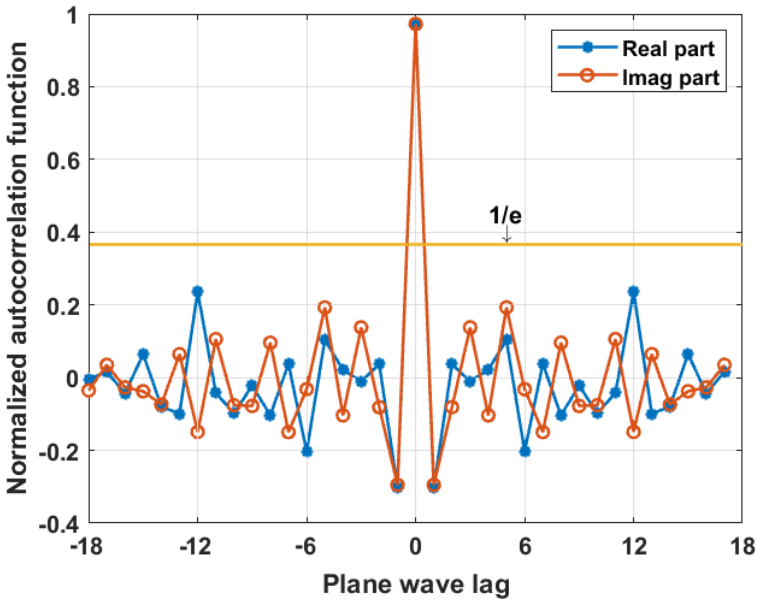

Figure 5. 29. Normalized autocorrelation function of Ex field component at point 3 at 5.5GHz in the enclosure with the 90mm×90mm×90mm cube and the 75mm×75mm square aperture.

5.8.3. The absorption cross sections of the cubes

Figure 5.8 shows the three cubes used in this thesis. In order to verify their full wave models, we compare the simulated absorption cross sections against measurement data. First we used 36 and 64 plane waves (see tables 1 and 2) to illuminate the 90mm×90mm×90mm cube and figure 5.27 shows the simulated absorption cross section. It can be seen that the two scenarios lead to almost identical results, which suggests that that 36 plane waves are sufficient to create a reverberant electromagnetic environment. Therefore, in order to save time, we used 36 plane waves in all the following simulations.

Figure 5.28 shows the simulated and measured absorption cross sections of the three cubes. The measurements were performed in the reverberation chamber at the University of York by X. Zhang [76]. It can be seen that simulations are in good agreement with the measurements. The absorption cross sections of the 90mm×90mm×90mm, 70mm×70mm×70mm and 55mm×55mm×55mm cubes are 0.012m^2, 0.008m^2 and 0.005m^2 respectively. The comparisons indicate that the full wave models of the cubes are reliable.

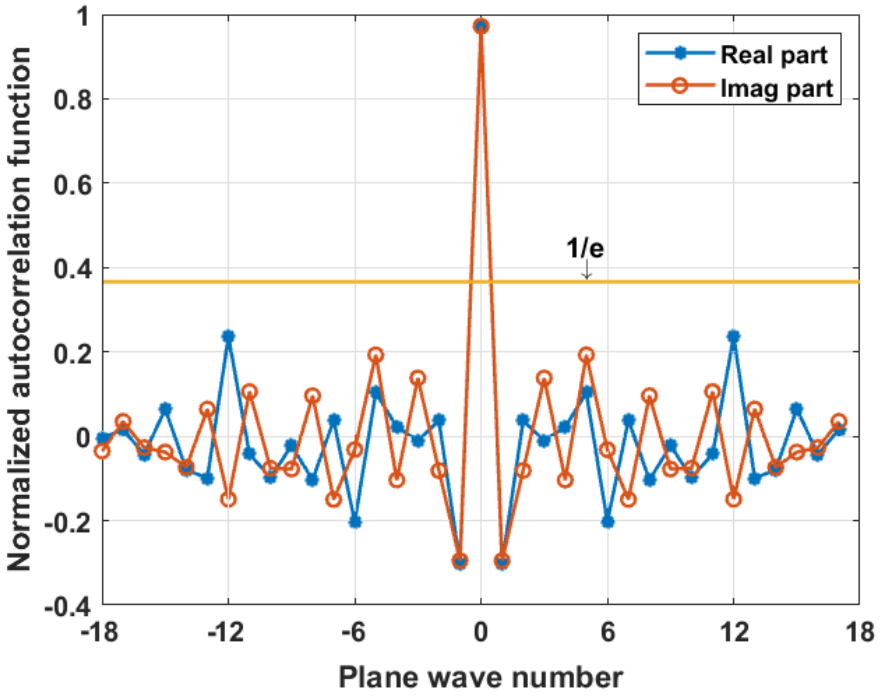

Figure 5. 30. Normalized autocorrelation function of Ey field component at point 3 at 5.5GHz in the enclosure with the 90mm×90mm×90mm cube and the 75mm×75mm square aperture.

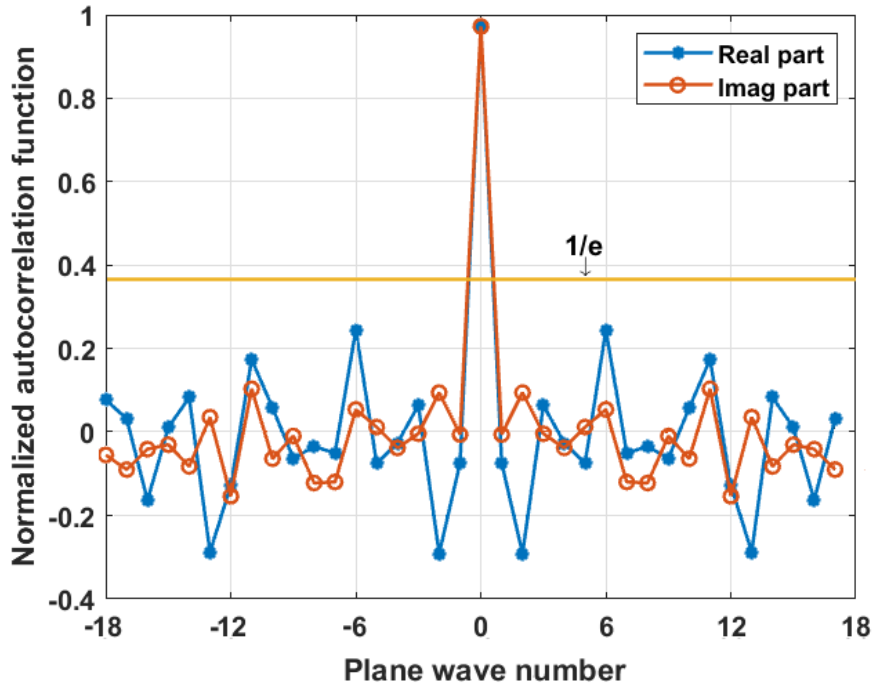

Figure 5. 31. Normalized autocorrelation function of Ez field component at point 3 at 5.5GHz in the enclosure with the 90mm×90mm×90mm cube and the 75mm×75mm square aperture.

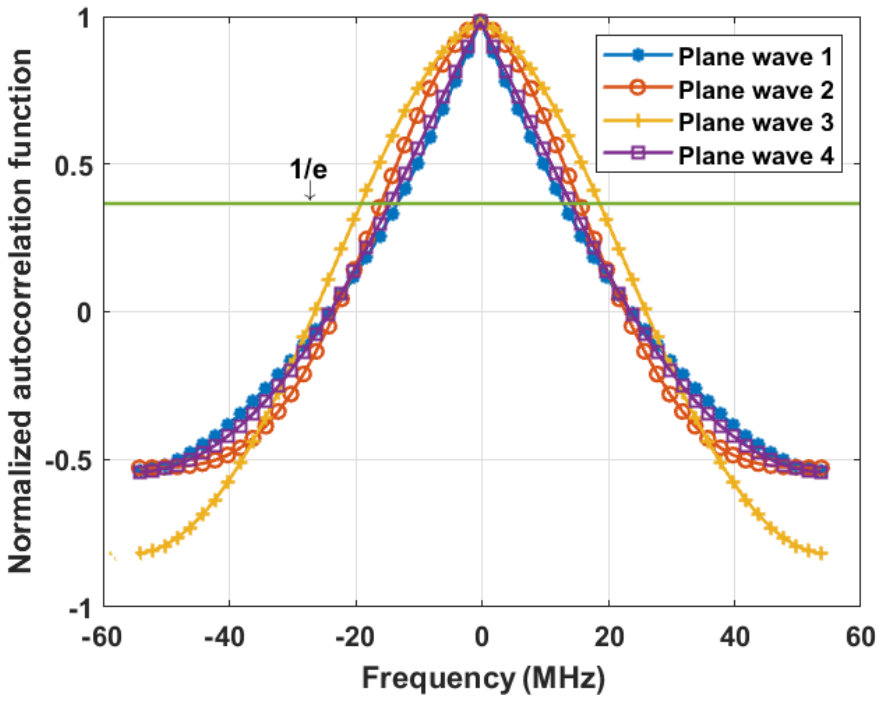

Figure 5. 32. Normalized ACF of the real part of the Ex field component at point 3 in the enclosure with the 90mm×90mm×90mm cube and 75mm×75mm square aperture. The four plane waves are randomly chosen and for each plane wave we pick 55 frequency points centred at 5.5GHz.

5.8.4. The field statistics of the full wave models

The use of the diffusion model requires the presence of a diffuse field and it is necessary to make sure that the field in the enclosure meets this condition. In both full wave simulations and measurements, autocorrelation function and probability density function are two key quantities to represent field statistics. According to Hill [43], in a reverberant electromagnetic environment, the field complies with normal distribution (also called Gaussian distribution) and this can be shown by plotting its probability density function (PDF). In order to plot PDF, there should be sufficient independent samples in the data and the number of independent samples can be estimated by autocorrelation function.

Figures 5.29, 5.30 and 5.31 show the normalized autocorrelation function (ACF) of the real and imaginary part of the electric field (which consists of Ex, Ey and Ez components) in the full wave model of the enclosure with the 90mm×90mm×90mm cube and the 75mm×75mm square aperture. We used the aforementioned 36 plane waves to illuminate the enclosure. The autocorrelation function was calculated by using formulas (3.8) and (3.9). The full wave simulation was performed from 1GHz to 10GHz and there are 5001 equally spaced points.

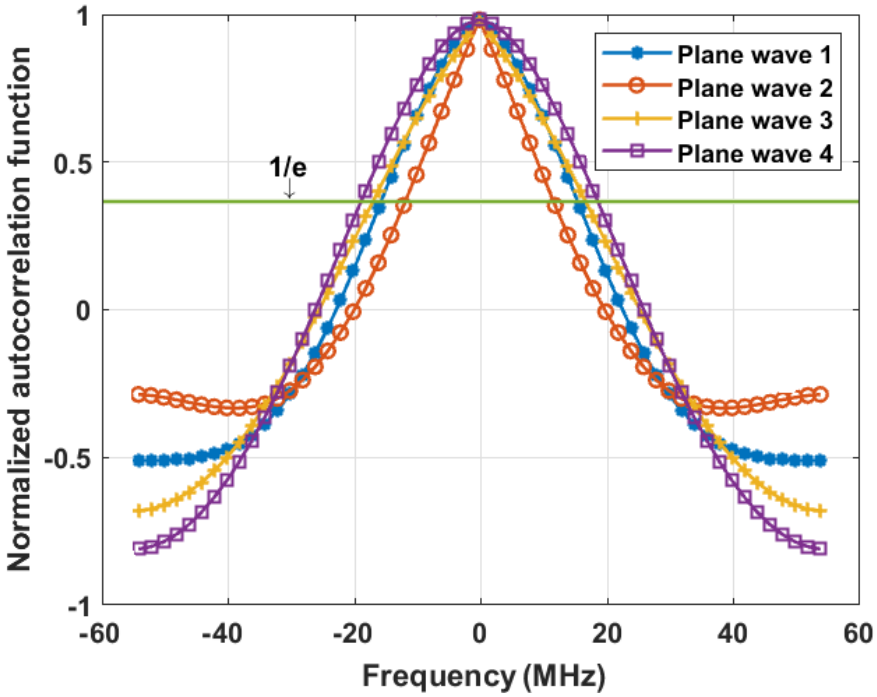

Figure 5. 33. Normalized ACF of the imaginary part of the Ex field component at point 3 in the enclosure with the 90mm cube and 75mm square aperture. The four plane waves are randomly chosen and for each wave, we pick 55 frequency points centred at 5.5GHz.

There are several probes in the model (see figure 5.16) and for simplicity, we only show the ACF at probe 3 at 5.5GHz. It can be seen that for all the three field components, there is only one correlated sample. According to formula 3.6, all the 36 samples are independent, which suggests that the 36 plane waves we use are independent of each other.

Only 36 independent samples are not sufficient to plot probability density function. We need to include some results from frequency points that are close to 5.5GHz. Therefore, we chose a frequency band of 100 MHz that is centred at 5.5GHz. The band contains 55 points. We randomly picked four plane waves and calculated the ACF of the 55 points within the 100MHz frequency band. Figures 5.32 and 5.33 show the ACF of the real and imaginary part of the Ex field component at point 3 in the enclosure with the 90mm×90mm×90mm cube and 75mm×75mm square aperture. It can be seen that the Ex field components are highly correlated, which means that even if we include the 55 points in the vicinity of 5.5GHz, we will not get more independent samples. The Ey and Ez field components are also highly correlated and for simplicity, we do not present them in this thesis.

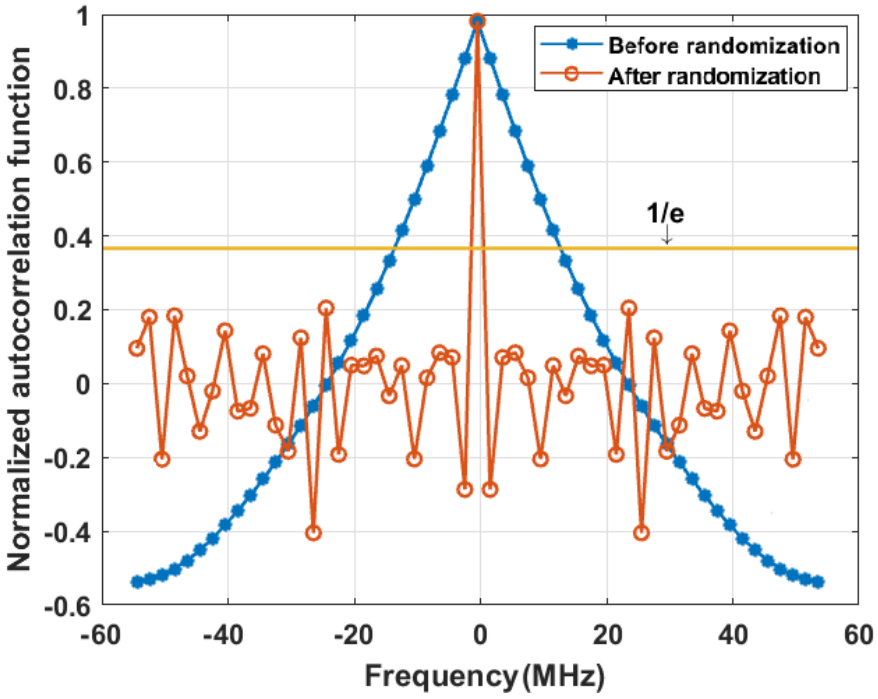

Figure 5. 34. Normalized ACF of the real part of the Ex field component of plane wave 1 at point 3 in the enclosure with the 90mm cube and 75mm square aperture, comparing the ACF before and after randomization. The frequency points centred at 5.5GHz.

In order to get adequate independent samples, we randomized the phase of the field components. As can be seen form figures 5.29 to 5.33, in CST, the field components are complex numbers and they can be expressed as $E=E_0e^{j\vartheta}$, where E_0 is the amplitude and ϑ is the phase angle. The randomization is achieved by multiplying the original field with a random angle:

$$E_r = E_0 e^{j\theta} \cdot e^{j\theta_r} \tag{5.102}$$

where ϑ_r is a random angle between 0 and 2π. In Matlab, we use the command 2π×rand(M,N) to generate the angles, where the function rand(M,N) returns M×N different random numbers between 0 and 1. As an example, we show the real part of Ex field component of plane wave 1 at point 3 in the enclosure with the 90mm×90mm×90mm cube and 75mm×75mm square aperture in figure 5.34. It can be seen that after the randomization, all 55 points within the bandwidth of 100MHz centred at 5.5GHz become independent. Applying the same method to all 36 plane waves, we now have 55×36=1980 independent samples, which we believe is sufficient to plot the probability density function.

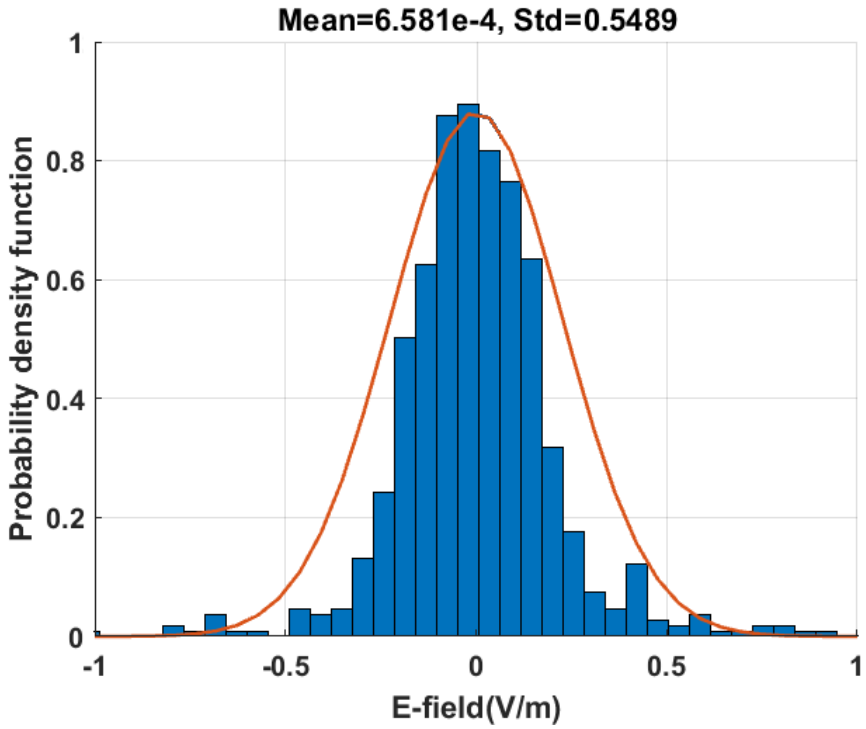

Figure 5. 35. Probability density function of the real part of Ex field component at 5.5GHz at point 3 in the enclosure with the 90mm×90mm×90mm cube and 75mm×75mm square aperture.

We plot the probability density function by using histogram in Matlab. First, we obtain the length of each bin (this is the number of samples), then divide them by the total number of samples to get the probability. Finally, we divide the probability by the width of each bin to get the probability density.

Figures 5.35-5.40 show the probability density function of the real and imaginary part of Ex, Ey and Ez field component at 5.5GHz at point 3 (see figure 5.16) in the enclosure with the 90mm×90mm×90mm cube and 75mm×75mm square aperture. It can be seen that all field components comply with normal distribution with means very close to zero.

We applied the same randomization process to the field in the enclosure with the r=6mm circular aperture and figures 5.41-5.46 show the results. Again, for simplicity we only present the PDF of the field at point 3 at 5.5GHz. The field components at point 3 comply with normal distribution. Therefore, we can conclude that the randomized field in the CST model of the enclosure is reverberant for both scenarios.

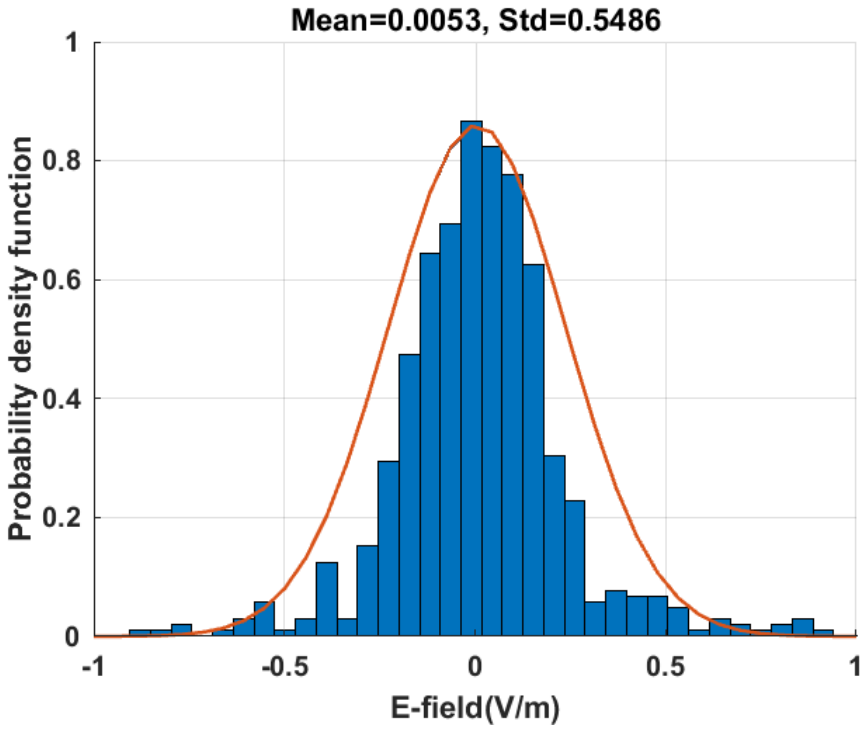

Figure 5. 36. Probability density function of the imaginary part of Ex field component at 5.5GHz at point 3 in the enclosure with the 90mm×90mm×90mm cube and 75mm×75mm square aperture.

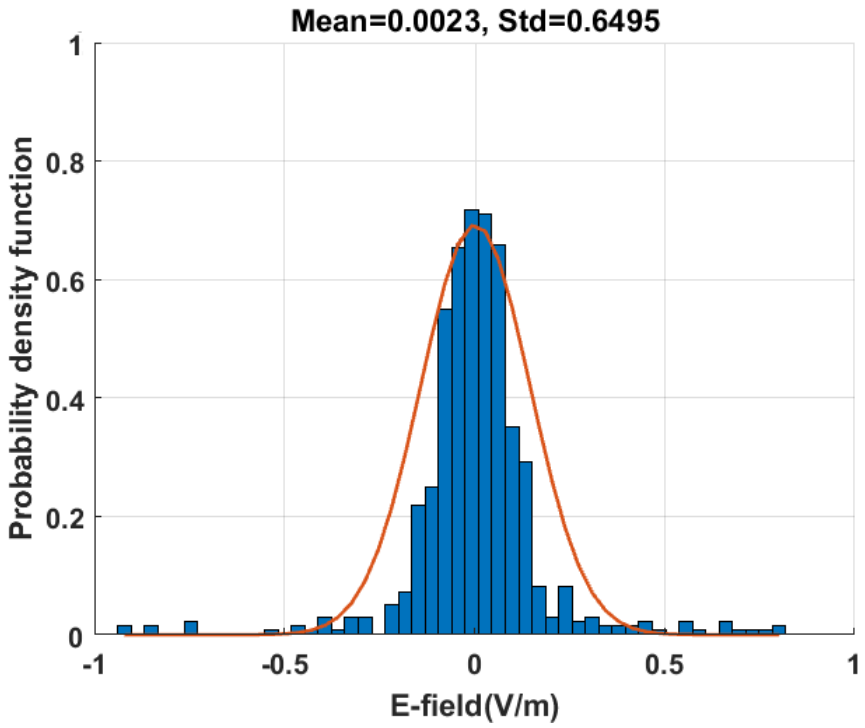

Figure 5. 37. Probability density function of the real part of Ey field component at 5.5GHz at point 3 in the enclosure with the 90mm×90mm×90mm cube and 75mm×75mm square aperture.

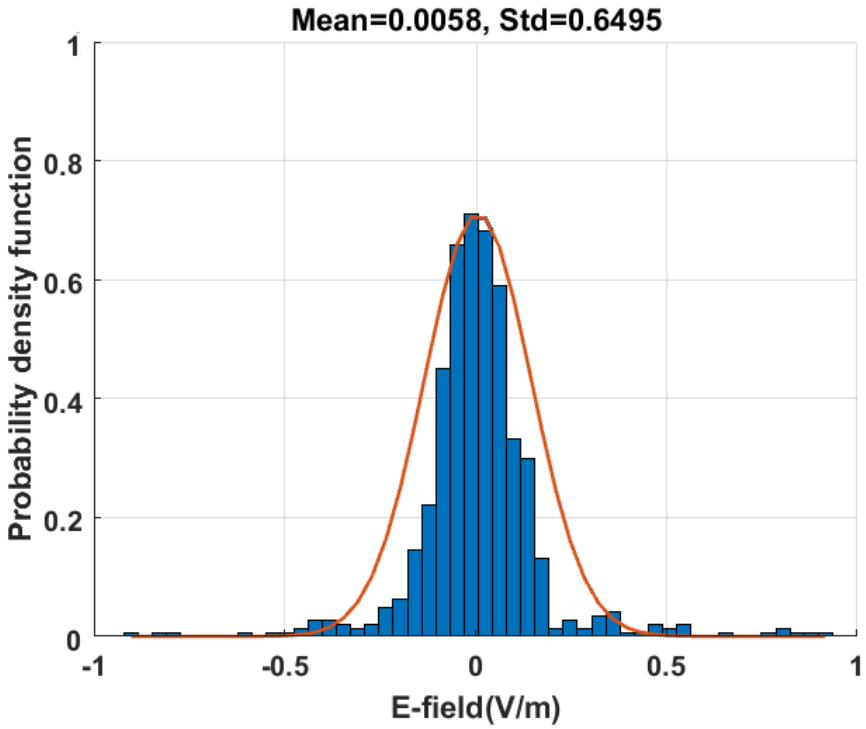

Figure 5. 38. Probability density function of the imaginary part of Ey field component at 5.5GHz at point 3 in the enclosure with the 90mm×90mm×90mm cube and 75mm×75mm square aperture.

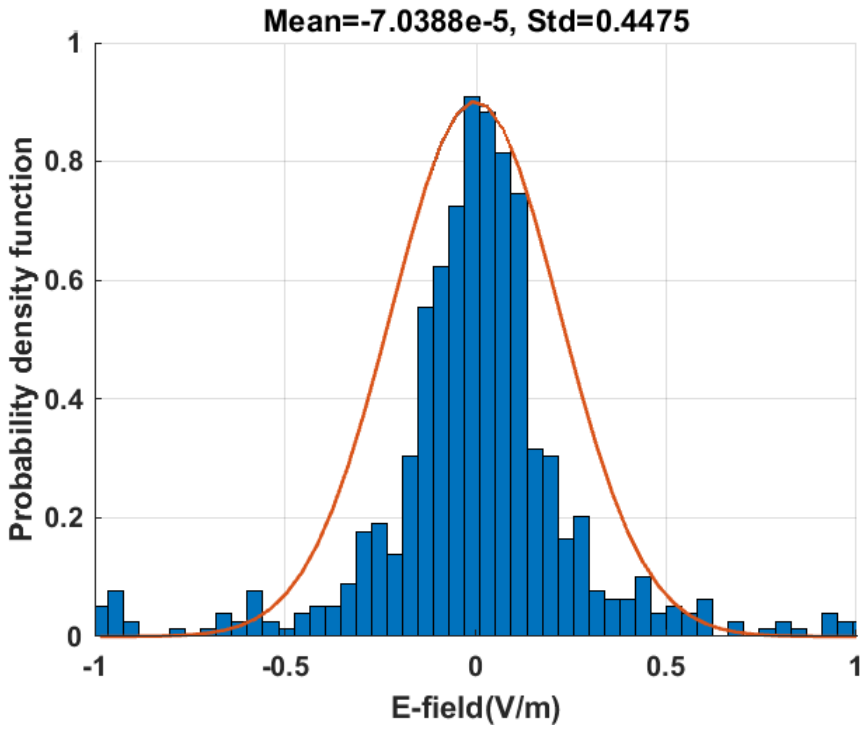

Figure 5. 39. Probability density function of the real part of Ez field component at 5.5GHz at point 3 in the enclosure with the 90mm×90mm×90mm cube and 75mm×75mm square aperture.

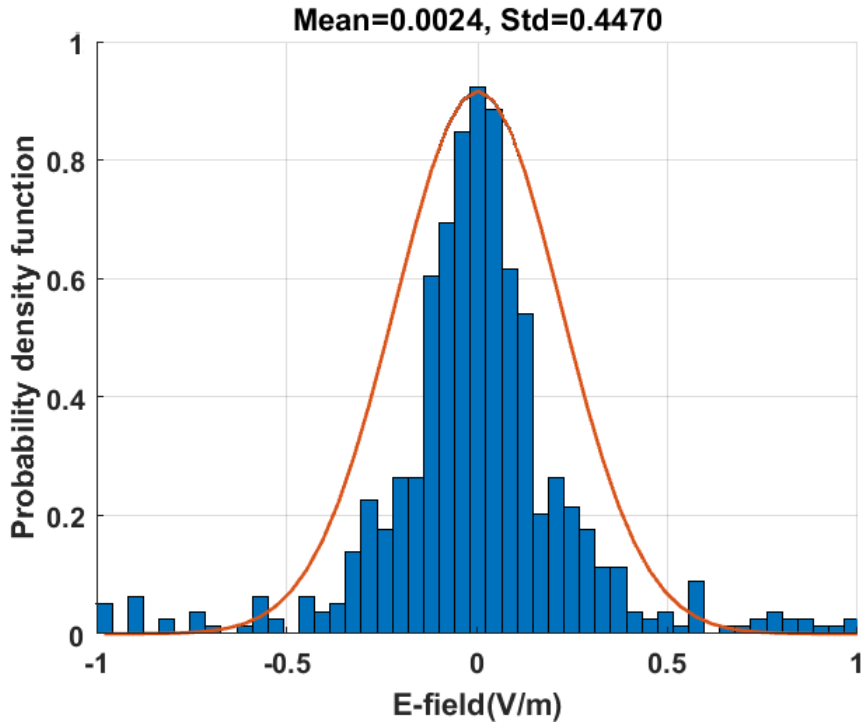

Figure 5. 40. Probability density function of the imaginary part of Ez field component at 5.5GHz at point 3 in the enclosure with the 90mm×90mm×90mm cube and 75mm×75mm square aperture.

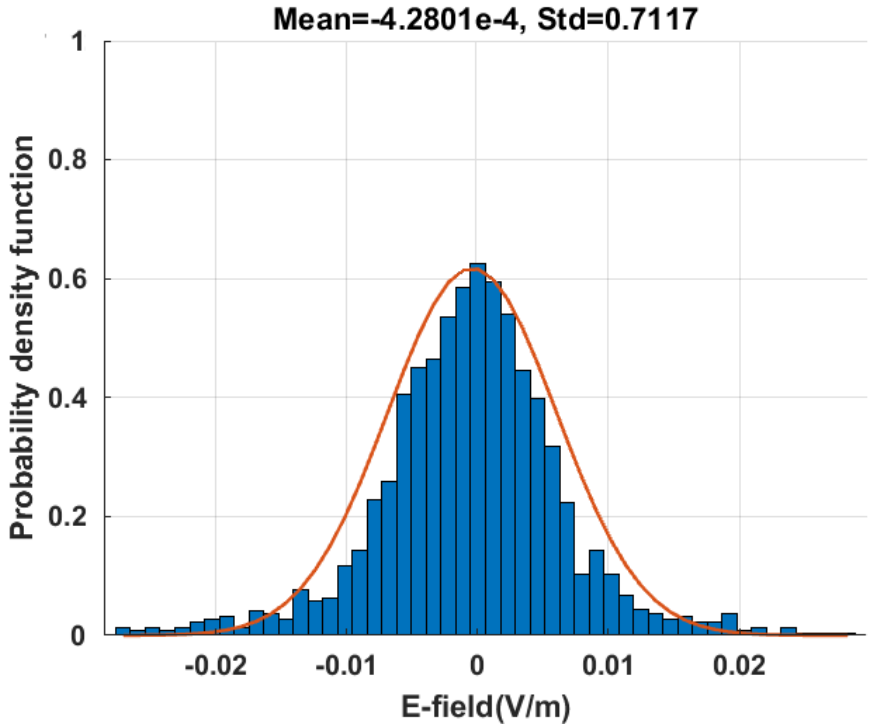

Figure 5. 41. Probability density function of the real part of Ex field component at 5.5GHz at point 3 in the enclosure with the 90mm×90mm×90mm cube and *r*=6mm circular aperture.

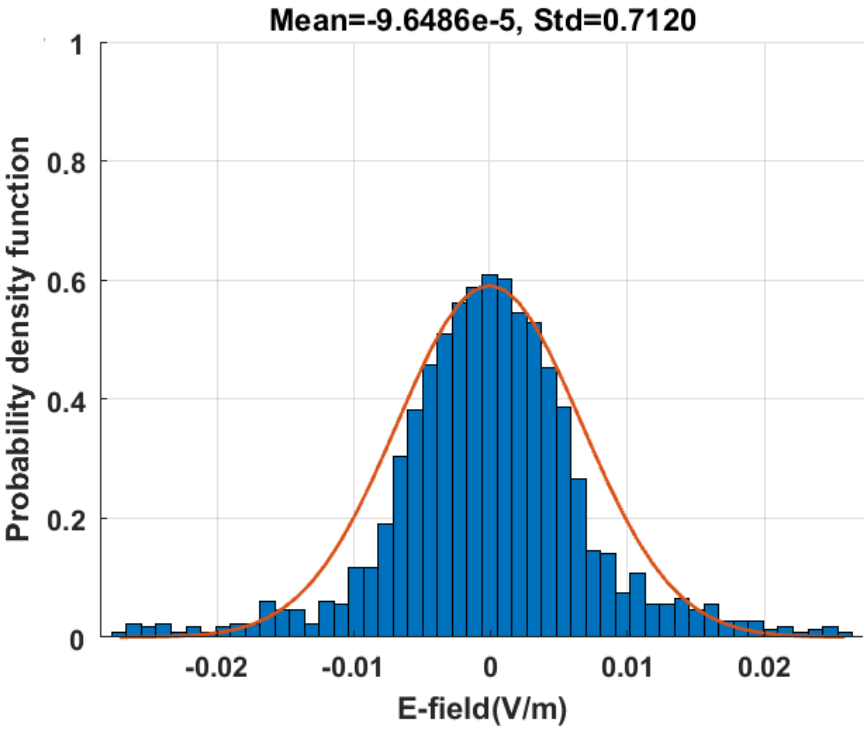

Figure 5. 42. Probability density function of the imaginary part of Ex field component at 5.5GHz at point 3 in the enclosure with the 90mm×90mm×90mm cube and *r*=6mm circular aperture.

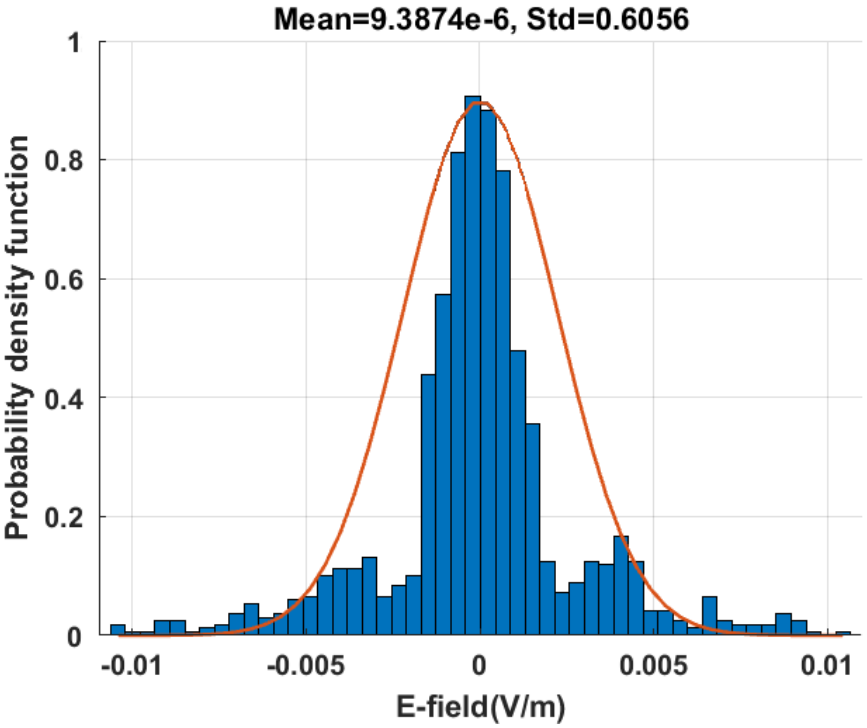

Figure 5. 43. Probability density function of the real part of Ey field component at 5.5GHz at point 3 in the enclosure with the 90mm×90mm×90mm cube and *r*=6mm circular aperture.

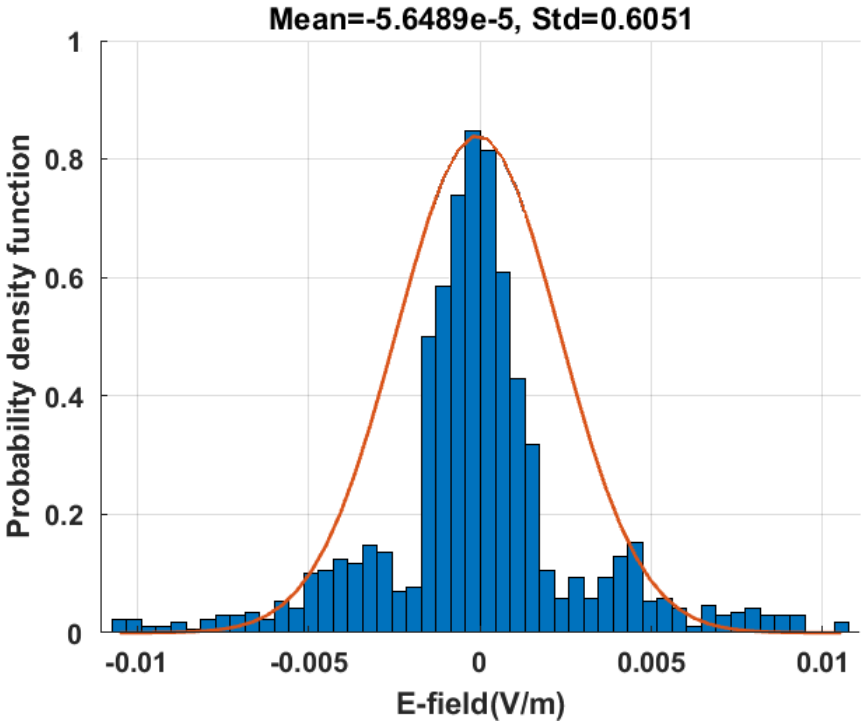

Figure 5. 44. Probability density function of the imaginary part of Ey field component at 5.5GHz at point 3 in the enclosure with the 90mm×90mm×90mm cube and *r*=6mm circular aperture.

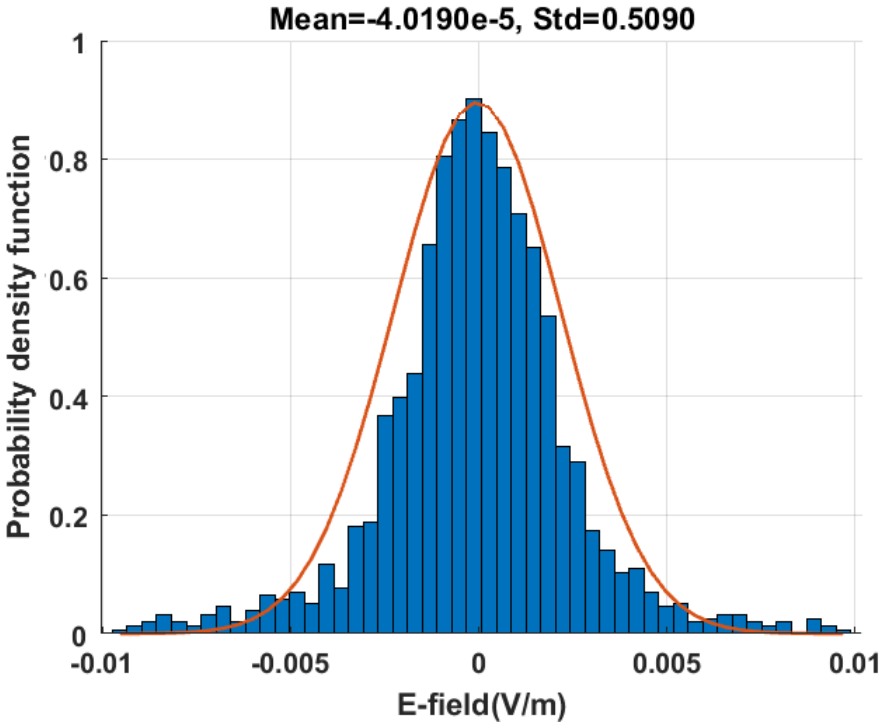

Figure 5. 45. Probability density function of the real part of Ez field component at 5.5GHz at point 3 in the enclosure with the 90mm×90mm×90mm cube and *r*=6mm circular aperture.

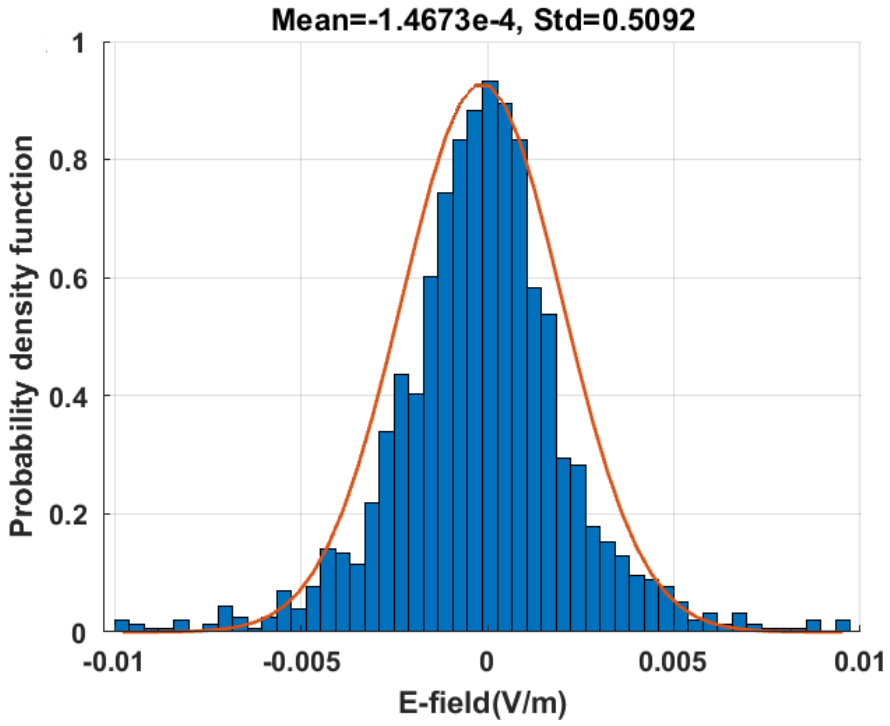

Figure 5. 46. Probability density function of the imaginary part of Ez field component at 5.5GHz at point 3 in the enclosure with the 90mm×90mm×90mm cube and *r*=6mm circular aperture.

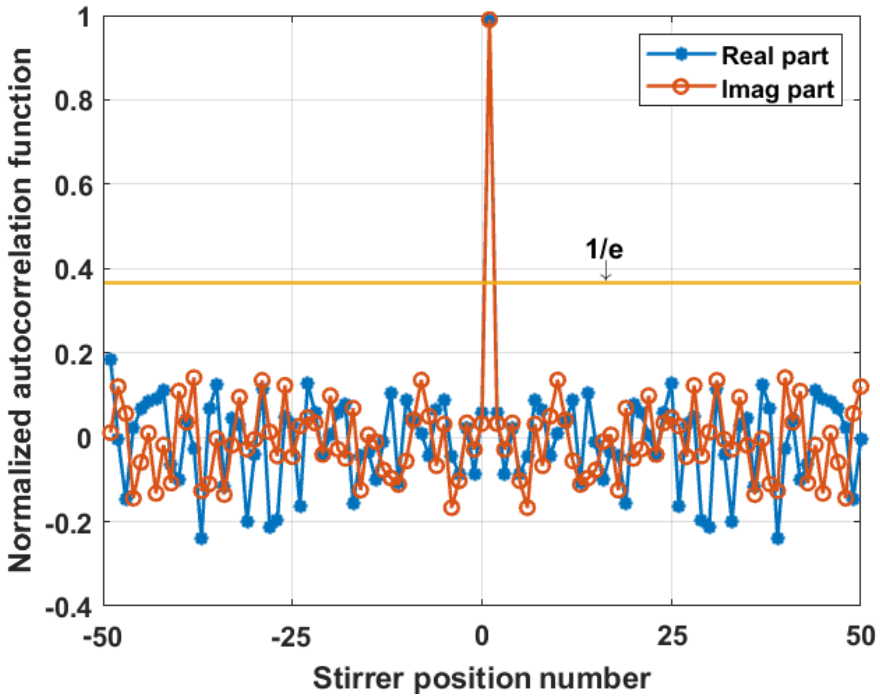

Figure 5. 47. Normalized autocorrelation function of S_{21} at point 2 at 5.5GHz in the enclosure with the 90mm×90mm×90mm cube and 75mm×75mm square aperture.

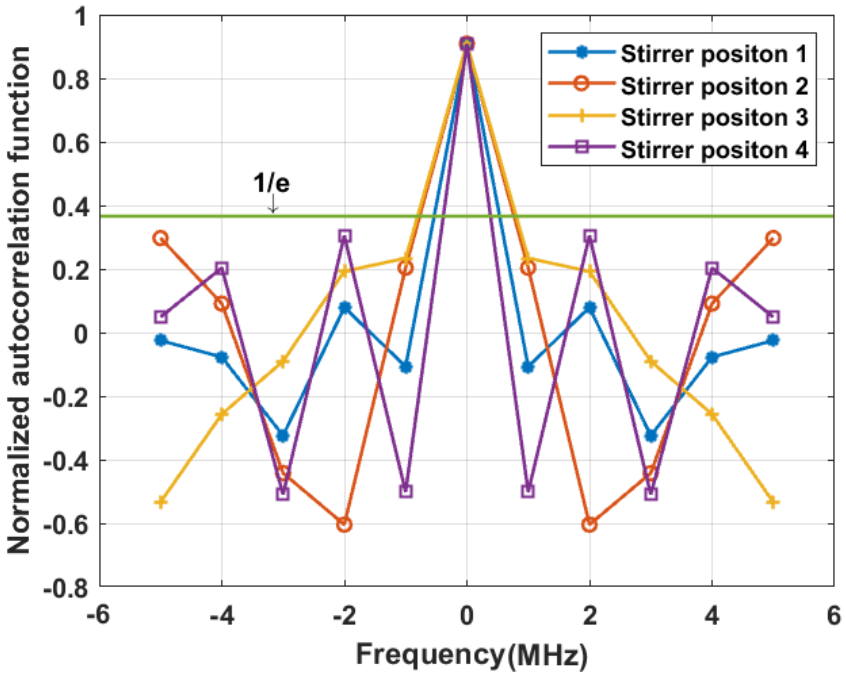

Figure 5. 48 Normalized ACF of the real part of S_{21} at point 2 at 5.5GHz in the enclosure with the 90mm×90mm×90mm cube and 75mm×75mm square aperture. The four stirrer positions were randomly chosen and for each position we picked a frequency band of 10MHz that is centred at 5.5GHz. The band contains 11 points.

5.8.5. The field statistics of the measurements

In this section, we present the statistics of the field in the physical measurements. In the measurements, the antennas do not record electric field like the probes in the full wave model. Instead, the network analyser collected S-parameters. Hence, we calculated the autocorrelation function and probability density function of S_{21}, which is the transmission coefficient between the transmitting antenna and the receiving antenna (see figures 5.22 and 5.23). There are seven measurement positions on the lid of the enclosure (see figure 5.5), we only present the field statistics at point 2 for brevity.

Figure 5.47 shows the normalized autocorrelation function of S_{21} at point 2 at 5.5GHz in the enclosure with the 90mm×90mm×90mm cube and the 75mm×75mm square aperture. It can be seen that for both real and imaginary part, all 100 samples are independent of each other, which suggests that the 100 stirrer positions are independent. We then picked four stirrer positions and for each position, we chose a frequency band of 20MHz, which contains 11 points.

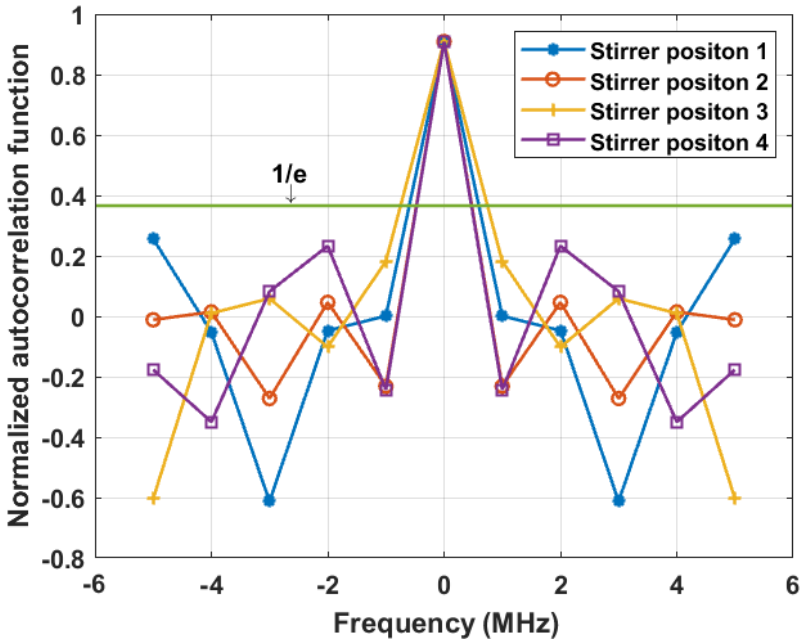

Figure 5. 49. Normalized ACF of the imaginary part of S_{21} at point 2 at 5.5GHz in the enclosure with the 90mm×90mm×90mm cube and 75mm×75mm square aperture. The four stirrer positions were randomly chosen and for each position we picked a frequency band of 10MHz that is centred at 5.5GHz. The band contains 11 points.

Figures 5.48 and 5.49 show the normalized autocorrelation of real and imaginary part of the 11 points respectively. It can be seen that they are independent. Therefore, we do not need to use the randomization process as we did to the data of full wave simulations.

Figures 5.50 and 5.51 show the probability density function of real and imaginary part of S_{21} at 5.5GHz at point 2 in the enclosure with the 90mm×90mm×90mm cube and the 75mm×75mm square aperture. Figure 5.52 and 5.53 show the probability density function at the same point at the same frequency in the enclosure with the same cube and the *r*=6mm circular aperture. There are totally 11×100=1100 samples in each figure. It can be seen that for both scenarios, the S_{21} complies with normal distribution with a mean of nearly zero. This indicates that at 5.5GHz, the field in the enclosure is sufficiently reverberant.

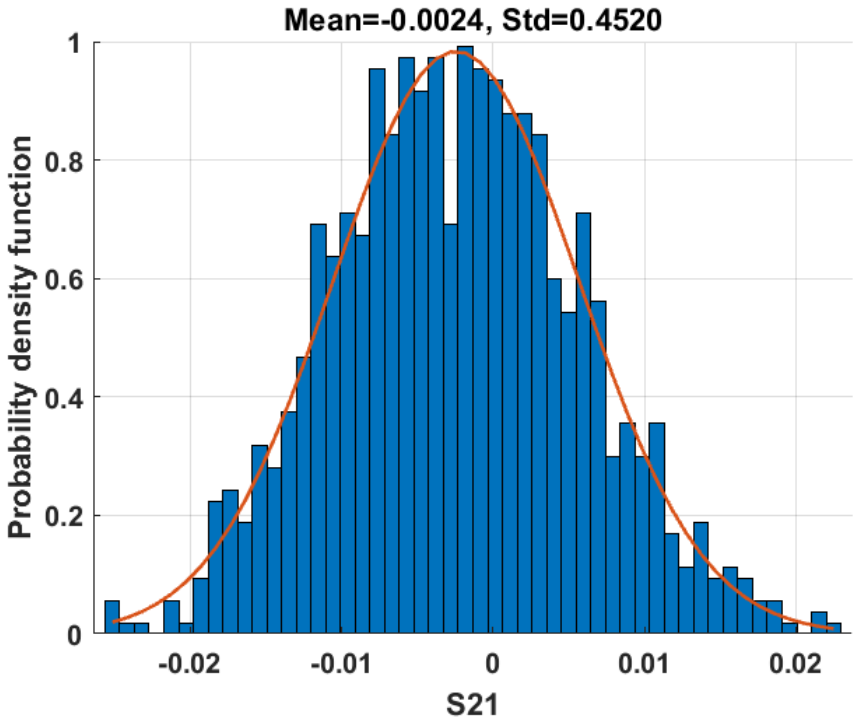

Figure 5. 50. Probability density function of the real part of S_{21} at 5.5GHz at point 2 in the enclosure with the 90mm×90mm×90mm cube and 75mm×75mm square aperture.

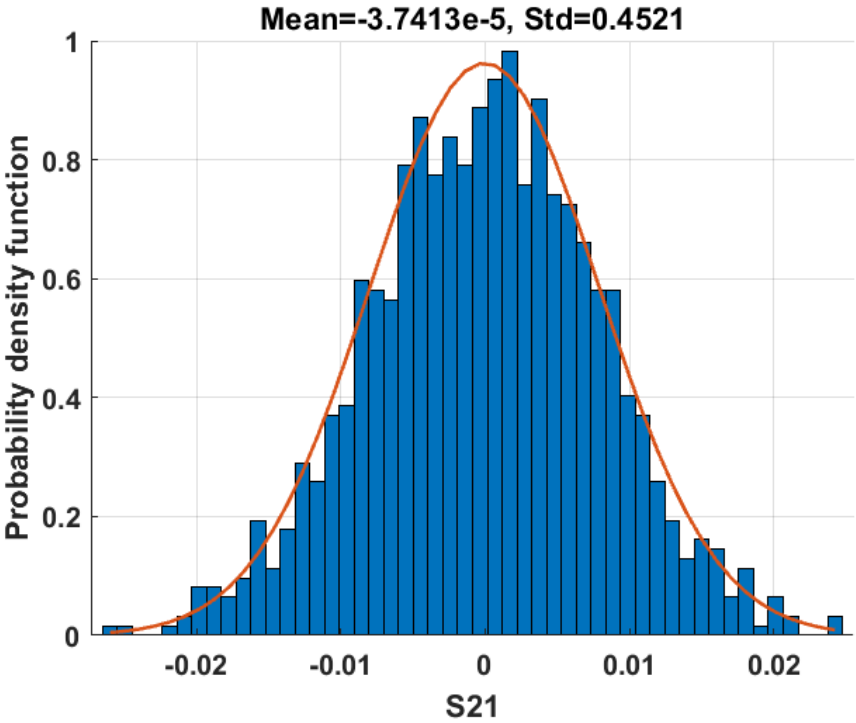

Figure 5. 51. Probability density function of the imaginary part of S_{21} at 5.5GHz at point 2 in the enclosure with the 90mm×90mm×90mm cube and 75mm×75mm square aperture.

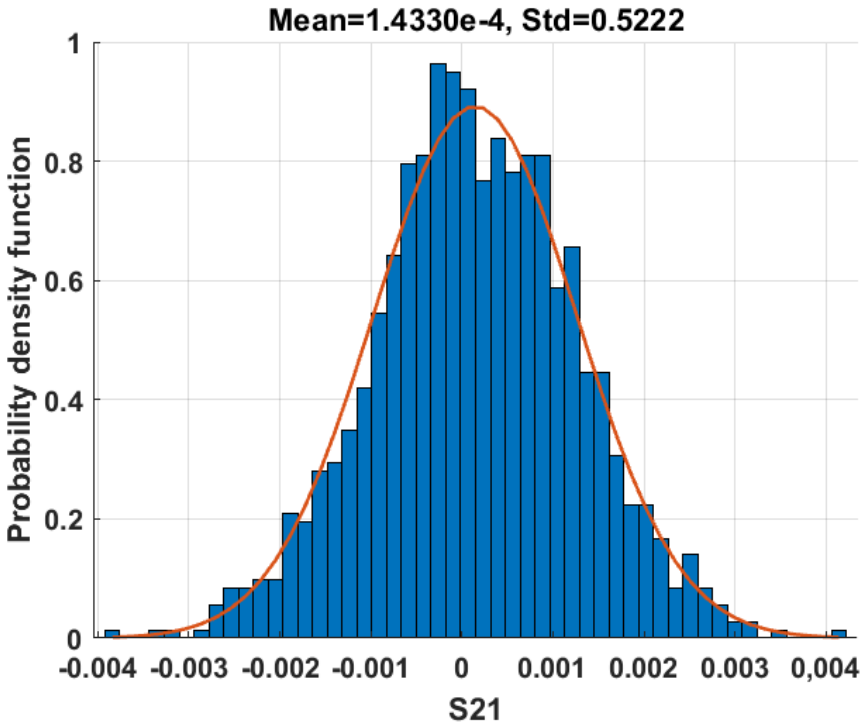

Figure 5. 52. Probability density function of the real part of S21 at 5.5GHz at point 2 in the enclosure with the 90mm×90mm×90mm cube and *r*=6mm circular aperture.

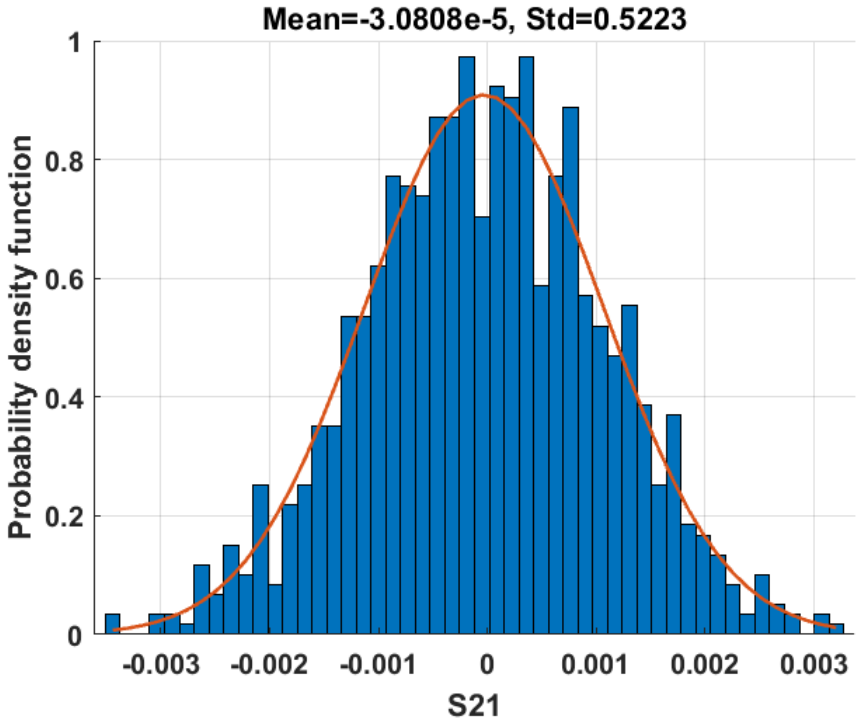

Figure 5. 53. Probability density function of the imaginary part of S_{21} at 5.5GHz at point 2 in the enclosure with the 90mm×90mm×90mm cube and *r*=6mm circular aperture.

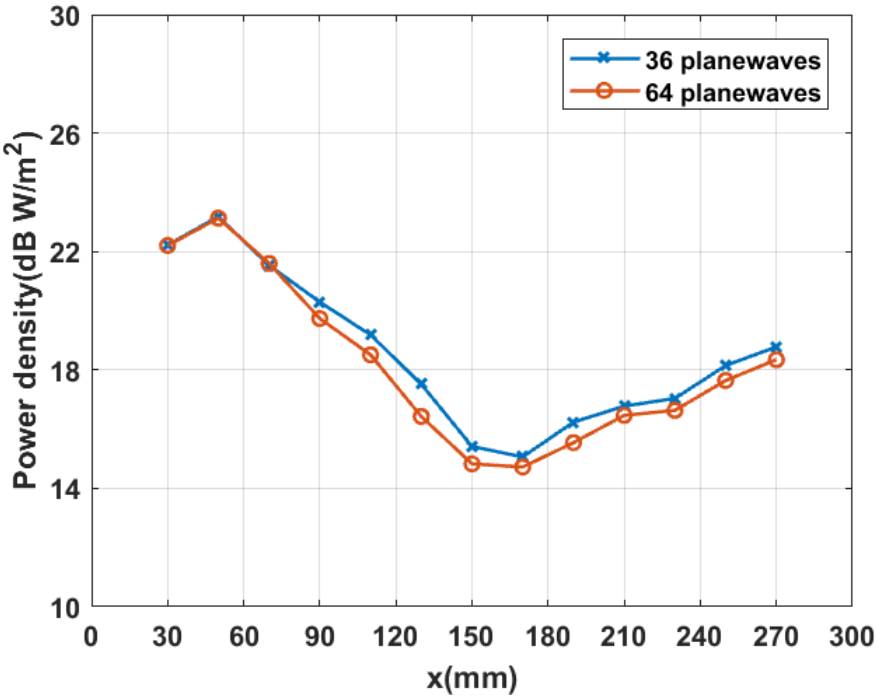

Figure 5. 54. Simulated power density, normalized to 1W input power, along the central line of the lid of the enclosure with the 90mm×90mm×90mm cube and 75mm×75mm square aperture at 5.5GHz, comparing different number of plane waves.

5.8.6. Power density in the enclosure

In the previous two sections, we have demonstrated that for both full wave simulation and physical measurement, the field in the enclosure is reverberant. In this section, we provide the power density in the enclosure, comparing the diffusion model, full wave simulation and measurement. It should be noted that the results obtained by full wave simulation and measurement were normalized to 1W input power in order to compare with that obtained by the diffusion model.

Figure 5.54 shows the simulated power density along the central line of the lid of the enclosure loaded with the 90mm×90mm×90mm cube and the 75mm×75mm square aperture at 5.5GHz. We used 36 and 64 plane waves (see figures 5.20 and 5.21) to illuminate the enclosure respectively. It can be seen that the test scenarios produced very similar results with less than 1dB difference. This shows again that 36 plane waves detailed in section 5.6.2 are sufficient to create a reverberant electromagnetic environment. In addition, it can be noticed that the power density is apparently not uniform throughout the enclosure.

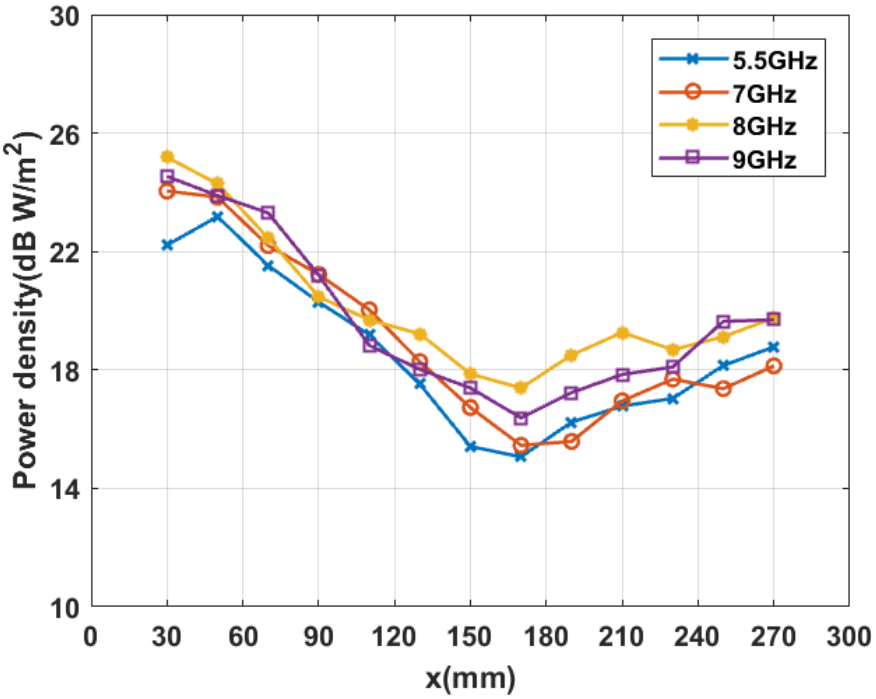

Figure 5. 55. Simulated power density, normalized to 1W input power, along the central line of the lid of the enclosure with the 90mm×90mm×90mm cube and 75mm×75mm square aperture at different frequencies.

Figure 5.55 shows the simulated power density along the central line of the lid of the enclosure loaded with the 90mm×90mm×90mm cube and the 75mm×75mm square aperture at 5.5GHz, 7GHz, 8GHz and 9GHz respectively. We can see that the results are generally in agreement with less than 3dB difference. This suggests that in the steady state, the field in the enclosure does not change a lot as frequency increases. Therefore, for brevity, in the following results we only show the power density at 5.5GHz.

Figures 5.56, 5.57 and 5.58 show the power density along the central line of the lid of the enclosure loaded with different cubes (see figure 5.8) and the 75mm×75mm square aperture at 5.5GHz, comparing the predictions of the diffusion mode, full wave simulation and measurement. It can be seen that the results obtained by the diffusion model agree with those by full wave simulation and measurement with less than 3dB difference. When the enclosure is loaded with the 90mm×90mm×90mm cube, the power density drops rapidly towards the centre and reaches the minimum value at around x=150mm. This is because the cube is at the centre (see figure 5.7). As the cube becomes smaller, this drop becomes less obvious.

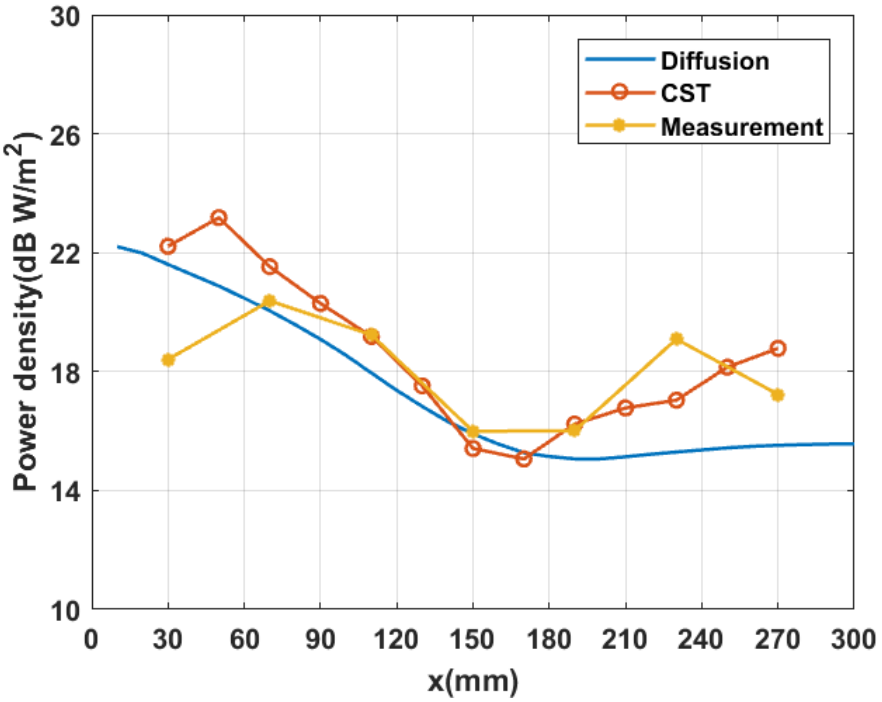

Figure 5. 56. Power density, normalized to 1W input power, along the central line of the lid of the enclosure with the 90mm×90mm×90mm cube and 75mm×75mm square aperture at 5.5GHz, comparing diffusion model, full wave simulation and measurement.

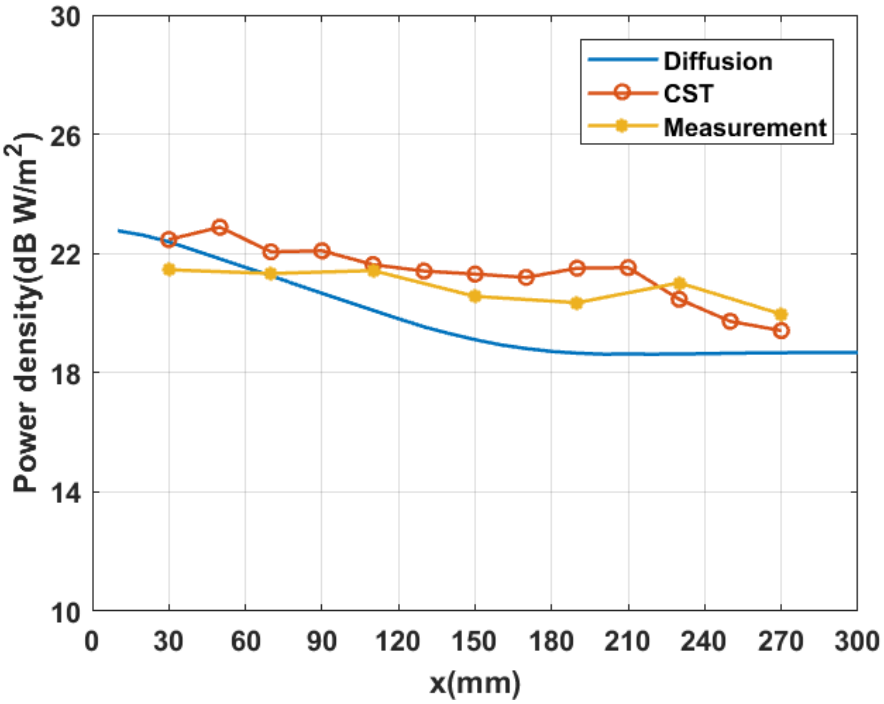

Figure 5. 57. Power density, normalized to 1W input power, along the central line of the lid of the enclosure with the 70mm×70mm×70mm cube and 75mm×75mm square aperture at 5.5GHz, comparing diffusion model, full wave simulation and measurement.

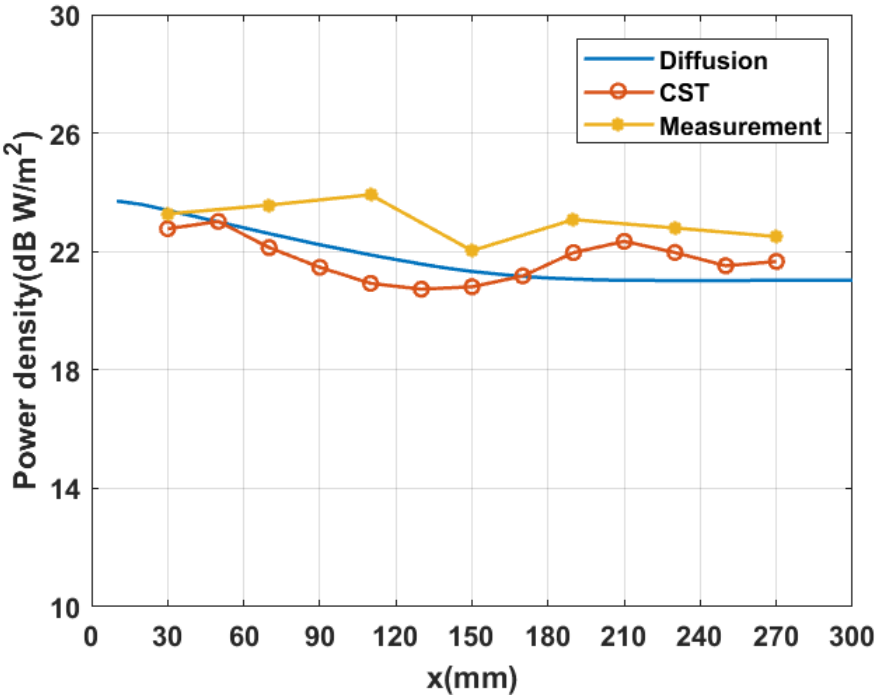

Figure 5. 58. Power density, normalized to 1W input power, along the central line of the lid of the enclosure with the 55mm×55mm×55mm cube and 75mm×75mm square aperture at 5.5GHz, comparing diffusion model, full wave simulation and measurement.

As has been mentioned, the 75mm×75mm square aperture has a constant transmission cross section from 1GHz to 10GHz and the *r*=6mm circular aperture has a frequency-dependent transmission cross section below 10GHz. For the enclosure with the circular aperture, we are interested in how the power density changes with frequency. Therefore, we picked point 2 (see figure 5.5) and plotted the power density as a function of frequency in figure 5.59. For simplicity, we only present the results when the enclosure is loaded with 90mm×90mm×90mm cube. It can be seen that the power density increases with frequency. This is because the transmission cross section of the r=6mm aperture increases with frequency (see figure 5.7). The diffusion model is in good agreement with the full wave simulation. The measurement, however, only shows good agreement above 5GHz.

In order to investigate the cause of this discrepancy, we covered the aperture and measured the power density again by using the method detailed in section 5.7. In this way, we obtained the noise floor of the measurement. The result is presented in figure 5.59 with the legend “no aperture”. It can be seen that the noise floor is less than -20dB W/m^2 and the measured power

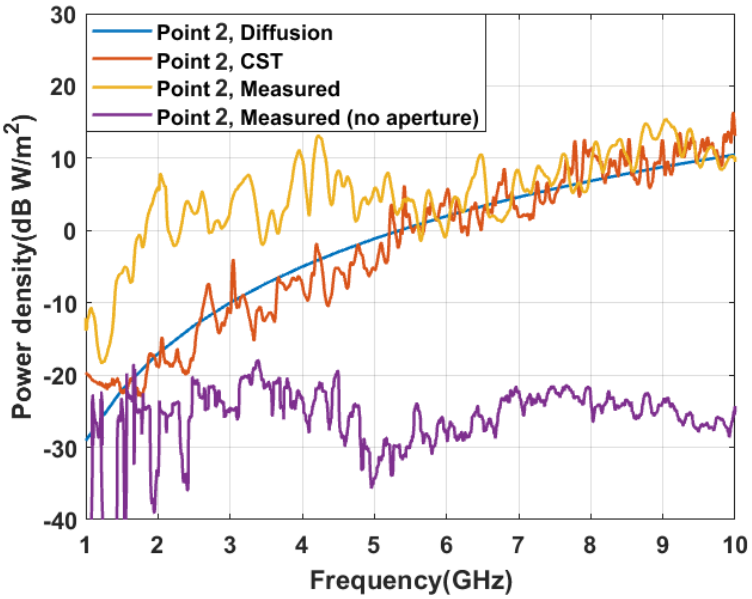

Figure 5. 59. Power density, normalized to 1W input power, along the central line of the lid of the enclosure with the 90mm×90mm×90mm cube and *r*=6mm circular aperture at 5.5GHz, comparing diffusion model, full wave simulation and measurement.

density is well above it. Hence, we can rule out the effect of the leakage through the seam and joint of the enclosure on the measurement.

Another possible reason for the discrepancy is that below 5GHz, the field in the enclosure is not sufficiently reverberant. We calculated the probability density function of S_{21} of point 2 at 2GHz and 3GHz respectively. The results are presented in figures 5.60-5.63. It can be seen that at 2GHz and 3GHz, the S_{21} at point 2 complies with a normal distribution, which indicates that the field in the enclosure is reverberant at these frequencies. Currently we are still uncertain about the cause of the difference between measurement and full wave simulation below 5GHz.

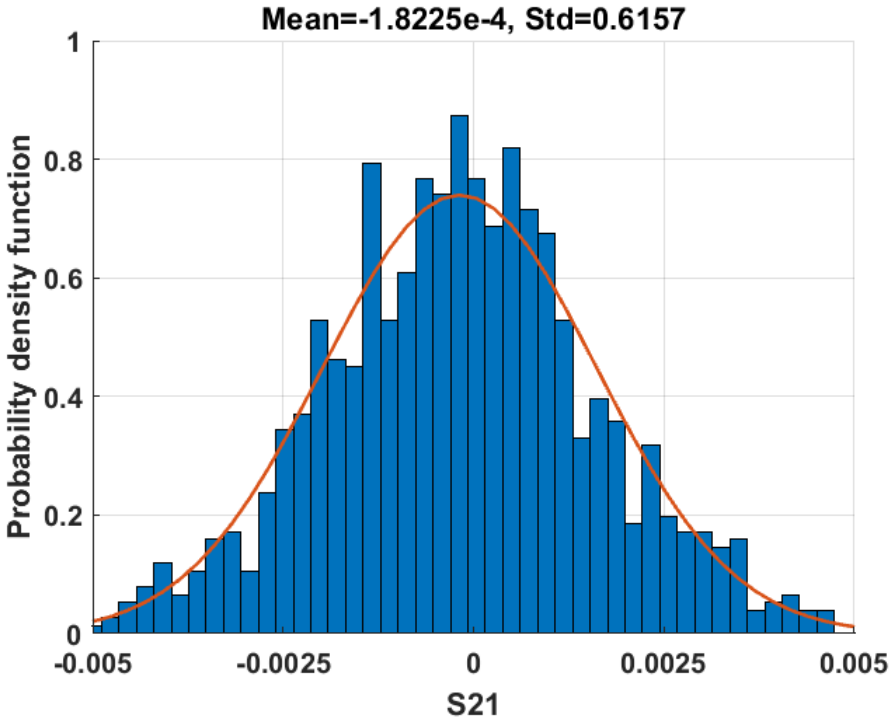

Figure 5. 60. Probability density function of the real part of S_{21} at 2GHz at point 2 in the enclosure with the 90mm×90mm×90mm cube and *r*=6mm circular aperture.

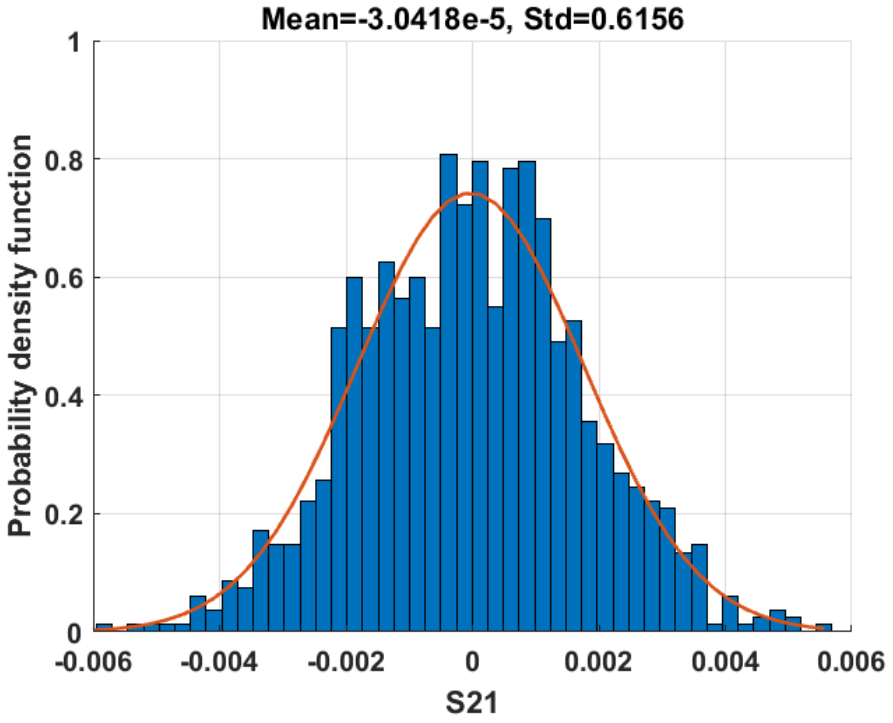

Figure 5. 61. Probability density function of the imaginary part of S_{21} at 2GHz at point 2 in the enclosure with the 90mm×90mm×90mm cube and *r*=6mm circular aperture.

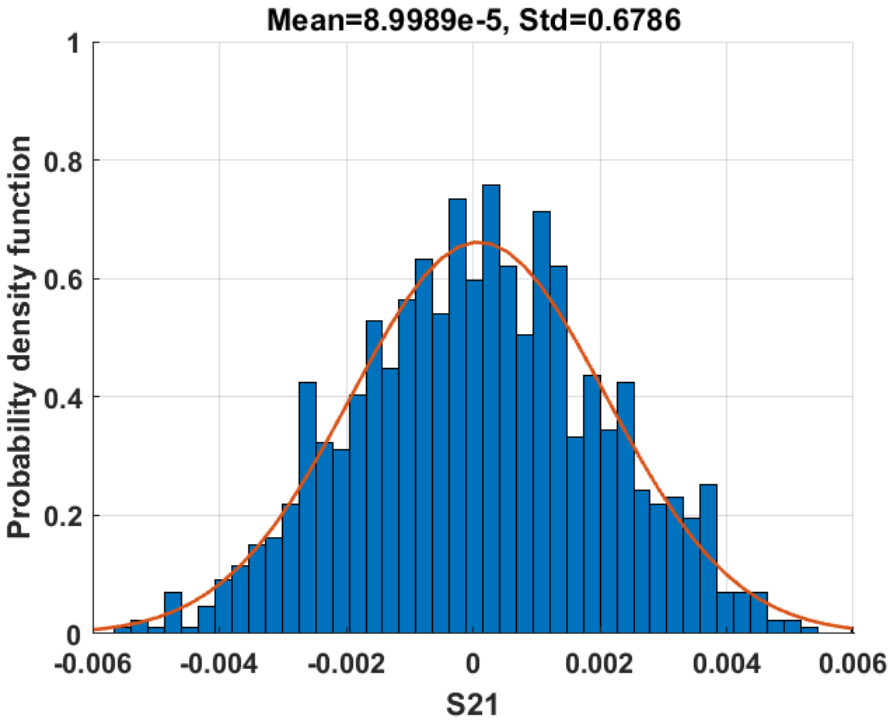

Figure 5. 62. Probability density function of the real part of S_{21} at 3GHz at point 2 in the enclosure with the 90mm×90mm×90mm cube and *r*=6mm circular aperture.

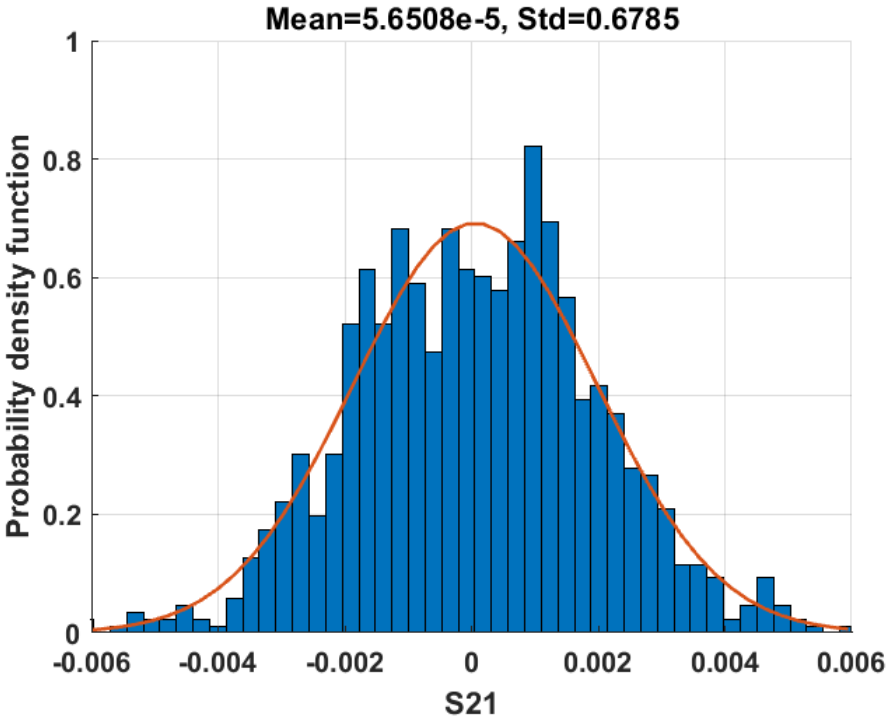

Figure 5. 63. Probability density function of the imaginary part of S_{21} at 3GHz at point 2 in the enclosure with the 90mm×90mm×90mm cube and *r*=6mm circular aperture.

5.9. Summary

In this chapter, we present a new method to predict electromagnetic field in populated enclosures, the diffusion model. The diffusion model has been used in acoustics for many years. In this thesis, for the first time, we applied the method to shielding problems.

The shielding effectiveness of an enclosure is defined as the ratio of field without and with the enclosure. In order to accurately predict the shielding effectiveness, it is necessary to obtain the precise internal field. The widely used power balance method calculates shielding effectiveness by using the absorption cross section of contents and transmission cross section of apertures. The basic assumption of the method is that the field in the enclosure is uniform in the steady state and it only holds when the loss in the enclosure is low. For moderate or high loss cases, the internal field in no longer uniform and the power balance method cannot describe this uniformity.

The diffusion model overcomes this limitation and it can be considered as a generalization of the power balance method. It compares the transmission of electromagnetic waves to radiative transport of particles in an enclosure and it is able to predict the variation of electromagnetic field in a cavity due to the presence of high losses. A 2D diffusion model has been tested previously, obtaining promising results. Here we demonstrated the usefulness of 3D diffusion model by using it to predict the power density of a populated enclosure and compare the results with full wave simulation and physical measurements. The comparisons indicated that with the presence of high loss, the energy in the enclosure is not uniform and the 3D diffusion model is able to show this change. For the enclosure with a 75mm×75mm square aperture, the predictions of the diffusion model are in agreement with those of full wave simulation and measurements, proving its availability. For the enclosure with an r=6mm circular aperture, the measurement is not in agreement with the diffusion model and full wave simulation at low frequencies. We have ruled out the influence of seam leakage and measurement noise floor. Currently we are still uncertain about the reason.

Chapter 6

Conclusions and future work

This work presented in this thesis centres on the prediction of shielding effectiveness. The shielding effectiveness of an enclosure quantifies its ability to protect its contents from electromagnetic interference. It is defined as the ratio of field/power density without and with the enclosure. In real applications, an enclosure is always populated and it has been proven that the contents have an effect on shielding effectiveness. Therefore, we need to consider contents when analysing shielding problems.

The first contribution of this thesis is that we demonstrated the absorption cross section of electronic components is hardly affected by their power states. The power balance method is widely used in the analysis of shielding problems of loaded enclosure. It treats shielding problems from an average energy point of view, assuming that in the steady state, the energy in the enclosure is uniform. By using the power balance method, the contents and the aperture are characterised by their absorption cross sections and transmission cross sections respectively. In this way, the shielding effectiveness is calculated from the absorption cross sections and transmission cross sections. The transmission cross section of an aperture is calculated from its polarizability tensors and the absorption cross section of content is obtained by physical measurements.

To the best of our knowledge, we have not found any reference that focus on the influence of power state on the absorption cross section. If the content contains active components, then behaviour of these components varies with power states and we assume that this change might affect its absorption cross section. In order to verify this assumption, we measured the absorption cross section of some computer components when they were both power on and powered off. A stress test software was used to make sure that all components (CPU, hard drive etc.) were in operation when powered on. The measurements were performed in a reverberation chamber and both frequency and time domain methods were used to obtain the absorption cross section. The results suggest that the power states have little influence on the absorption cross section within 1% measurement uncertainty. Since the

reverberation chamber we used is not perfect, we measured the absorption cross section of the powered on/off computer components at different locations in the chamber and did not observe obvious change in the results. Hence, we conclude that power state has little effect on the absorption cross section. When performing similar measurements in the future, there will be no need to consider power state, which brings convenience to the measurements.

The second contribution of this thesis is that we proved the usefulness of 3D diffusion model. A fundamental limitation of the power balance method is that it assumes in the steady state, the energy is uniform in the enclosure, which is only true when the loss in the enclosure is low. The diffusion equation based model stems from acoustics community and it is able account for the variation of electromagnetic energy in an enclosure due to the presence of moderate or high losses. Previously 2D diffusion model has tested, obtaining promising results. However, the 2D model can be only applied to symmetrical structures and thus has limited applicability.

In this thesis, we developed a 3D diffusion model. The 3D model enables more complex applications to be investigated. For instance, it is able to predict the non-uniform field in a populated equipment enclosure, informing the optimal positioning of sensitive components to reduce the influence of electromagnetic interference on them. In order to verify it, we used it to predict the power density in an enclosure and compared the results to those obtained by full wave simulation and measurement. The enclosure has a removable front face to allow different apertures to be installed. Therefore, we made two test scenarios, one with a 75mm×75mm square aperture and the other one with a r=6mm circular aperture. For each scenario, in order to introduce high loss, we put an absorbing cube in the enclosure.

The use of the 3D diffusion model requires the presence of a diffuse field. In the full wave simulation, this requirement is achieved by using a number of plane waves to illuminate the enclosure from different positions. As for the physical measurements, we preformed them in a reverberation chamber and used a mechanical stirrer to create a diffuse field.

Comparison between the diffusion model and the power balance method suggests that when the loss in the enclosure is low, the energy in the enclosure varies little with positions and the two methods leads to almost identical results. As the loss in the enclosure increases, the energy in the enclosure is not uniform and the power balance method cannot describe this

change. Comparisons between the diffusion model, full wave simulation and measurements indicate that for the enclosure with 75mm×75mm aperture, the predictions of the diffusion model is in agreement with those of the full wave simulation and measurements, with less than 3dB difference. For the r=6mm circular aperture, the predictions of the diffusion model agrees well the that of full wave simulation. The measurements, however, is not in agreement with them at low frequencies. We have ruled out the effects of seam leakage and insufficient diffuse field. Currently the reason for the discrepancy is still to be investigated.

Although we have shown the usefulness of the diffusion model, it requires further development. An extension of this work is to apply the diffusion model to enclosures with large dimensional ratios (one side is much longer than the other two). Diffusivity is a key parameter in the 3D diffusion model. In this thesis, we assume that for this application (the 300mm×300mm×120mm enclosure), the diffusivity is a constant. It has been pointed out the in an enclosure with a large dimensional ratio, the diffusivity along the long side is no longer a constant [82]. Although some empirical solutions have been proposed, more research is required to verify them. Solving this problem would allow the diffusion model to be applied to more complex problems.

List of Symbols

f	Frequency
E_0	Electric field with enclosure
E_i	Electric field without enclosure
k	Positive integer; wave number
m	Positive integer
n	Positive integer
l	Length
w	Width
h	Height
Q	Quality factor
c	Light speed
V	Volume
e	Natural logarithm; elliptical eccentricity
$N_{ms;ind}$	Number of independent samples of mechanical stirring
$N_{ms;tot}$	Number of total samples of mechanical stirring
$N_{ms;cor}$	Number of correlated samples of mechanical stirring
$N_{fs;ind}$	Number of independent samples of frequency stirring
$N_{fs;tot}$	Number of total samples of frequency stirring
$N_{fs;cor}$	Number of correlated samples of frequency stirring
N_{ind}	Number of independent samples
ω	Angular frequency
U_s	Steady state energy
W	Energy density

P_d	Dissipated power
E_{tot}	Total (rms) electric field
ε	Permittivity
λ	Wavelength
K	Rician K-factor
Q_u	Quality factor of an enclosure with aperture uncovered
Q_c	Quality factor of an enclosure with aperture covered
τ	Time constant
τ_u	Time constant of an enclosure with aperture uncovered
τ_c	Time constant of an enclosure with aperture covered
μ	Permeability
δ	Skin depth
A	Surface area
σ	Conductivity
A_e	Effective area of antenna
σ_a	Absorption cross section
σ_t	Transmission cross section
ϑ	Polar angle
φ	Azimuth angle
C_0	constant
$\sigma_{t//}^{x}$	Parallel polarisation in *x* axis
$\sigma_{t//}^{y}$	Parallel polarisation in *y* axis
σ_{t+}^{x}	Perpendicular polarisation in *x* axis
σ_{t+}^{y}	Perpendicular polarisation in *y* axis
α_e	Electric polarizability tensor
α_{mx}	Magnetic polarizability tensors in *x* axis
α_{my}	Magnetic polarizability tensors in *y* axis

r	Radius
f_c	Cut-off frequency of aperture
G	Net transfer function
α_u	Uncertainty
η_t	Efficiency of transmitting antenna
η_r	Efficiency of reviving antenna
τ_{wo}	Reverberation chamber time constant with dissipative object
τ_{no}	Reverberation chamber time constant without dissipative object
β	Ray magnitude
T	Propagation delay
V_r	Received signal voltage
$N_i(t)$ i=1, 2	Standard complex Gaussian random process
V_n	Background noise level
R	Resistance
C	Capacitance
R_p	Parallel resistor
R_s	Series resistor
L	Inductance
$\bar{a}$	Complex conjugate of a
$w(\mathbf{r})$	Energy density at position **r**
$S(\mathbf{r})$	Power density at position **r**
D	Diffusion coefficient
Λ	volumetric loss rate due to content absorption
P	Total radiated power
δ	Dirac function
l_{MFP}	Overall mean free path
$l_{\mathrm{MFP;wall}}$	Contribution to mean free path

	by walls
$l_{MFP;con}$	Contribution to mean free path by contents
α_{con}	Absorption efficiency of contents
$\hat{\mathbf{n}}$	Outward unit normal vector
α_{wall}	Absorption efficiency of walls
$\sum_{\alpha}(\mathbf{r})$	Absorption factor of walls
$\Gamma_{TE}(\vartheta)$	Fresnel reflection coefficient for the reflection of TE plane wave
$\Gamma_{TM}(\vartheta)$	Fresnel reflection coefficient for the reflection of TM plane wave
p	Volume power density
$w_r(\mathbf{r})$	Reverberant energy density at position **r**
V_s	Volume of volume source
$G(\cdot)$	Green's function
$J(\mathbf{r})$	Energy density flux at position **r**
$h_{ij}(\mathbf{r})$ i,j=1,2	Energy exchange coefficient
U	Total energy in the space
α_{con}	Absorption factor of contents
A_{wall}	Surface area of enclosure walls
A_{con}	Surface area of enclosure contents
$\sigma_{a;wall}$	Absorption cross section of walls
$\sigma_{a;con}$	Absorption cross section of contents
$u(\mathbf{r})$, $\mathbf{F}(\mathbf{r})$, $\mathbf{G}(\mathbf{r})$, $\varphi(\mathbf{r})$, $\gamma(\mathbf{r})$, $\psi(\mathbf{r})$	Test functions used in FEM
T_k	Discrete elements in FEM
V_k	Finite element space on T_k
X	Type of finite elements in FEM
M	Dimension of finite element space V_k
$\mathbf{F}(\Omega)$	Angular spectrum

Ω	Solid angle
$\hat{\boldsymbol{\theta}}$, $\hat{\boldsymbol{\varphi}}$	Mutually orthogonal unit vectors
$F_\vartheta(\Omega)$, $F_\varphi(\Omega)$	Complex field amplitudes
$F_{\vartheta r}(\Omega)$, $F_{\vartheta i}(\Omega)$	Real and imaginary parts of $F_\vartheta(\Omega)$
$F_{\varphi r}(\Omega)$, $F_{\varphi i}(\Omega)$	Real and imaginary parts of $F_\varphi(\Omega)$
$P_n(x)$	Lengendre polynomial of order n
w_I	Gauss-Legendre quadrature weighting factor
N (mean, standard deviation)	Normal distribution
$D_{\max}$	Maximum dimension of the object under test
$O(\mathbf{r})$	Linear operator
L_{GL}	Order of Legendre polynomial
η_0	Free space impedance
ψ	Polarization angle in CST
IG	Mismatch corrected insertion gain
S_{ch}	Power density in reverberation chamber
S_{en}	Power density in enclosure
E_r	Randomized electric field
ϑ_r	Random angle between 0 and 2π

List of Abbreviations

ACF	Autocorrelation Function
ACS	Absorption Cross Section
CIR	Channel Impulse Response
CPU	Central Processing Unit
EEBC	Energy Exchange Boundary Condition
EMC	Electromagnetic Compatibility
EMI	Electromagnetic Interference
FDTD	Finite-Difference Time-Domain
FEM	Finite Element Method
GPU	Graphics Processing Unit
IFFT	Inverse Fast Fourier Transform
ILCM	Intermediate Level Circuit Model
LUF	Lowest Useable Frequency
OATS	Open Area Test Site
PCB	Printed Circuit Board
PDF	Probability Density Function
PDP	Power Delay Profile
PWB	Power Balance Method
RAM	Radio Absorbing Material
RF	Radio Frequency
RMS	Root Mean Square
SE	Shielding Effectiveness
TCS	Transmission Cross Section
TE	Transverse Electric
TM	Transverse Magnetic

References

[1] B. Keiser, *Principles of electromagnetic compatibility, 3rd edition*. Norwood, Artech House, Inc., 1987.

[2] A. C. Marvin, J. F. Dawson, S. Ward, L. Dawson, J. Clegg and A. Weissenfeld, " A proposed new definition and measurement of the shielding effect of equipment enclosures," *IEEE Transections on Electromagnetic Compatibility*, vol. 46, no. 3, pp. 459-468, August 2004.

[3] D. A. Hill, J. W. Adams, M. T. Ma, A. R. Ondrejka, B. F. Riddle, M. L. Crawford and R. T. Johnk, "Aperture excitation of electrically large, lossy cavities," Electronic and Electrical Engineering Laboratory, National Institutes of Standards and Technology, Boulder, USA, Technical Note 1361, September 1993.

[4] I. D. Flintoft, S. L. Parker, S. J. Bale, A. C. Marvin, J. F. Dawson and M. P. Robinson, "Measured absorption cross section of printed circuit boards from 2to 20GHz," *IEEE Transections on Electromagnetic Compatibility*, vol. 58, no. 2, pp. 553-560, April 2016.

[5] I. D. Flintoft, A. C. Marvin, F. I. Funn, L. Dawson, X. Zhang, M. P. Robinson and J. F. Dawson, " Evaluation of the diffusion equation for modelling reverberant electromagnetic fields," *IEEE Transactions on Electromagnetic Compatibility*, vol. 59, no. 3, pp. 760-769, June 2017.

[6] C. R. Paul, *Introduction to electromagnetic compatibility*. New Jersey: John Wiley & Sons, Inc., 1992.

[7] S. A. Schelkunoff, *Electromagnetic waves*. New York: David Van Nostrand, Inc., 1948.

[8] H. Kaden, *Wirbelströme und schirmung in der nachrichtentechnik*. Berlin: Springer, 1959.

[9] M. P. Robinson, T. M. Benson, C. Christopoulos, J. F. Dawson, M. D. Ganley, A. C. Marvin, S. J. porter and D. W. P. Thomas, "Analytical Formulation for the shielding effectiveness of enclosures with apertures," *IEEE Transactions on Electromagnetic Compatibility*, vol. 40, no. 3, pp. 240-248, August 1998.

[10] T. Konefal, J. F. Dawson, A. C. Marvin, M. P. Robinson and S. J. Porter, "A fast multiple mode intermediate level circuit model for the prediction of shielding effectiveness of a rectangular box containing a rectangular aperture," *IEEE Transactions on Electromagnetic Compatibility*, vol. 47, no. 4, pp. 678-691, November 2005.

[11] P. Dehkhoda, A. Tavakoli and R. Moini, "An efficient and reliable shielding effectiveness evaluation of a rectangular enclosure with numerous apertures," *IEEE Transactions on Electromagnetic Compatibility*, vol. 50, no. 1, pp. 208-212, February 2008.

[12] C. Hao and D. Li, "Simplified model for shielding effectiveness of a cavity with apertures on different sides," *IEEE Transactions on Electromagnetic Compatibility*, vol. 56, no. 2, pp. 335-342, April 2014.

[13] I. Junqua, J. P. Paramantier and F. Issac, "A network formulation of the power balance method for the high-frequency coupling," *Electromagnetics*, vol. 25, nos. 7-8, pp. 603-622, February 2005.

[14] U. Carlberg, P. S. Kildal, A. Wolfgang, O. Sotoudeh and C. Orlenius, "Calculated and measured absorption cross sections of lossy objects in reverberation chamber," *IEEE Transections on Electromagnetic Compatibility*, vol. 46, no. 2, pp. 146-154, May 2004.

[15] Y. He, "Application of the reverberation chamber to the shielding effectiveness measurement of physical small enclsoures," Ph.D. dissertation, Department of Electronic Engineering, University of York, York, UK, 2009.

[16] *American national standard guide for construction test sites for performing radiated emission measurements*, ANSI C67.4-2015, 2015.
[17] H. A. Mendes, "A new approach to electromagnetic field-strength measurements in shielded enclosures," Wescon Technical papers, USA, August 1968.
[18] I. D. Flintoft, "Notes on average power absorbed by cavity walls in a diffuse field," unpublished, University of York, June 2016.
[19] T. A. Loughry, "Frequency stirring: an alternate approach to mechanical mode-stirring for the conduct of electromagnetic susceptibility testing," Phillips Laboratory, Kirtland Air Force Base, Albuquerque, USA, Technical Report 91-1036, 1991.
[20] A. C. Marvin and Y. He, "A study of enclosure shielding effectiveness measurement using frequency stirring in a mode-stirred chamber," *Proceedings of the 2008 IEEE International Symposium on Electromagnetic Compatibility*, Detroit, USA, pp. 1-6, August 2008.
[21] Y. Huang and D. J. Edwards, "A novel reverberating chamber: the source stirred chamber," *Proceedings of the 8th IET International Conference on Electromagnetic* Compatibility, Edinburgh, UK, pp. 120-124, September 1992.
[22] D. Zhang and E. Li, "Loading effect of EUT on maximal electric field level in a reverberation chamber for immunity test," *Proceedings of the 2002 IEEE International Symposium on Electromagnetic Compatibility*, Minneapolis, USA, vol. 2, pp. 972-975, August 2002.
[23] D. A. Weston, *Electromagnetic compatibility: principles and applications*. New York, Marcel Dekker, Inc., 1991.
[24] *Testing and measurement techniques: reverberation chamber test methods*, IEC 61000-4-21:2011, 2011.
[25] *Requirements for the control of electromagnetic interference characteristics of subsystems and equipment*, MIL-STD-461F, 2007.
[26] M. R. Schroeder, "The Schroeder frequency revisited," *The Journal of the Acoustical Society of America*, vol. 99, no. 5, pp. 3240-3241, May 1996.
[27] R. H. Price, H. T. Davis and E. P. Wenaas, "Determination of the statistical distribution of electromagnetic-field amplitudes in complex cavities," *Physical Review E*, vol. 48, no. 6, pp. 4716-4729, December 1993.
[28] S. J. Boyes and Y. Huang, *Reverberation chambers: Theory and applications to EMC and antenna measurements*. New Jersey: John Wiley & Sons, Inc., 2016.
[29] C. L. Holloway, D. A. Hill, J. M. Ladbury, P. F. Wilson, G. Koepke and J. Coder, "On the use of reverberation chambers to simulate a Rician radio environment for the testing of wireless devices," *IEEE Transactions on Antennas and Propagation*, vol. 54, no. 11, pp. 3167-3177, November 2006.
[30] Q. Xu, Y. Huang, X. Zhu, L. Xing, Z. Tian and C. Song, "Shielding effectiveness measurement of an electrically large enclosure using one antenna," *IEEE Transactions on Electromagnetic Compatibility*, vol. 57, no. 6, pp. 1466-1471, December 2015.
[31] *IEEE standard method for measuring the shielding effectiveness of enclosures and boxes having all dimensions between 0.1m and 2m*, IEEE Std. 299.1-2013, 2013.
[32] B. H. Bakker and H. F. Pues, "A novel technique for damping site attenuation resonances in shielded semi-anechoic rooms," *Proceedings of 7th International Conference on Electromagnetic Compatibility*, York, UK, pp. 119-124, August 1990.
[33] D. W. P. Thomas, A. Denton, T. Konefal, T. M. Benson, C. Christopoulos, J. F. Dawson, A. C. Marvin and S. J. Porter, "Characterisation of the shielding effectiveness of loaded enclosures," *Proceedings of the 1999 International Conference and Exhibition on Electromagnetic Compatibility*, York, UK, pp. 89-94, July 1999.

[34] W. Wallyn and D. De Zutter, " Modelling the shielding effectiveness and resonances of metallic shielding enclosures loaded with PCBs," *Proceedings of the 2001 IEEE International Symposium on Electromagnetic Compatibility*, Montreal, Canada, pp. 691-696, August 2001.
[35] A. C. Marvin, G. Esposito, J. F. Dawson, I. D. Flintoft, L. Dawson, J. A. K. Everard and G. C. R. Melia, "A wide-band hybrid antenna for use in reverberation chambers," *Proceedings of the 2013 IEEE International Symposium on Electromagnetic Compatibility*, Denver, USA, pp. 222-226, August 2013.
[36] J. R. Solin, "Formula for the field excited in a rectangular cavity with an aperture and lossy walls," *IEEE Transections on Electromagnetic Compatibility*, vol. 57, no. 2, pp. 203-209, April 2015.
[37] J. M. Dunn, "Local, high-frequency analysis of the fields in a mode-stirred chamber," *IEEE Transections on Electromagnetic Compatibility*, vol. 32, no. 1, pp. 53-58, February 1990.
[38] D. A. Hill and M. H. Francis, " Out-of-band response of antenna arrays," *IEEE Transections on Electromagnetic Compatibility*, vol. 29, no. 4, pp. 282-288, November 1987.
[39] C. M. Butler, Y. R. Samii and R. Mittra, "Electromagnetic penetration through apertures in conducting surfaces," *IEEE Transections on Electromagnetic Compatibility*, vol. 20, no. 1, pp. 82-93, February 1978.
[40] H. A. Bethe, "Theory of diffraction by small holes," *The physical review*, 2nd series, vol. 66, nos. 7 and 8, pp. 163-182, October 1944.
[41] I. Junqua, J. P. Paramantier and S. Bertuol, "Fundamentals on the PWB approach," Technical report WP3-TN14-PWB-ONERA, September 2010.
[42] H. A. Mendez, "Shielding theory of enclosures with apertures," *IEEE Transections on Electromagnetic Compatibility*, vol. 20, no. 2, pp. 296-305, May 1978.
[43] D. A. Hill, Electromagnetic field in cavities: deterministic and statistical theories. New Jersey: John Wiley & Sons, Inc., 2009.
[44] C. L. Holloway, H. A. Shah, R. J. Pirkl, W. F. Young, D. A. Hill and J. Ladbury, "Reverberation chamber techniques for determining the radiation and total efficiency of antennas," *IEEE Transactions on Electromagnetic Compatibility*, vol. 60, no. 4, pp. 1758-1770, April 2012.
[45] X. Zhang, M. P. Robinson, I. D. Flintoft and J. F. Dawson, "Inverse fourier transform technique of measuring averaged absorption cross section in the reverberation chamber and Monte Carlo study of its uncertainty," *Proceedings of the 2016 IEEE International Symposium on Electromagnetic Compatibility*, Wroclaw, Poland, pp. 263-267, September 2016.
[46] X. Zhang, M. P. Robinson, I. D. Flintoft and J. F. Dawson, "Efficient determination of reverberation chamber time constant," *IEEE Transactions on Electromagnetic Compatibility*, vol. 60, no. 5, pp. 1296-1303, October 2018.
[47] A. A. M. Saleh and R. A. Valenzuela, "A statistical model for indoor multipath propagation," *IEEE Journal on Selected Areas in Communications*, vol. 5, no.2, pp. 128-137, February 1987.
[48] *Uncertainty of measurement—Part 3: Guide to the expression of uncertainty in measurement*, ISO/IEC Guide 98-3:2008 (JCGM/WG1/100),2008.
[49] Matlab [Online]. Available: https://www.mathworks.com/products/matlab.html
[50] I. D. Flintoft, A. C. Marvin, M. P. Robinson, K. Fischer and A. J. Powell, "The re-emission spectrum of digital hardware subjected to EMI," *IEEE Transactions on Electromagnetic Compatibility*, vol. 45, no. 4, pp. 576-585, November 2003.
[51] HeavyLoad [Online]. Available: https://www.jam-software.com/heavyload.

[52] V. Rajamani, C. F. Bunting and J. C. West, “Sensitivity analysis of a reverberation chamber with respect to tuner speeds,” *Proceedings of the 2007 IEEE International Symposium on Electromagnetic Compatibility*, Honolulu, USA, pp. 1-6, July 2007.

[53] K. A. Remley, J. Dortmans, C. Weldon, R. D. Horansky, T. B. Meurs, C. M. Wang, D. F. Williams, C. L. Holloway and P. F. Wilson, “Configuring and verifying reverberation chambers for testing cellular wireless devices, “ *IEEE Transections on Electromagnetic Compatibility*, vol. 58, no. 3, pp. 661-672, June 2016.

[54] W. T. C. Burger, K. A. Remley, C. L. Holloway and J. M. Ladbury, “Proximity and antenna orientation effects for large-from-factor devices in a reverberation chamber,” *Proceedings of the 2014 IEEE International Symposium on Electromagnetic Compatibility*, Denver, USA, pp. 671-676, August 2013.

[55] C. Foy, J. Picaut and V. Valeau, “Including scattering within room acoustics diffusion model: an analytical approach,” *The Journal of the Acoustical Society of America*, vol. 140, no. 4, pp. 2659-2669, October 2016.

[56] C. Foy, V. Valeau, J. Picaut, N. Fortin, A. Sakout and C. Prax, “Modelling the inhomogeneous reverberant sound field within the acoustic diffusion model: a statistical approach,” *The Journal of the Acoustical Society of America*, vol. 141, no. 5, pp. 3931-3932, May 2017.

[57] J. M. Navarro, “Discrete time modelling of diffusion processes for acoustic simulation and analysis,” Ph.D. dissertation, Department of Communication, Polytechnic University of Valencia, Valencia , Spain, 2011.

[58] J. Picaut, L. Simon and J. D. Polack, “A mathematical model of diffuse sound field based on a diffuse equation,” *Acta Acustica United with Acustica*, vol. 83, no. 4, pp. 614-621, July 1997.

[59] C. Foy, V. Valeau, A. Billon, J. Picaut and A. Sakout, “An empirical diffusion model for acoustic prediction in rooms with mixed diffuse and specular reflections,” *Acta Acustica United with Acustica*, vol. 95, no. 1, pp. 97-105, January 2009.

[60] J. M. Navarro and J. Escolano, “Simulation of building indoor acoustics using an acoustic diffusion equation model,” *Journal of Building Performance Simulation*, vol. 8, no. 1, pp. 3-14, January 2015.

[61] V. Valeau, M. Hodgson and J. Picaut, “A diffusion based analogy for the prediction of sound fields in fitted rooms,” *Acta Acustica United with Acustica*, vol. 93, no. 1, pp. 94-105, January 2007.

[62] V. Valeau, J. Picaut and M. Hodgson, “On the use of a diffusion equation to for room acoustic perdiction,” *The Journal of the Acoustical Society of America*, vol. 119, no. 3, pp. 1504-1513, February 2006.

[63] C. Visentin, N. Prodi and V. Valeau, “A numerical investigation of the Fick’s law of duffusion in room acoustics,” *The Journal of the Acoustical Society of America*, vol. 132, no. 5, pp. 3180-3189, November 2012.

[64] W. C. Sabine, Collected papers on acoustics, Harvard University Press, Cambridge, USA, 1922.

[65] C. F. Eyring, “Reverberation time in dead rooms,” *The Journal of the Acoustical Society of America*, vol. 168, no. 1, pp. 217-241, 1930.

[66] Y. Jing and N. Xiang, “On boundary conditions for the diffusion equation in room-acoustic prediction: theory, simulations and expriments,” *The Journal of the Acoustical Society of America*, vol. 123, no. 1, pp. 145-153, January 2008.

[67] D. A. Hill, “A reflection coefficient derivation for the Q of a reverberation chamber,” *IEEE Transections on Electromagnetic Compatibility*, vol. 38, no. 4, pp. 591-592, November 1996.
[68] A. Billon, C. Foy, J. Picaut, and V. Valeau, “Modeling the sound transmission between rooms coupled through partition walls by using a diffusion model,” *Journal of the Acoustical Society of America*, vol. 123, no.6, pp. 4261-4271, June 2008.
[69] A. Billon, J. Picaut and A. Sakout, “Prediction of the reverberant time in high absorbent room using a modified diffusion model,” *Applied Acoustics*, vol. 69, no. 1, pp. 68-74, January 2008.
[70] F. Hecht, “New development in FreeFEM++,” *Journal of Numerical Mathematics*, vol. 20, nos. 3-4, pp. 251-266, March 2013.
[71] F. Hecht, S. Auliac, O. Pironneau, J. Morice, A. Le Hyaric, K. Ohtsuka and P. Jolivet, *Freefem++,* Third edition, Version 3.58-1. [Online]. Available: http://www3.freefem.org/ff++/ftp/freefem++doc.pdf. [Accessed: December 12, 2018].
[72] M. Discacciati, A. Quarteroni and A. Valli, “ Robin-Robin domain decomposition methods for the Stocks-Darcy coupling,” *SIAM Journal on Numerical Analysis*, vol. 45, no. 3, pp. 1246-1268, January 2007.
[73] H. Si, “TetGen, a Delaunay based quality tetrahedral mesh generator,” *ACM Transactions on Mathematical Software*, vol. 41, no.2, pp. 1-36, January 2015.
[74] Computer Simulation Technology (CST). [Online]. Available: http://www.cst.com. [Accessed: January 5th, 2019].
[75] I. D. Flintoft, S. J. Bale, A. C. Marvin, M. Ye, J. F. Dawson, C. Wan, M. Zhang, S. L. Parker and M. P. Robinson, “Representative contents design for shielding enclosure qualification from 2 to 20 GHz,” *IEEE Transactions on Electromagnetic Compatibility*, vol. 60, no. 1, pp. 173-181, February 2018.
[76] X. Zhang, “Accurate wideband measurement of human body absorption cross section in reverberation chamber: A morphological parameters study from 1GHz to 18GHz,” Ph.D. dissertation, Department of Electronic Engineering, University of York, York, UK, 2017.
[77] York Advanced Research Computing Cluster (YARCC). [Online]. Available: http://wiki.york.ac.uk/display/RHPC/YARCC+-+York+Advanced+Research+Computing+Cluster. [Accessed: January 7th, 2019].
[78] D. A. Hill, “Plane wave integral representation for fields in reverberation chambers,” *IEEE Transactions on Electromagnetic Compatibility*, vol. 40, no. 3, pp. 209-217, August 1998.
[79] J. C. West, C. F. Burning and V. Rajamani, “Accurate and efficient numerical simulation of the random environment within an ideal reverberation chamber,” ,” *IEEE Transactions on Electromagnetic Compatibility*, vol. 54, no. 1, pp. 167-173, February 2012.
[80] W. P. Johnson, “Review of Mathematics and Social Utopias in France: Olinde Rodrigues and His times by Simon Altmann and Eduardo L. Ortiz,” *The American Mathematical Monthly*, vol. 114, no. 8, pp. 752-758, October 2007.
[81] O. Bucci and G. Franceschetti, “On the spatial bandwidth of scattered fields,” *IEEE Transactions on Antennas and Propagation*, vol. 35, no. 12, pp. 1545-1555, December 1987.
[82] C. Visentin, N. Prodi, V. Valeau, and J. Picaut, “Experimental analysis of the relationship between reverberant acoustic intensity and energy density inside long rooms,” *Journal of the Acoustical Society of America*, vol. 138, no.1, pp. 181-192, July 2015.